Carbon Nanotube Thin Films for Active Noise Cancellation, Solar Energy Harvesting, and Energy Storage in Building Windows

A Dissertation
SUBMITTED TO THE FACULTY OF
UNIVERSITY OF MINNESOTA
BY

Shan Hu

IN PARTIAL FULFILLMENT OF THE REQUIREMENTS
FOR THE DEGREE OF
DOCTOR OF PHILOSOPHY

Adviser: Dr. Rajesh Rajamani

July 2014

Acknowledgements

This dissertation is impossible without the help, guidance, and support from a lot of people, to whom I would like to express my sincere thankfulness.

Firstly, I would like to thank my Ph.D. advisor Professor Rajesh Rajamani for guiding me into the exciting fields of nanotechnology and energy. His trust and support make it possible for me to explore a wide range of topics in this dissertation. From him I learned the qualities of a great researcher and educator.

Secondly, I want to thank my M.S. advisor Professor Xun Yu for continuing to provide help and guidance on my research and career development after I graduated from his group. His Ph.D. research lays a solid foundation for this dissertation.

Thirdly, I would like to thank my dissertation committee Professor Kim Stelson, Professor Rusen Yang, and Professor Gregory Cibuzar for reviewing my thesis and for raising excellent questions during the oral defense. Reversions based on their questions make this work more comprehensive.

Finally, I want to thank former and current members of the Laboratory for Innovations in Sensing, Estimation, and Control including Lee Alexander, Dr. Gridsada Phanomchoeng, Dr. Krishna Vijayaraghavan, Dr. Peng Peng, Dr. Kalpesh Singal, Dr. Saber Taghvaeeyan, Garrett Nelson, Mahdi Ahmadi, Ye Zhang, Song Zhang, Ryan Madson, Woongsun Jeon. Without them, the four-and-a-half years I spent at the University of Minnesota Twin Cities would have been less enjoyable.

Dedication

This dissertation is dedicated to my mom Peijuan Luo, my dad Xuewu Hu, and my husband Junyan Shen
for their unconditional love and support.

They are my ultimate driving force and forever source of inspiration.

Abstract

This research explores the application of carbon nanotube (CNT) films for active noise cancellation, solar energy harvesting and energy storage in building windows. The CNT-based components developed herein can be integrated into a solar-powered active noise control system for a building window.

First, the use of a transparent acoustic transducer as both an invisible speaker for auxiliary audio playback and for active noise cancellation is accomplished in this work. Several challenges related to active noise cancellation in the window are addressed. These include secondary path estimation and directional cancellation of noise so as to preserve auxiliary audio and internal sounds while preventing transmission of external noise into the building.

Solar energy can be harvested at a low rate of power over long durations while acoustic sound cancellation requires short durations of high power. A supercapacitor based energy storage system is therefore considered for the window. Using CNTs as electrode materials, two generations of flexible, thin, and fully solid-state supercapacitors are developed that can be integrated into the window frame. Both generations consist of carbon nanotube films coated on supporting substrates as electrodes and a solid-state polymer gel layer for the electrolyte. The first generation is a single-cell parallel-plate supercapacitor with a working voltage of 3 Volts. Its energy density is competitive with commercially available supercapacitors (which use liquid electrolyte). For many applications that will require higher working voltage, the second-generation multi-cell supercapacitor is developed. A six-cell device with a working voltage as high as 12 Volts

is demonstrated here. Unlike the first generation's 3D structure, the second generation has a novel planar (2D) architecture, which makes it easy to integrate multiple cells into a thin and flexible supercapacitor. The multi-cell planar supercapacitor has energy density exceeding that of other planar supercapacitors in literature by more than one order of magnitude. All-solution fabrication processes were developed for both generations to achieve economical and scalable production. In addition to carbon nanotubes, nickel/nickel oxide core-shell nanowires were also studied as electrode materials for supercapacitors, for which high specific capacitance but low working voltage were obtained.

Semi-transparent solar cells with carbon nanotube counter electrodes are developed to power the active noise cancellation system. They can be directly mounted on the glass panes and become part of the home window. The 2.67% efficiency achieved is higher than the 1.8% efficiency required for harvesting adequate energy to cancel noise of 70dB Day-Night-Level, which impacts on a north-facing window.

In summary, this project develops several fundamental technologies that together can contribute to a solar-powered active noise cancellation system for a building window. At the same time, since the component technologies being developed are fundamental, it is also likely that they will have wider applications in other domains beyond building windows.

Table of Contents

List of Tables

List of Figures

1 Introduction

1.1 Carbon Nanotubes and Carbon Nanotube Thin Films

Carbon nanotubes (CNTs) are one of the most studied nanomaterials so far. Their molecular structure can be visualized as graphene sheets being rolled up along certain directions (Figure 1-1). Rolling up a single layer of a graphene sheet gives single-wall carbon nanotubes (SWNTs), whereas rolling up multiple layers concentrically gives multi-wall carbon nanotubes (MWNTs). Depending on the directions of rolling, CNTs have different chirality, including armchair, zigzag, and chiral structures (Figure 1-2 (a) to (c) illustrate the schematics of their molecular structures).[1] Due to their unique structures, CNTs have exceptional electrical, mechanical, thermal and optical properties, which have attracted a lot of research attention. An individual CNT can be either semiconducting or metallic depending on its chirality and tube diameter.[2-3] Metallic CNTs have low resistivity and high current-carrying capacities (up to ~10^9 A cm^{-2}),[4] which make them excellent materials as conductors for advanced electrical interconnects. CNTs have super strong tensile strength; the density-normalized strength of SWNTs is ~50 times higher than that of steel.[5] Hence, CNTs are used as fillers in various composite materials for enhanced mechanical strength.[6] CNTs also have high thermal conductivities (up to 3500 Wm^{-1} K^{-1})[7], and researchers have used CNTs as thermal interface for rapid electronic cooling.[8-9] Its mesoporous structure with pore size between 2 and 50 nm results in specific surface area in the order of 1000 m^2/g.[10] CNT thin films with thickness ranging from several nanometers to several microns represent the most promising form of CNT for practical applications. They have properties that can approach the exceptional

characteristics of individual CNTs, but they are far more suitable for practical applications because they can be easily integrated into devices. Hence, preparation of CNT thin films on desired substrates is the starting point of many CNT-based devices. Methods to deposit CNT thin films include Chemical Vapor Deposition (CVD) growth[11-12] and solution-based deposition (such as spray coating,[13] ink-jet printing,[14] and vacuum filtration[15]). Compared with CVD growth, solution-based deposition is more attractive because it is cost-effective, readily scalable, and compatible with a wide variety of substrates. However, the challenges for solution-based deposition method are how to achieve uniform distribution of nanotubes on the substrate and how to obtain a moderate-to-high nanotube areal density (the number of nanotubes per unit area). The challenges are introduced by the strong intertube interactions and low solubility of CNTs. Because of intertube attractive forces (the van der Waals forces), individual CNTs form bundles of different diameters (Figure 1-2 (d)). With the variation of bundle diameters, it is difficult to achieve uniform CNT thin film thickness. Because of low solubility, only sparse CNTs are present in stable solution. To obtain moderate-to-high CNT surface coverage with such a low concentration solution is very time-consuming, because deposition needs to be repeated numerous times.

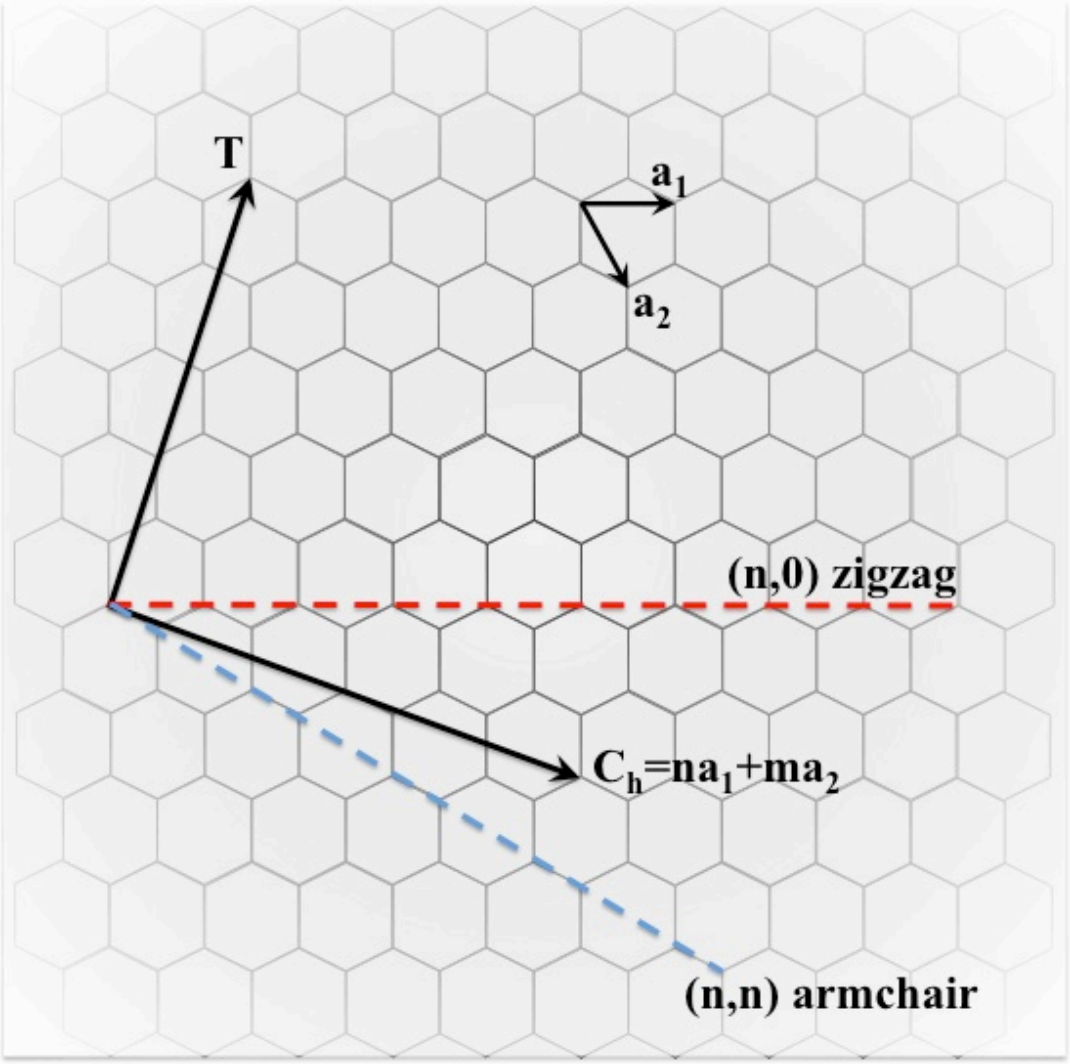

Figure 1-1 Schematic of a 2D graphene sheet being rolled up into a SWNT. a_1 and a_2 are lattice vectors. C_h is roll-up vector defined by a_1, a_2 and a pair of integers n, m. Chirality of CNT is determined by C_h with (n,0) being zigzag and (n,n) being armchair. T is the translation vector perpendicular to the roll-up vector and it is parallel to the tube axis.

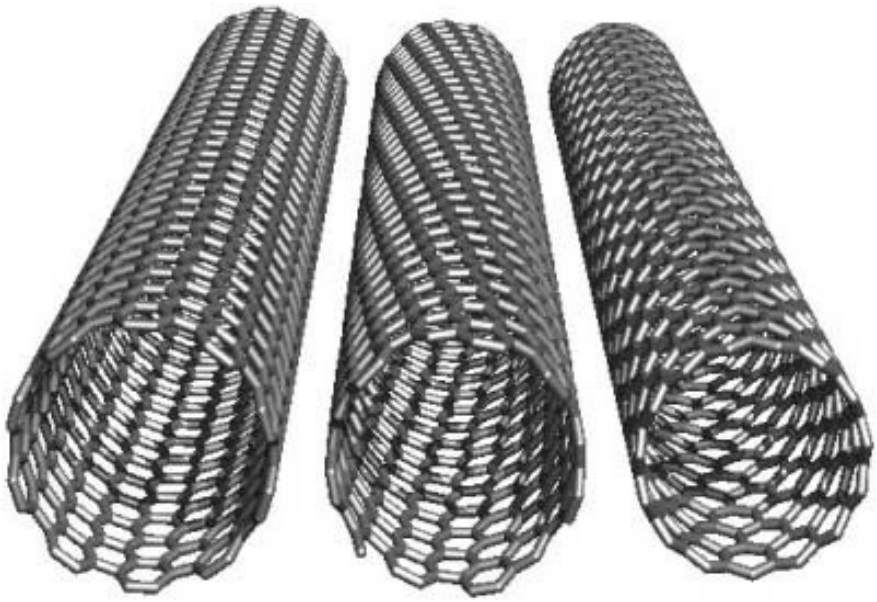

(a) (b) (c)

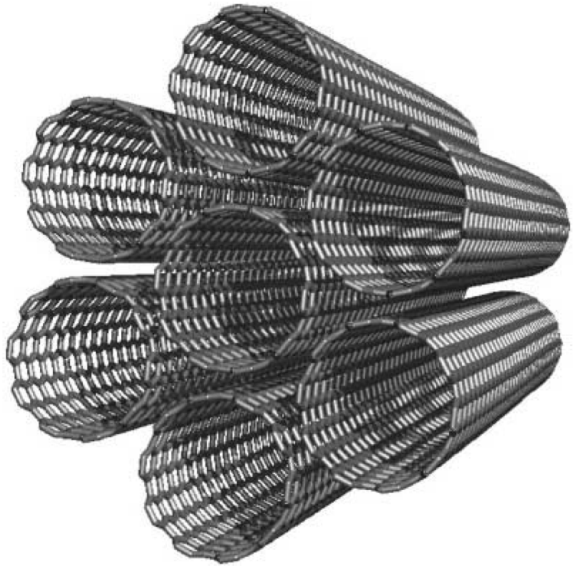

(d)

Figure 1-2 Schematics of defect-free and open-ended SWNTs of different chirality.[16] (a) A metallic armchair (10,10) SWNT; (b) a semiconducting chiral (12, 7) SWNT; (c) a metallic zigzag (15, 0) SWNT; (d) SWNT bundles consist of seven individual tubes held together by van der Waals forces (© 2002 WILEY-VCH Verlag GmbH, Weinheim, Fed. Rep. of Germany. Reuse with permission).

1.2 Functionalization of CNTs

Functionalization of CNTs, which attaches appropriate functional groups to the carbon scaffolds of CNT, is an effective solution to the above challenges. It is believed that functional groups can penetrate the CNT bundles and the result of the penetration is reduced intertube van der Waals forces, which facilitate the debundling of pristine CNTs. Furthermore, if the functional groups are polar (e.g. carboxyl groups -COOH) and the functionalized CNTs are dispersed into polar solvents (e.g. water) through ultrasonication, the weakened van der Waals forces can be completely overcome by the interaction between the polar solvent and functional groups, resulting in reduced bundle diameters (or completely de-bundling into individual nanotubes) and increased solubility of CNTs in solvent.

Methods to functionalize CNTs include covalent and noncovalent functionalization. In covalent functionalization, addition reaction happens in which the carbon-carbon double bonds in CNT are opened and functional groups are attached to one of the carbon atoms through covalent bonding. One of the most popular covalent functionalization techniques is "oxidative purification". As-synthesized CNTs by bulk production methods such as electric arc or HiPco process are unsupported and loose powders, called "soots" of CNT.[17-18] The soots have large bundles and considerable amount of impurities including amorphous carbon and catalyst metals (such as Fe and Co). During oxidative purification, CNT soots are treated in oxidizing acid (nitric acid,[19,20,21,22] mixture of sulfuric acid and hydrogen peroxide,[23] or the mixture of nitric acid and sulfuric acid[24]) at elevated temperature. The acid can purify the CNT soots by removing a significant

amount of amorphous carbon and metals. Meanwhile, it also introduces oxygen-bearing functional groups such as carboxylic groups to the end of the tubes and to the tube sidewalls' defect sites created by the oxidative conditions (Figure 1-3). The functional groups debundle CNTs and increase solubility of the acid-treated CNTs (a-CNTs). Longer acid treatment time at higher temperature can remove more impurities and decorate the nanotubes with larger amount of functional groups, thereby further debundling and dissolving the CNTs. However, it comes with a price. The acids can also cut the CNTs into shorter length, which reduces the electrical conductivity of the a-CNTs. It can also completely oxidize the tubes resulting in significant mass loss of CNT.

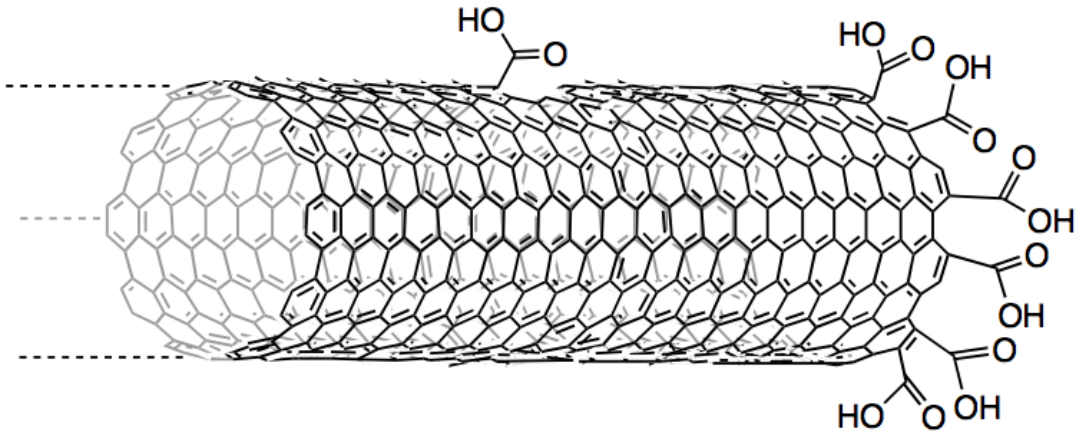

Figure 1-3 Schematic of a SWNT functionalized by carboxylic groups at its open end and sidewall.[16] ((© 2002 WILEY-VCH Verlag GmbH, Weinheim, Fed. Rep. of Germany, reuse with permission)

In noncovalent functionalization, appropriate surfactants are mixed with CNT and the mixture is subjected to ultrasonication. Surfactants are molecules with a hydrophilic part usually referred to as the polar head group and a hydrophobic region as tail. Commonly used surfactants for CNT dispersion include sodium dodecyl sulfate,[25]

sodium dodecylbenzyl sulfonate,[26] sodium dodecylsulfonate,[27] etc. The tails can form noncovalent bonding with the hydrophobic sidewalls of CNTs through pi-pi stacking (attractive interactions between organic molecules). The unzipping mechanism was proposed to explain the ultrasonication-assisted debundle and dissolve of CNT in surfactant-containing solvent (Figure 1-4).[28]

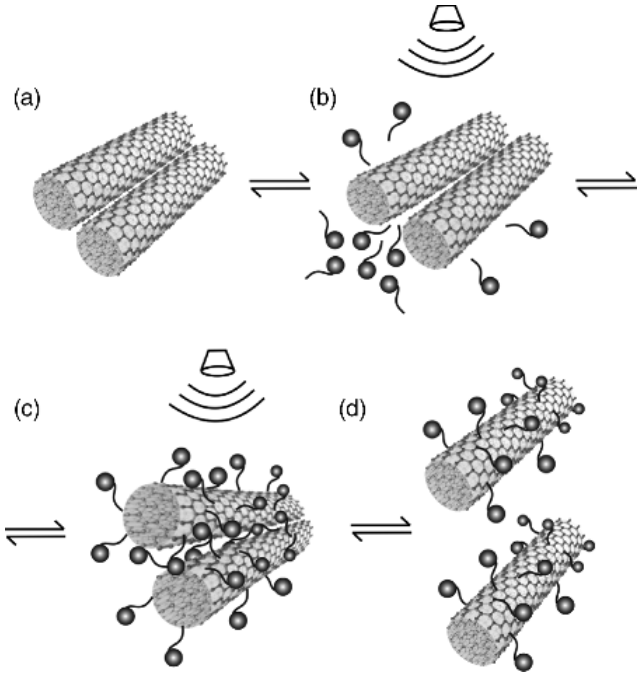

Figure 1-4 Unzipping mechanism for noncovalent functionalization of CNT by ultrasonication and surfactant.[29] (a) Pristine CNT bundles; (b) Surfactants' hydrophobic tails absorbed to dangling ends of individual tubes created by ultrasonication; (c) Surfactants progress through the length of tubes; (d) Individual tubes completely debundled and dispersed in solvents. (© 2010 John Wiley & Sons, Ltd. Reuse with permission)

During the first step of the proposed mechanism, sheer forces introduced by ultrasonication produce dangling ends in the CNT bundles, which become starting points of surfactant bonding. The surfactants prevent the dangling ends from re-aggregation. Due to continuous sheer force input and the relative movement of the dangling ends and the rest of the bundle, the surfactants progress through the nanotube length and eventually

completely debundle the tube. The hydrophilic heads of the surfactants then help dissolve the functionalized CNT into water. Unlike covalent functionalization, the noncovalent method is nondestructive. However, it introduces a lot of impurities (i.e. surfactants) into the CNT networks.

1.3 CNT-based Solar-powered Active Noise Control System

Functionalized CNTs become solution-processable. With CNT solutions, thin films of CNT can be fabricated onto various substrates in a more economical and scalable way. This research exploits the unique properties of functionalized CNT thin films to develop essential components for a solar-powered active noise control (ANC) system for a building window application. Figure 1-5 is the schematic of the proposed ANC system. It has an intelligent active noise controller, which can simultaneously perform ANC and auxiliary audio playback with a CNT-based transparent speaker mounted onto the interior side of the window. The second component is a semi-transparent solar cell that is also mounted onto the window (the exterior side) to generate enough energy to power the entire ANC system. The third component is a stack of thin, flexible, and solid-state CNT-based supercapacitors integrated with the window frame materials to provide necessary energy management for the proposed solar-powered system.

Such a solar-powered and self-efficient system is suitable for applications such as zero energy buildings, which are equipped with self-sufficient components and consume zero net energy year-round (energy used by the building equals renewable energy generated on site).

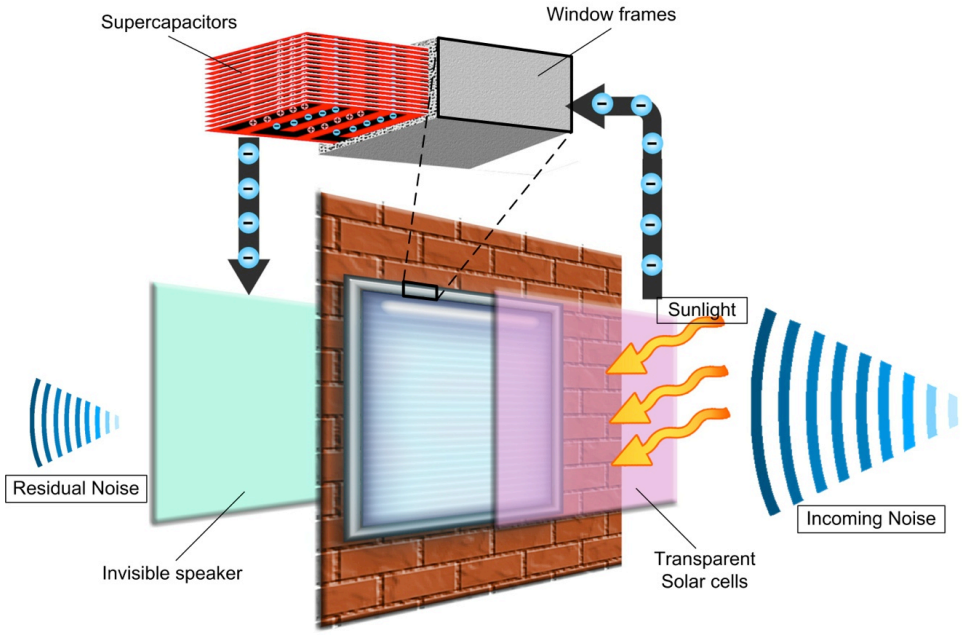

Figure 1-5 Schematic of a solar-powered ANC window with CNT-based components.

1.4 Thesis Contributions

This thesis proposes to develop the components for a solar-powered ANC system for building windows. Compared with the existing window ANC system, the solar-powered system will be more compact without requiring external power supply and more environmentally friendly. With an improved control algorithm, it also has the additional ability for simultaneous auxiliary audio playback and ANC. The major contributions of this thesis are:

1) **A novel control system**: The control system integrates a wave separation algorithm and a secondary path transfer function estimator with a standard feedforward adaptive noise controller. Such a control system allows the use of a CNT-based acoustic actuator for simultaneous ANC and auxiliary audio playback. The added algorithms and hardware can eliminate the interference between the

two functions, and also ensure that desirable internal sounds generated inside the buildings are not cancelled.

2) **Semi-transparent dye sensitized solar cells with CNT counter electrodes:** This research uses CNT thin films as counter electrodes to replace the more expensive and less stable platinum counter electrodes. The power conversion efficiency (PCE) of the developed solar cells is larger than the calculated required PCE to cancel a noise level of 70dB DNL. At the same time, the solar cells remain semi-transparent. This kind of solar cell has great potential to be integrated into building windows and car windows for solar energy harvesting.

3) **Thin, flexible, and solid-state supercapacitors:** Two generations of supercapacitors are developed using acid functionalized CNTs as electrode materials. Both generations are easy to be fabricated in large-scale on a variety of substrates, such as paper, polymer, etc. They are thin and flexible, thus can be mounted on almost any surfaces including those inaccessible to traditional bulky supercapacitors. They are solid-state without the electrolyte-leaking problem, thus handling is easy. The first generation is a single-cell system with specific capacitance and specific energy superior to commercial single-cell supercapacitors. The second generation is a multi-cell system with a novel 2D device architecture. The multi-cell system is very useful for systems requiring high working voltage and high energy density. In the solar-powered ANC system, the supercapacitors are used to rapidly provide electrical energy to power the real-time ANC system.

2 Intelligent Active Noise Control System for Home Windows

2.1 Active Noise Control for Home Windows

Homes close to airports and highways suffer from significant noise problems. Figure 2-1 shows the noise contour near the Minneapolis-St. Paul International Airport (MSP) area.[30] The unit DNL in Figure 2-1 stands for Day-Night Average Sound Level. It measures the average noise level over a 24-hour period. When calculating DNL, the noise between 10pm and 7am is artificially increased by 10 dB, whereas the noise levels at other times are the actual measured values. The 10 dB increase compensates for the decrease in community background noise during 10 pm and 7 am. Table 2-1 gives the number of residential homes included in the noise contour. More than 3000 homes are affected by noise more than 65 dB DNL. Every year, an average of more than $20 million was spent on the noise mitigation for homes and schools in the MSP area.

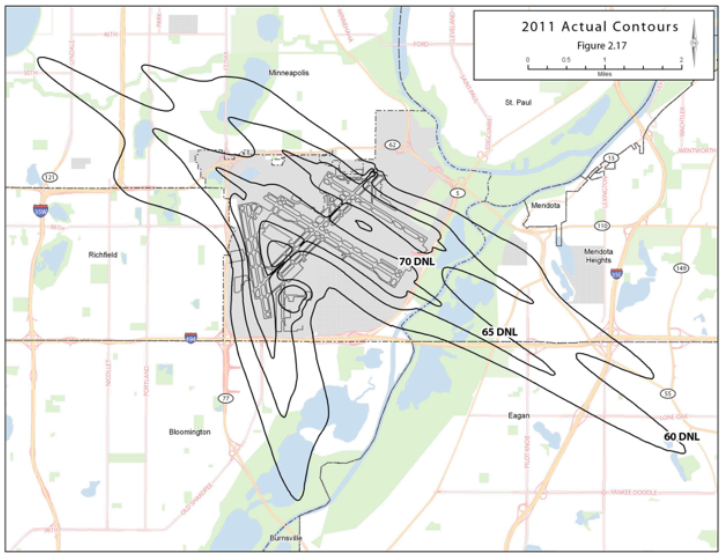

Figure 2-1 The noise contour in MSP area for the year 2011. [30]

Table 2-1 Minneapolis-St. Paul International Airport summary of 2011 actual DNL noise contour single family and multi-family unit counts (adapted from Figure 2-1)

	Dwelling Units Within DNL (dB) Interval							
	Single Family				Multi-Family			
	60-64	65-69	70-74	75+	60-64	65-69	70-74	75+
Minneapolis	5979	1525	-	-	509	474	-	-
Bloomington	79	2	-	-	447	618	-	-
Richfield	624	43	-	-	69	-	-	-
Eagan	148	1	-	-	-	-	-	-
Mendota Heights	54	1	-	-	-	-	-	-
Total	6884	1572	-	-	1025	1710	-	-

Windows constitute the primary path through which noise enters the home. For example, a typical frame wall may weigh 70 kg/m^2, while a typical single glazed window weighs about 7 kg/m^2. Consequently, the window can transmit roughly ten times as much sound energy as is transmitted through the same area of wall.[31] In studying the effectiveness of various measures in improving building insulation against traffic noise, Utley, *et al.* concluded that window improvements provide the most satisfaction to home dwellers.[32] The traditional passive method to reduce noise transmitted through windows is using sealed double-glazed windows in which two panes of glass are separated by a few millimeters of air cavity. The performance of double-glazed window is poor for low frequencies (<1 kHz), such as traffic noise. The sound transmission loss of a double-glazed window is greater than 40dB at 2 kHz but decreases to 20dB at 100Hz.[33] Active noise cancellation (ANC) is a better solution for reduction of low frequency noise.

Two main approaches of actively controlling sound transmission into a room have been proposed in literature. The first approach, loudspeaker-based active noise control,

uses loudspeakers as the secondary source. The loudspeakers are usually placed inside the room (room control).[34-35] The complex acoustical field in a room makes this approach difficult and less effective. The other approach is active structural acoustic control (ASAC). In this approach thin panels are placed in the sound transmission path. They are used as loudspeakers and their vibration is actively controlled by vibration inputs, yielding so-called "panel speakers".[36,37,38] In this way the transmission of noise is controlled before noise enters the acoustically complex room. As a result, the ASAC approach is used in this research.

2.2 ANC with a CNT-based Transparent Acoustic Actuator

Previous research on window ANC placed several voice coil actuators on glass to convert the glass panes of a window into speakers. The use of distributed voice coil on glass suffers from the disadvantage that the speed of bending waves in glass is too low to be useful for effective noise cancellation. While noise can be reduced at the location of the voice coil actuator, it is not reduced over the entire glass pane because when the "anti-noise" generated by the voice coil travels to the edge of the glass, it is not out of phase with the incoming noise anymore.[39] To address this shortcoming, researchers from our laboratory have previously developed a distributed transparent thin film acoustical actuator.[40] Figure 2-2 shows the developed transparent thin film actuator. Because of its high optical transmittance, the transparent film will not destroy the aesthetics and function of the window. The transparent actuator consists of a piezoelectric film with carbon nanotubes coated on both sides of the film as electrodes. It can be placed between the two panes of a double glazed window and serve as a distributed acoustic actuator. The

authors used a feedforward filtered-X least mean square (FXLMS) algorithm with this transparent thin film as the "panel speaker" to build a window ANC system.[39] Experimental results show that the ANC system can provide reduction in noise transmission through the window of 10-15 dB between 300 – 800 Hz. During characterization of the thin film actuator, it was noted that the actuator had good acoustic response as an audio loudspeaker. The actuator has a smooth response over a broadband range of frequencies. Considering the thin film actuator's effectiveness for the window ANC system and its promise as a general-use loudspeaker, there is good potential that this transparent thin film actuator when embedded into home windows can be used as an invisible speaker for simultaneous auxiliary audio playback (such as music) and window ANC. This research addresses the technical challenges associated with this application.

Figure 2-2 The transparent thin film speaker used in window active noise control system[39] (© 2007 IEEE. Reuse with permission)

2.3 Introduction to the Feedforward FXLMS Algorithm

To investigate the technical challenges of simultaneous audio playback and ANC, the working principle of a typical ANC algorithm (feedforward FXLMS) needs to be understood first. Figure 2-3 is a block diagram of the feedforward FXLMS control algorithm used for ANC system.[41-42] *x(n)* is the reference signal measured by an upstream reference microphone; *x'(n)* is the filtered version of *x(n)*; *e(n)* is the residual noise at downstream measured by an error microphone; *y(n)* is the control signal sent to actuator; *P(z)* is the unknown transfer function of sound transmission path from the error microphone to the reference microphone (i.e. primary path), *p(n)* is the impulse response of *P(z)*; *S(z)* is the dynamics from the secondary source to the error microphone (i.e. secondary path), *s(n)* is the impulse response of *S(z)*; $\hat{S}(z)$ is the estimation of this secondary path, $\hat{s}(n)$ is the impulse response of $\hat{S}(z)$; and *w(n)* is the adaptive digital filter that is used by the LMS algorithm to generate control signals *y(n)*. The FXLMS adaptation law for *w(n)* is given in Equation (2-1).

$$w(n+1) = w(n) + \mu \hat{x}(n) e(n) \tag{2-1}$$

where μ is the adaptation step size and $\hat{x}(n)$ is the convolution of $\hat{s}(n)$ and *x(n)*. Once the coefficients of *w(n)* have been updated using Equation (2-1), the active noise control signal *y(n)* will be produced as follows:

$$y(n) = w(n)x(n) = \sum_{l=0}^{L-1} w_l(n)x(n-l) \tag{2-2}$$

where *L* is the filter length. Then the control signals will be sent to the thin film speaker to generate anti-noise sound.

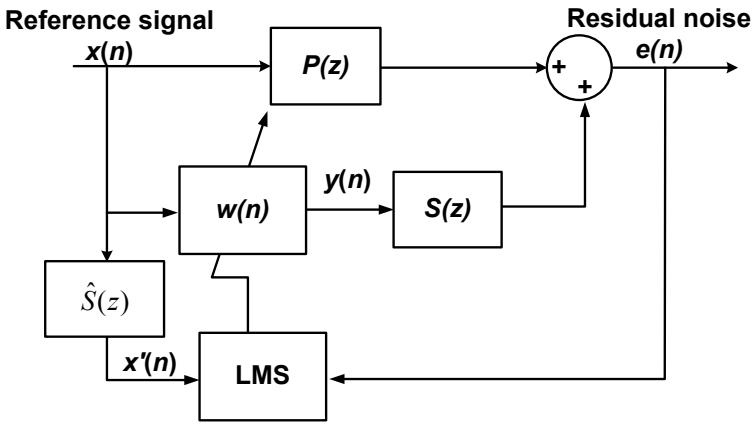

Figure 2-3 Flow chart of the feedforward FXLMS algorithm

2.4 Challenges in Simultaneous ANC and Audio Playback

When audio signals for playback are simultaneously created by the thin film speaker together with the anti-noise, they could be easily picked up by both the reference and the error microphones. The FXLMS control algorithm assumes that all sound picked up by the error microphone is undesired sound and should be cancelled. Using the traditional FXLMS algorithm for simultaneous ANC and audio playback could lead to a situation where the ANC system will act on the audio signals. Responding to the audio signals can cause two problems: (1) distortion of audio signals, and (2) decreased performance in cancellation of noise. When audio sound is picked up by the reference and the error microphones, $\hat{x}(n)$ and $e(n)$ in Equation (2-1) and the term $x(n)$ in Equation (2-2) will include an audio signal component in addition to that of the noise. Since the optimization goal of the LMS algorithm is to minimize the mean square of error signal $e(n)$, getting audio signals in the reference and the error signals will cause control signals to be generated to cancel the desired audio sound. In addition, with the presence of both

audio signals and noise in the control loop, the LMS algorithm is optimized towards the global minimization of audio signals and noise, which could weaken its control strength on the noise compared to the situation when it deals with the noise only.

To make simultaneous auxiliary audio playback and window active noise cancellation feasible, cancellation of audio sound by the ANC system should be prevented. Thus, the audio signals should be eliminated from the reference and the error signals. However, it is almost impossible to physically isolate the reference and the error microphones from the audio sound by physical barriers, especially in the case of the error microphones, which are located within the house. Given that audio signals and external noise are travelling from opposite directions with respect to the reference microphone, a wave separation algorithm can be used to separate audio signal and noise in the reference signal; whereas the same method cannot be applied to separate noise in the error signal, because noise and audio signals travel from the same direction with respect to the error microphone. However, if the audio signals picked up by the error microphone can be correctly estimated and subtracted from the error signals, the resultant error signals will be the residual of external noise after ANC only. Estimation of audio signals picked up by the error microphone can be achieved by estimating the dynamics from the thin film speaker to the error microphone, which is the secondary path transfer function *S(z)* in the feedforward FXLM algorithm shown in Figure 2-3. Since audio sound in the error signal can be computed as the response of *S(z)* to the source audio signals, with the source audio signals readily available, only the secondary path *S(z)* needs to be estimated. Thus, to develop simultaneous ANC and audio playback, this research needs to achieve two

objectives: (a) eliminating auxiliary audio signals from the reference signal; (b) eliminating auxiliary audio signals from the error signal.

2.5 Eliminating Audio Signals from the Reference Measurement by the Wave Separation Algorithm

2.5.1 Introduction to the Wave Separation Algorithm

A wave separation algorithm can separate the sound at any point into two components based on their direction of travel, i.e. the incident sound and the reflected sound. Since the external noise and audio signals are travelling in opposite directions with respect to the reference microphone, one of them can be treated as incident sound and the other as reflected sound. Hence, the wave separation algorithm can be used to separate external noise and audio signals picked up by the reference microphone.

Several wave separation algorithms have been proposed in literature. De Sanctis *et al.* placed two microphones in a duct for wave separation. They adaptively estimated the frequency domain transfer function between the two microphones using a third microphone. Then the forward and backward going sounds were estimated using the transfer function and inverse Fast Fourier Transform.[43] This frequency domain wave separation algorithm consumes a lot of computational power. Thus it is not suitable to be used with a real-time active noise control system. Time domain wave separation is a better option for real-time application. Kemp et al. placed M (M > 2) microphones in the acoustic field to estimate the inter-microphone time domain transfer functions for forward and backward direction. Then forward and backward going sound waves are

estimated by time domain convolution using the appropriate transfer functions.[44] Because of the significant delay introduced by multiple convolutions, it is possible that this method also will fail to keep up with the requirements for a real-time ANC. Thus a more time-efficient wave separation in time domain is needed for this research.

In this research, a time-domain wave separation algorithm based on the momentum equation and continuity equation was used.[45] The wave separation algorithm utilizes two microphones, which are a few inches apart. The pair of microphones is placed between the incident and the reflected sound source. In our case, the incident sound source is the noise source located outside of houses and the reflected sound source is the thin film speaker used to play audio signals. The set up of the wave separation system is shown in Figure 2-4. Here, $P_n(t)$ and $P_a(t)$ are noise and audio sound respectively; d is the distance between two microphones; and $P_1(t)$ and $P_2(t)$ are the acoustic pressure signals picked up by the two microphones. It is assumed that distance d is small compared to the wavelength of noise and audio sound. Let the acoustic pressure signals picked up by the two microphones be p_1 and p_2. If the distance d between the microphones is small relative to the smallest wavelength of the sound, the pressure at the midpoint is approximately:

$$p = \frac{p_1 + p_2}{2} \tag{2-3}$$

For a plane wave, the momentum equation yields

$$\rho \frac{\partial u}{\partial t} + \frac{\partial p}{\partial x} = 0 \tag{2-4}$$

Since the distance between the two microphones is small, the spatial derivative can be approximated by

$$\frac{\partial p}{\partial x} = \frac{p_2 - p_1}{d} \tag{2-5}$$

Substituting into Equation (2-4), the particle velocity is calculated as

$$u(t) = \frac{1}{\rho d}\int_0^t (p_1 - p_2)dx \tag{2-6}$$

The incident wave can be expressed as [24]

$$p_i = \sum_n A_n e^{j(w_n t - k_n x)} \tag{2-7}$$

where the wave number k_n is related to the frequency ω_n and the speed of sound c by the relation $k_n = \omega_n / c$. Substituting into the momentum Equation (2-4), the particle velocity corresponding to the incident and reflected wave are

$$u_i = \frac{1}{\rho_0 c} p_i \tag{2-8}$$

$$u_r = -\frac{1}{\rho_0 c} p_r \tag{2-9}$$

Thus the overall particle velocity at the midpoint of the two microphones can be expressed as

$$u = u_i + u_r = \frac{1}{\rho_0 c}(p_i - p_r) \tag{2-10}$$

The associated pressure at the midpoint is

$$p = p_i + p_r \tag{2-11}$$

Combining Equations (2-10) and (2-11), the incident wave and the reflected wave can be calculated by Equation (2-12) and (2-13):

$$p_i = \frac{1}{2}(p + \rho_o c u) \tag{2-12}$$

$$p_r = \frac{1}{2}(p - \rho_0 c u) \tag{2-13}$$

To calculate p_i and p_r, p_1 and p_2 are first measured by the two closely positioned microphones. p is calculated using Equation (2-3). Numerical integration is then used to

update the particle velocity u, as shown in Equation (2-6). Finally, Equations (2-12) and (2-13) are used to obtain p_i and p_r.

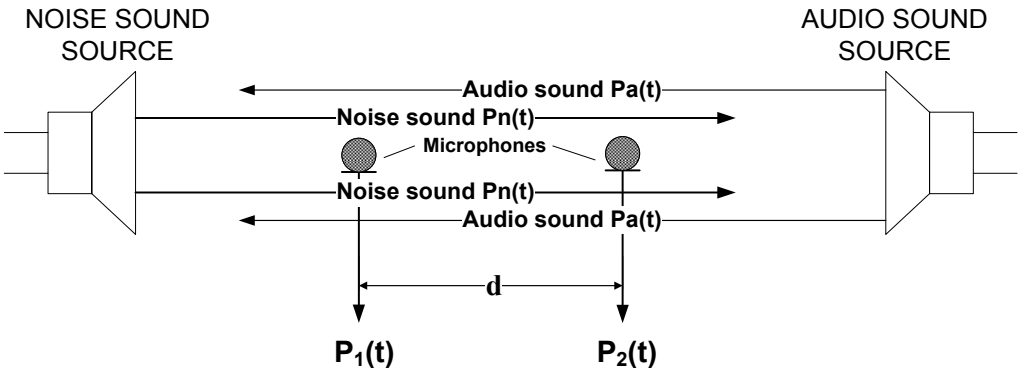

Figure 2-4 The integration method for wave separation

This time domain wave separation algorithm does not have time-consuming steps such as convolution and deconvolution. Hence, little time-delay will be introduced when it is used with the real-time active noise cancellation. The reason why sound wave travelling in opposite directions can be separated is that the wave separation algorithm introduces different transfer functions for different sound travel paths. The transfer functions from the external noise to the separated reference signals (called ‘‘forward path’’) and from the audio sound to the separated reference signals (called ‘‘backward path’’) can be derived and compared as follows. To derive the transfer function of the forward path, let the internal noise $P_i(t) = 0$ then $P_1(t) = P_e(t)$ and $P_2(t) = P_e(t\text{-}T)$, where T is the transmission delay from P_1 to P_2. T is determined by the speed of sound c and the distance d between the two microphones: $T = d/c$. Using Equation (2-6) and (2-12), we have the forward path transfer function to be

$$G_{forward}(s) = \frac{1+e^{-sT}}{4} + \frac{c}{2d}\frac{1-e^{-sT}}{s} \tag{2-14}$$

where s is the Laplace variable. Similarly, the backward path transfer function is

$$G_{backward}(s) = \frac{1+e^{-sT}}{4} + \frac{c}{2d}\frac{e^{-sT}-1}{s} \tag{2-15}$$

For d = 6.35 cm, as in the case of the reference microphone arrays used in this paper, the forward and backward paths' transfer functions in frequency domain are compared in Figure **2-5**. The forward path has a very flat frequency response at 0 dB magnitude and 0° phase, which means that the external noise will pass through the wave separation algorithm with little change in magnitude and no phase shift. The forward path acts like an all-pass filter for the external noise. However, the backward path has a large negative dB magnitude and non-zero phase shift, which means that the magnitude of the audio sound will be largely reduced after wave separation.

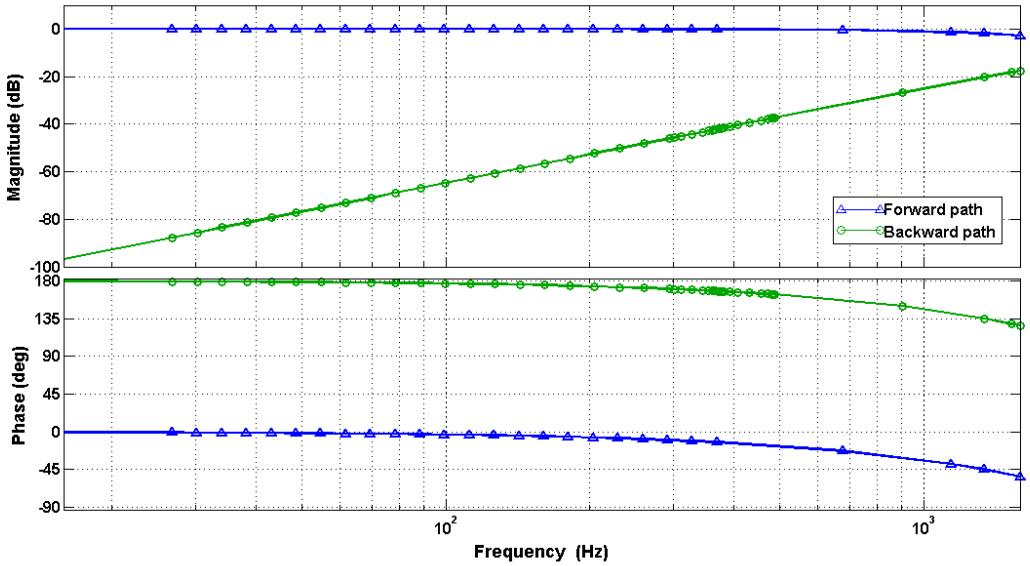

Figure 2-5 The forward path and backward path transfer functions' frequency responses

2.5.2 Error Analysis of the Wave Separation Algorithm

The error in the above wave separation algorithm mainly comes from approximating the spatial derivative of the sound pressure at the midpoint of the two microphones by a difference equation in Equation (2-5). The distance should be as small as possible so that the approximation in Equation (2-5) holds. However, in reality due to the limited resolution of the microphones, the spacing between the two microphones cannot be too small. Otherwise, the microphones will not be able to distinguish the pressure differences at the two microphone locations. The inter-microphone spacing of 6.35 cm used in this paper are smaller than the smallest wavelength of the sound in the experiments. At lower frequencies where the wavelengths are considerable larger than the microphone spacing, the approximation in Equation (2-5) is very close to the true value. On the other hands, at really high frequencies where the wavelengths are comparable to the microphone spacing, the approximation error becomes not negligible. This explains why the difference between the frequency response of the forward and that of the backward path becomes less at higher frequencies as shown in Figure 2-5. Thus, the wave separation is less effective at high frequencies than at low frequencies. Since the approximation error only has an effect on the particle velocity u in Equation (2-12) and (2-13) for calculating p_i and p_r, discussing the expected error of u as a function of frequency is equivalent to that of discussing the error in p_i and p_r.

To quantify the frequency dependence of the error introduced by the approximation in Equation (2-5) at the given microphone spacing used in our experiments, assume the sound pressure at position x and time t is given by

$$p = A\sin\left(\omega t - kx\right) \tag{2-16}$$

where A is the amplitude, ω is the angular frequency, k is the wave number and $k = \omega/c$ and c is the velocity of the sound. Then the spatial derivate of p at the midpoint of the two microphones ($x = d/2$) is given by

$$\left.\frac{dp}{dx}\right|_{x=\frac{d}{2}} = -Ak\cos\left(\omega t - \frac{kd}{2}\right) \tag{2-17}$$

Thus the particle velocity at $x=d/2$ is given by

$$u(t) = \frac{1}{\rho}\int_0^t \left.\frac{dp}{dx}\right|_{x=\frac{d}{2}} d\tau = \frac{-Ak}{\rho\omega}\left(\sin\left(\omega t - \frac{kd}{2}\right) + \sin\left(\frac{kd}{2}\right)\right) \tag{2-18}$$

The spatial derivative of p at $x = d/2$ can be approximated by

$$\frac{p_1 - p_2}{d} = \frac{A\sin\left(\omega t - kd\right) - A\sin\left(\omega t\right)}{d} \tag{2-19}$$

Hence the approximation particle velocity at $x=d/2$ is given by

$$\hat{u}(t) = \frac{1}{\rho}\int_0^t \frac{p_1 - p_2}{d} d\tau = \frac{-A}{\rho d\omega}\left(2\sin^2\left(\frac{\omega t}{2}\right) + \cos\left(\omega t - kd\right) - \cos\left(kd\right)\right) \tag{2-20}$$

For a discrete-time implementation, the relative approximation error is therefore given by

$$E\left(n\right) = \frac{u\left(n\Delta T\right) - \hat{u}\left(n\Delta T\right)}{u\left(n\Delta T\right)} \tag{2-21}$$

The root mean square (RMS) of the relative approximation error is given by

$$RMS = \sqrt{\frac{\sum_{n=0}^{N} E^2(n)}{N}} \tag{2-22}$$

The RMS error versus frequency is shown for d=6.35cm and 7.62cm in Figure 2-6. As discussed before, the expected error of approximation in Equation (2-5) increases with

frequency and inter-microphone distance. However, the relative errors are insignificant for both inter-microphone distances chosen for frequencies up to 1000 Hz.

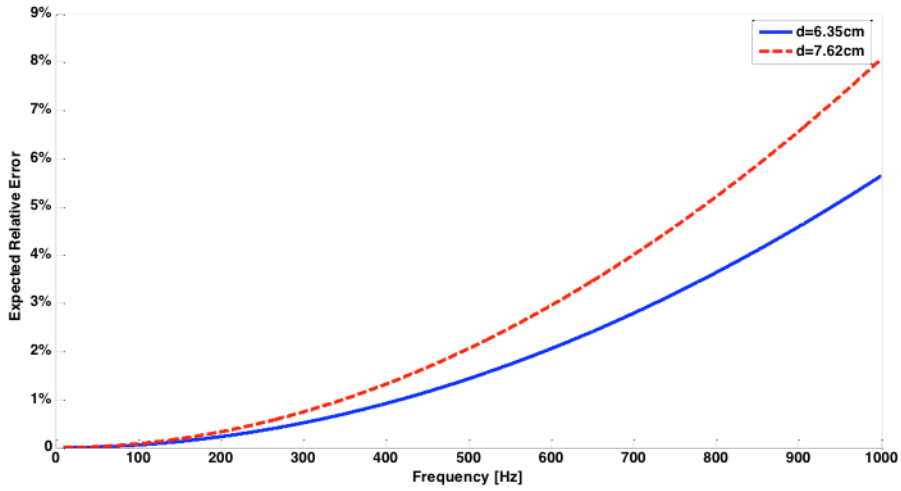

Figure 2-6 Relative errors in particle velocity u as a function of frequency at given inter-microphone distances d.

2.5.3 Effect of the Incident Angle on the Wave Separation Algorithm

The output of the new sensing system was experimentally measured at five different angles of 0°, 45°, 90°, 135°, and 180° respectively as shown in Figure 2-7. White noise was fed to the speaker and then the output from the sensing system integrated with wave separation algorithm was measured. After both the input and output signals at each angle were obtained, Fast Fourier Transform was used to compute the frequency response. The frequency responses of the sensing system integrated with wave separation at the five different angles are compared in Figure 2-8. The magnitude of the frequency response decreases in general as the angle increases from 0° to 180°. Overall, there is an obvious difference in magnitude for 0° < angle < 90° and 90° < angle < 180°. The magnitude at 180° is 10–15 dB smaller than that of 0°. The speaker being at angle 0° corresponds to the case that the external noise source is in line with the microphone pair.

In this case, the sensing system with wave separation allows the most amount of external sound to enter the separated reference signal. The speaker at angle 180° corresponds to the case that the internal noise source is in line with the microphone pair. In this case, the system prevents the most amount of internal sound from entering the separated reference signal. For an angle of 90°, the sound measured by both microphones are the same, thus the particle velocity *u* calculated from Equation (2-6) is zero. Hence, from Equation (2-12) and Equation (2-13), it can be seen that the separated sound is just half of the incident sound. The responses at angle 45° and 135° are in between. This is one more demonstration that the sensing system with the wave separation algorithm has the ability to selectively pick up sound coming from one side (0°<angle<90°) while suppressing the sound coming from the other side (90° < angle < 180°).

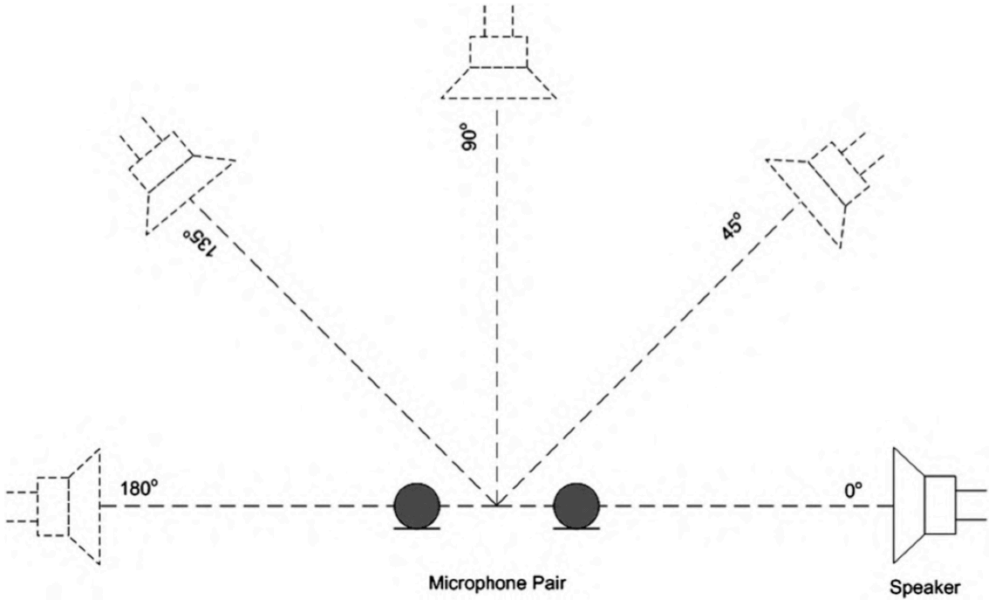

Figure 2-7 The speaker at five angles (0°, 45°, 90°, 135°, and 180°) with respect to the microphone pair.

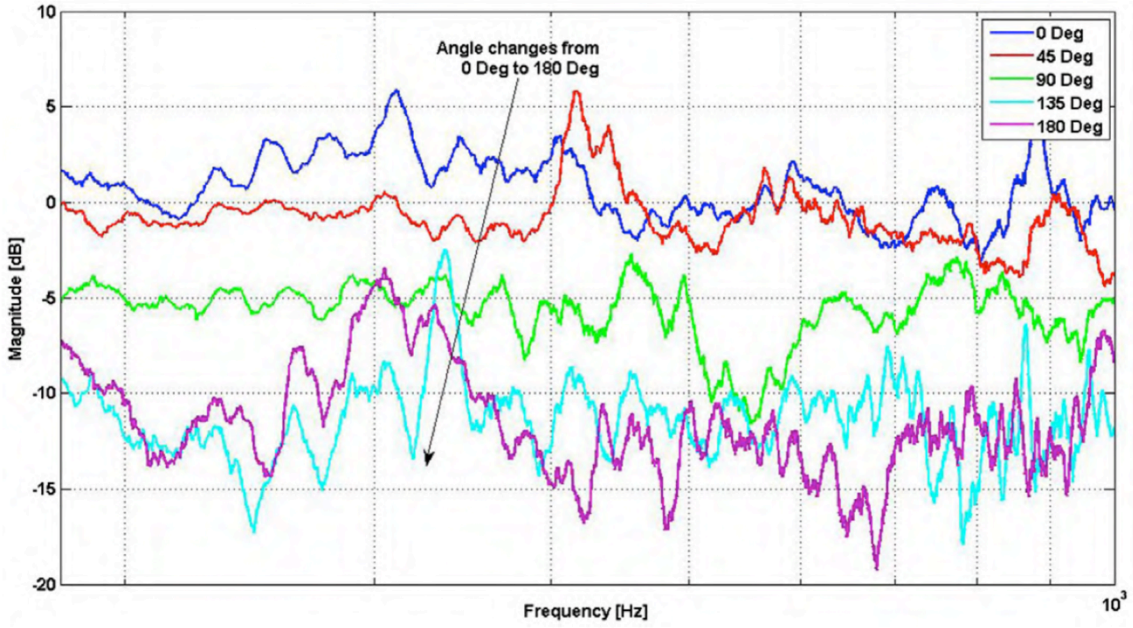

Figure 2-8 Comparison of the sensing system's frequency responses when the speaker's angle with respect to the microphone pair is at 0°, 45°, 90°, 135°, and 180° respectively.

2.6 Eliminating Audio Signals from the Error Measurement by Estimating the Secondary Path Transfer Function

Audio sound in the error signals should be eliminated to prevent the ANC system's response to audio signals. For that, audio signals picked up by the error microphone have to be estimated and subtracted from the error signals. The secondary path is the path by which audio signals travel from the speaker to the error microphone. Since the source audio signals are often readily available (from the CD player, for instance), if the dynamics of the secondary path is known, the audio signals picked up by the error microphone can be calculated as the response of the secondary path to the source audio signals. Unfortunately, the secondary path transfer function is usually unknown and time-variant, because it comprises components such as the thin film

speaker and the acoustic path from the speaker to the error microphone, whose dynamics could change with temperature and humidity. Hence, the key to reliably estimate audio signals is to estimate the time-variant secondary path transfer function in real time. Methods to estimate the secondary path transfer function using additive white noise are found in literature.[46-47] In addition, the secondary path transfer function can also be estimated using the auxiliary source audio signals.[48]

The schematic of the ANC system integrated with secondary-path estimation using the source audio signals is shown in Figure 2-9. Here $N(n)$ is the external noise separated from the reference signals by the wave separation algorithm. If the wave separation works perfectly, $N(n)$ will only contain the external noise but no audio signals. *e(n)* is the error signals measured by the error microphones. In the case of simultaneous ANC and audio playback, *e(n)* will be the mix of residual noise after ANC and audio signals. *e′(n)* is the estimated residual noise. Ideally *e′(n)* will only contain information of external noise. *A(n)* is the source audio signals sent to the actuator for audio playback. *A′(n)* is the estimated audio signals picked up by the error microphone. *p(n)* and *s(n)* are the impulse response of the primary path and the secondary path respectively. $\hat{s}(n)$ is the estimation of *s(n)*. *y(n)* is the ANC control signals. The LMS adaptation law for $\hat{s}(n)$ is as follows:

$$\hat{s}(n+1) = \hat{s}(n) + \mu_s A(n)e'(n) = \hat{s}(n) + \mu_{s_1} A(n)[A(n)s(n) - A(n)\hat{s}(n)] + \mu_{s_1} A(n)N_r(n) \quad (2\text{-}23)$$

where μ_{s_1} is the adaptation step size, and $N_r(n)$ is the residual noise after ANC given by

$$N_r(n) = N(n)p(n) - y(n)s(n) \quad (2\text{-}24)$$

The expected value of $\hat{s}(n)$ will converge to its optimal value *s(n)* if *A(n)* is uncorrelated with $N_r(n)$ and the expectation of residual external noise approaches to zero after ANC. However, the situation does exist when the audio signals are correlated with the residual noise, which could result in failure of correct secondary path identification.

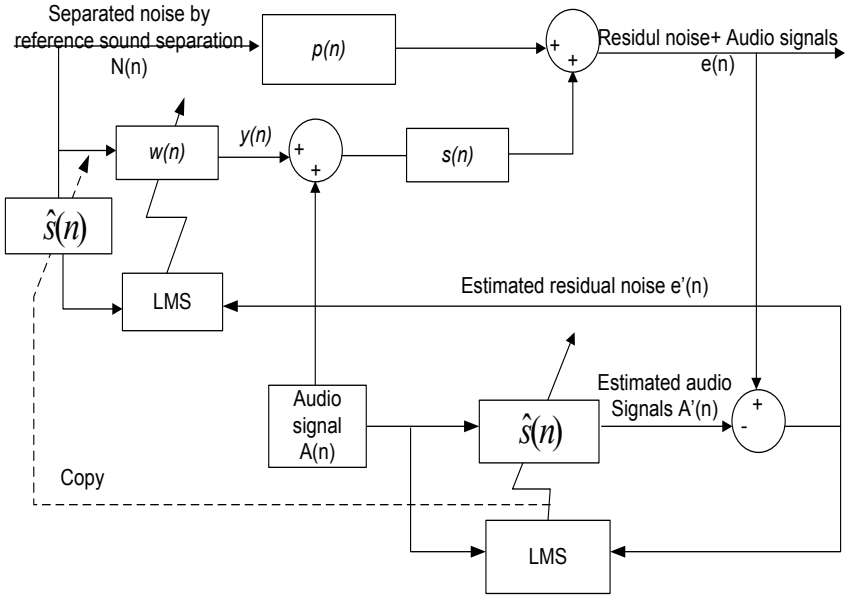

Figure 2-9 Schematic of the proposed ANC system integrated with secondary path transfer function estimation using source audio signals.

Another method to estimate the secondary path transfer function involves the injection of white noise into the ANC system. The schematic of the ANC system integrated with secondary-path estimation by additive white noise is shown in Figure 2-10. Similar to the estimation by audio signals, the LMS adaptation law for $\hat{s}(n)$ is given as:

$$\hat{s}(n+1) = \hat{s}(n) + \mu_{s_2} G(n) e'(n) = \hat{s}(n) + \mu_{s_2} G(n)[G(n)s(n) - G(n)\hat{s}(n)] + \mu_{s_2} G(n)[A(n)s(n) - A(n)\hat{s}(n)] + \mu_{s_2} G(n) N_r(n) \quad (2\text{-}25)$$

where μ_{s_2} is the adaptation step size, *G(n)* is the white noise, and $N_r(n)$ is the residual noise after ANC defined the same as in Equation (2-24). The expected value of $\hat{s}(n)$ will

converges to its optimal solution *s(n)* if *G(n)* is uncorrelated with $N_r(n)$ and the expectation of residual noise approaches to zero after ANC. Since *G(n)* is independently added white noise, it is guaranteed that *G(n)* will not be correlated with the residual noise $N_r(n)$. Thus the potential estimation failure caused by correlated audio signals and noise will not happen to the estimation using additive white noise. However, adding white noise to the ANC system will generate some unwanted sound, which could be annoying to home dwellers, whereas using the readily available source audio signals does not cause any disturbance.

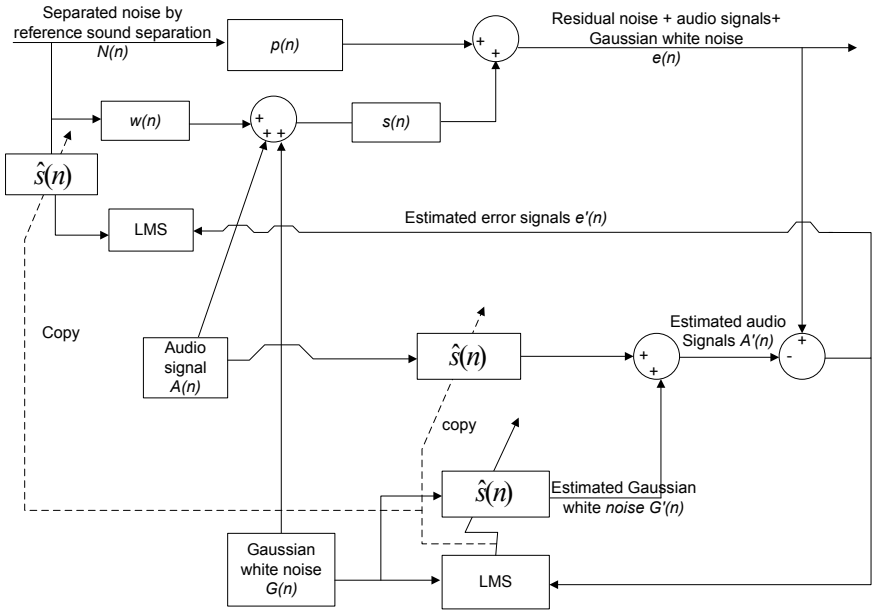

Figure 2-10 Schematic of the proposed ANC system integrated with secondary path transfer function estimated using additive white noise.

2.7 Experimental Results of Simultaneous Audio Playback and ANC[*]

2.7.1 Experiment Setup

The setup of the proposed ANC system for simultaneous window active noise cancellation and audio playback is shown in Figure **2-11**. A 1.1m×0.9m×2m cabin with a window (20cm×20cm) on one side is used to simulate a room under the impact of noise. The transparent thin film speaker is placed right next to the window pane inside the cabin and is driven by the summation of audio signals and active noise control signals. A woofer speaker is located outside of the cabin to simulate the external noise source. A pair of omni-directional microphone is placed on the outer side of the window and works with the wave separation algorithm to separate the reference signals from the "polluted" reference measurement. Another microphone located inside the cabin is the error microphone. The online estimation of secondary path is integrated with the FXLMS algorithm to eliminate audio signals picked up by the error microphone. The microphone outputs were pre-amplified and filtered before entering the data acquisition card. A CIO-DAS 6402/12 (Measurement Computing, Norton, MA) data acquisition was used for data communication between a PC and speakers/microphones. The control algorithms were implemented via a PC with a RT-Linux operation system. The sampling period was 150μs.

[*] This section contains contents published in [1] Hu, S., Rajamani, R., & Yu, X. (2013). Directional cancellation of acoustic noise for home window applications. *Applied Acoustics*, *74*(3), 467-477. Copyright 2013 Elsevier. Reused with permission. [2] This section contains contents published in Hu, S., Rajamani, R., & Yu, X. (2012). Invisible speakers in home windows for simultaneous auxiliary audio playback and active noise cancellation. *Mechatronics*, *22*(8), 1031-1042. Copyright 2012 Elsevier. Reused with permission.

Unlike the traditional ANC systems, which use direct microphone measurements for the reference and the error signals, the proposed ANC system utilizes the separated external noise by the wave separation algorithm for the reference signals and use the estimated residual external noise for the error signals to compute the control signals. It is expected that with all the add-ons, audio signals entering the control loop could be reduced, and that ANC and audio playback could be accomplished simultaneously without distorting audio signals and degrading active noise cancellation performance.

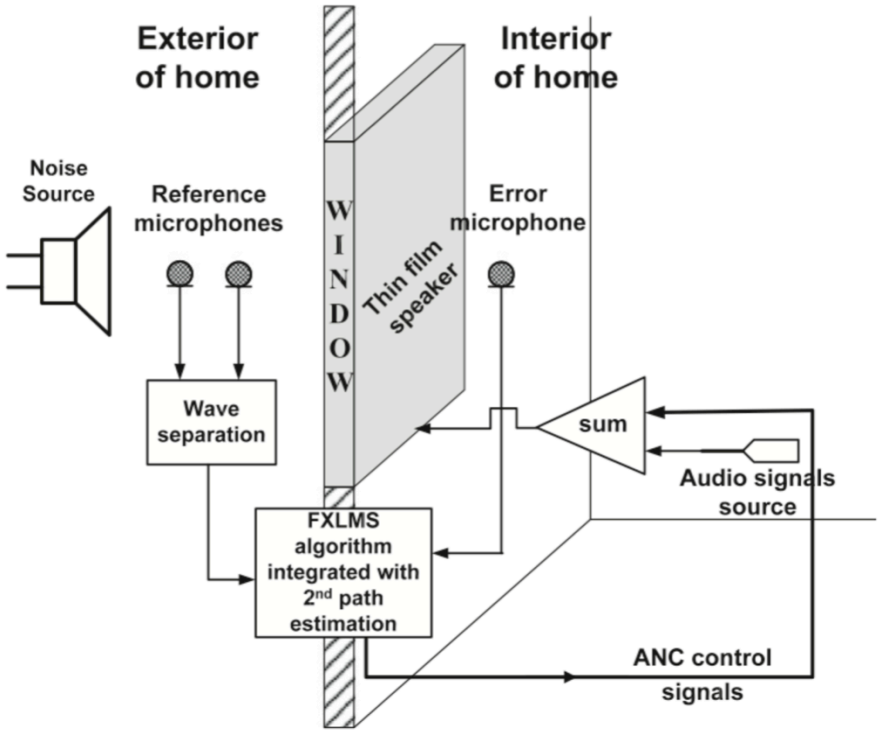

Figure 2-11 The setup of proposed ANC system for simultaneous audio playback and window active noise cancellation

2.7.2 Experimental Verification of the Wave Separation Algorithm

The reference microphone pair was separated by a distance d=6.35cm. As required by the wave separation algorithm, this distance d was chosen to make sure it was

smaller than the smallest wavelength of the sound. Experiments were conducted to verify the effectiveness of the wave separation algorithm. For the first experiment, a 600 Hz sinusoidal audio signal was played by the transparent speaker, and 550 Hz sinusoid was created from the external noise speaker. It is expected that external noise (550 Hz) in the reference measurement should be kept the same before and after the wave separation, whereas audio sound (600Hz) in the reference measurement should be eliminated by the wave separation. Figure **2-12** (a) and (b) compare the reference signals before and after separation in time and frequency domain. In time domain, the beat phenomenon caused by mixing 600Hz and 550Hz sound disappeared after the separation, leaving the reference measurement dominated by the external noise (550Hz). In frequency domain, the magnitude of the audio sound (600Hz) was reduced by almost 20dB in the reference measurement after the wave separation. The magnitude of external noise (550Hz) was slightly decreased by about 3dB because of the wave separation, which might be due to the imperfect normal incidence of sound and the fact that the sound in the acoustical field is a three-dimensional wave instead of a one-dimensional plane wave.

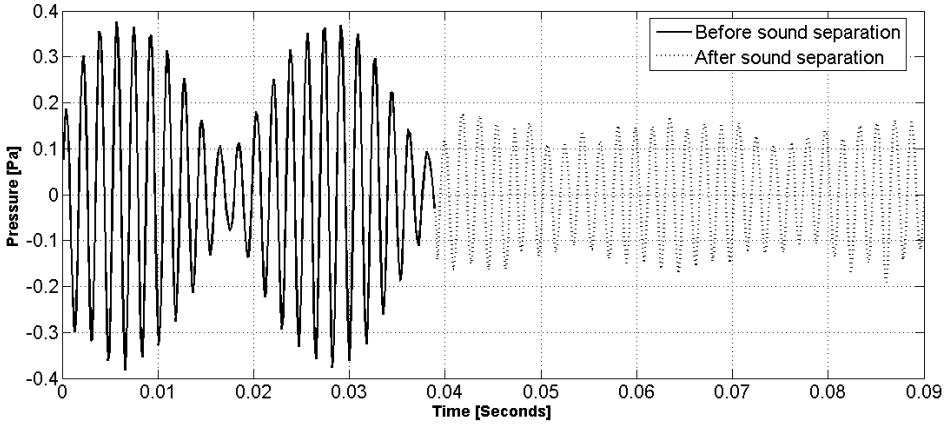

(a)

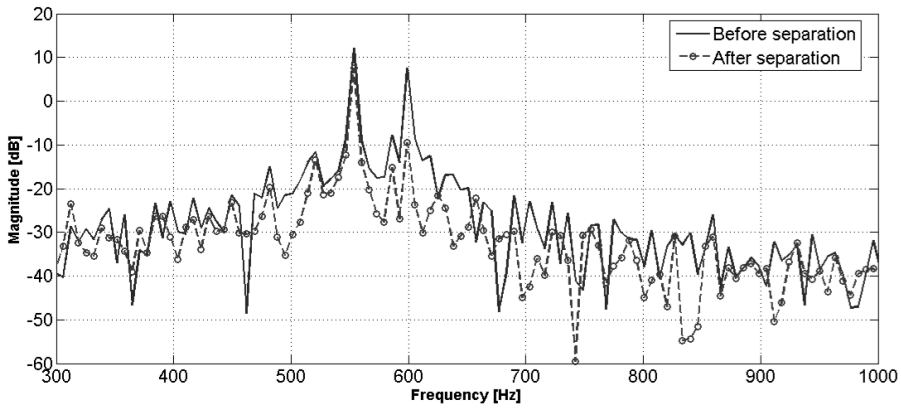

(b)

Figure 2-12 Wave separation algorithm eliminated audio sound (600Hz) but kept external noise (550Hz) in the reference measurement; (a) the reference measurement before and after separation result in time domain, and (b) in frequency domain.

Since the external noise and the audio sound are usually broadband, a second experiment was conducted to test the separation algorithm's effectiveness when dealing with broadband sound. Broadband sound with overlapping frequencies will make it difficult to distinguish between audio sound and external noise before and after the wave separation. To better demonstrate how wave separation algorithm works with broadband sound, sound without overlapping frequencies was used. For this test, the external noise was 800-1100 Hz broadband, and the audio sound was 400-700 Hz broadband. It is expected that after the wave separation, the magnitude of 400-700 Hz components in the reference measurement will be reduced, whereas the magnitude of 800-1100 Hz components should be kept at the same level as before the wave separation. Figure **2-13** (a) and (b) compare the reference measurement before and after the wave separation in time and frequency domain. The average magnitude decrease for 400-700 Hz components (audio sound) was about 10 dB. For 800-1100 Hz components (external noise) the average reduction was only 4 dB.

Experiments in the two scenarios verify that the wave separation algorithm can effectively separate external noise from the direct microphone measurements. This can help reduce the adverse effects on ANC introduced by the reference signals "polluted" by the audio sound or other sound generated inside the building. The wave separation algorithm did also decrease the external noise in the reference measurement by a few decibels in both experiments. However, the reduction was insignificant compared to the decrease of audio sound.

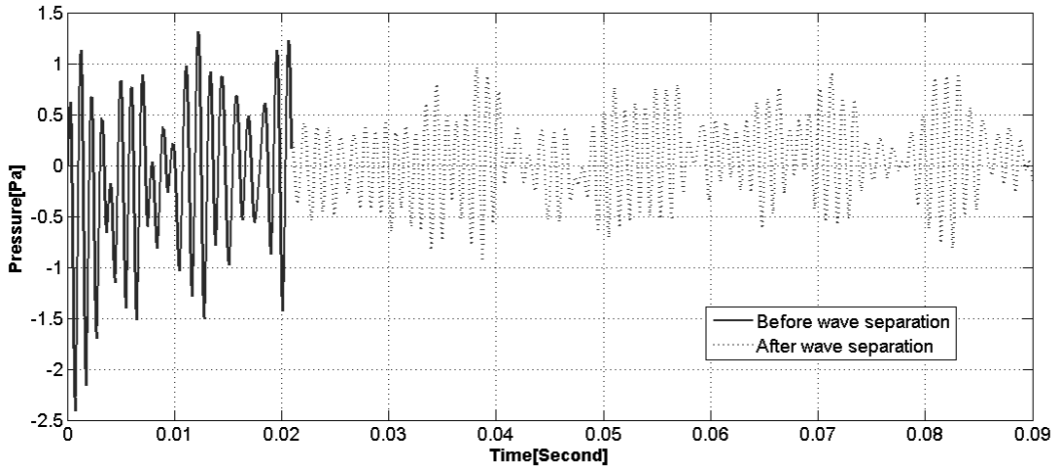

(a)

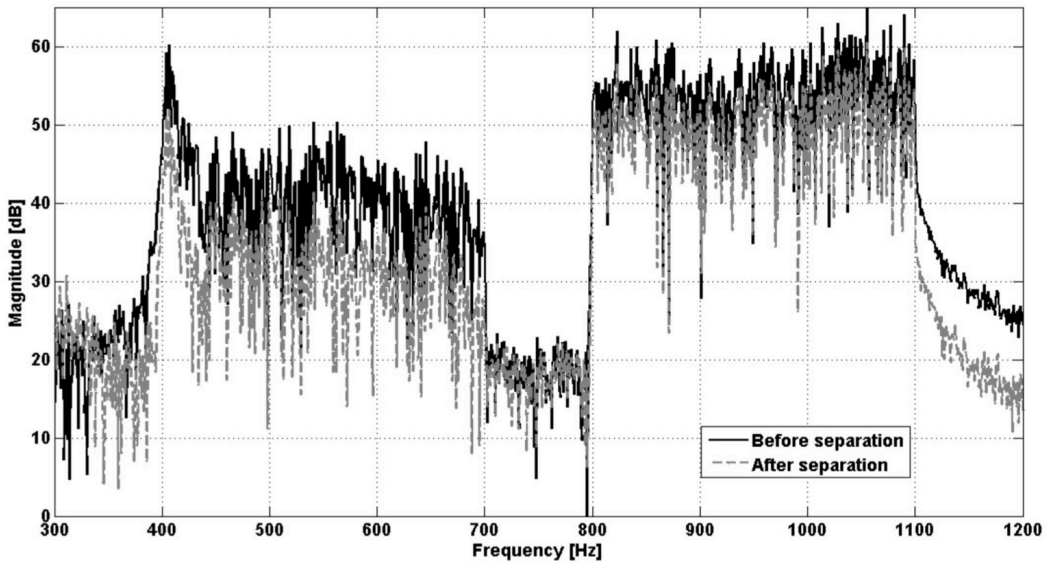

(b)

Figure 2-13 Wave separation algorithm eliminated broad band audio sound (400-700 Hz) but preserved broadband external noise (800-1100 Hz broadband) in the reference measurement; (a) the reference measurement before and after the wave separation in time domain, and (b) in frequency domain.

Finally, the frequency response of the new reference measurement system (including the reference microphone, the pre-filtering circuit, the data sampling, and the wave separation algorithm) was experimentally measured by swept sine testing. The original reference measurement system with just the microphone was also measured for comparison. A sine sweep wave was fed to the external noise source speaker. This signal was used as an input to compute the frequency response amplitude at each frequency. For the original system without the wave separation, the output is the direct microphone measurement. For the new system, the output is the estimated external noise obtained from the wave separation algorithm. Both frequency responses are compared in Figure **2-14**. The low magnitude in frequency < 100Hz in both systems is due to the use of a high pass filter with cut-off frequency at 100Hz. The high pass filter is used to suppress the 60Hz power line noise and low frequency baseline drift. Although the frequency response is slightly shifted downwards (magnitude is reduced) by the wave separation, the shape of the sensing system with wave separation matches with that of the original system very well. It demonstrates that the wave separation algorithm introduces little distortion to the frequency response of the original sensing system. The resulting magnitude can be easily scaled to match the new system with the original one.

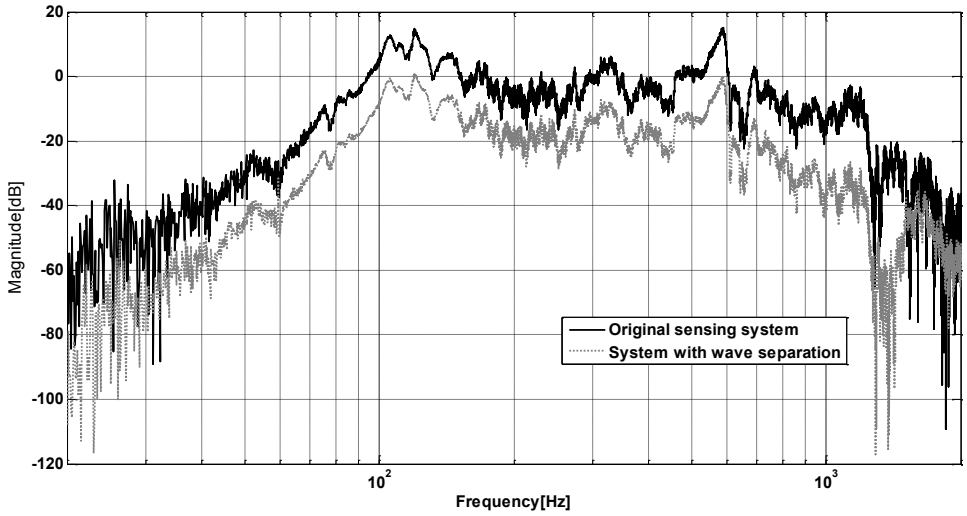

Figure 2-14 Comparison of frequency response of the reference measurement systems with and without wave separation

2.7.3 Experiments on Estimation of Secondary Path Transfer Function

Since estimation of the secondary path transfer function $s(n)$ is the key to the success of simultaneous audio playback and active noise control, an experiment was performed to validate this estimation. $s(n)$ estimated by additive white noise and source audio signals will usually converge to slightly different optimal values because of different signal content in the white noise and audio signals. Generally speaking, $s(n)$ estimated using additive white noise is closer to the true value than that using the source audio signals, because white noise has broader frequency band than audio signals and additive white noise is guaranteed to be uncorrelated with the residual noise as discussed in Section 2.6. Result of $s(n)$ estimated by white noise is demonstrated here.

The frequency response of $s(n)$ estimated by additive white noise is given in Figure 2-15. It shows that the secondary path has components consisting of a second order high pass filter with cut-off frequency around 500 Hz, a pure time delay, and two second order low pass filters with cut-off frequency at around 1000 Hz. The high pass filter behavior is

introduced by the thin film speaker, as shown in the frequency response of the thin film speaker in Figure **2-16**. The time delay is introduced because of the sound transmission delay between the thin film speaker and the error microphone. The low pass filters correspond to the two low pass filters (cut-off frequency 1143 Hz) in the signal conditioning circuits used for the error microphone and the thin film speaker. The low pass filters were used to suppress high frequency harmonics. The cut off frequency at 1143 Hz is chosen because traffic noise is mainly low frequencies below 1000 Hz. Based on the above analysis of the characteristics of the secondary path, it can be concluded that the transfer function estimated by additive white noise effectively models the dynamics of the secondary path.

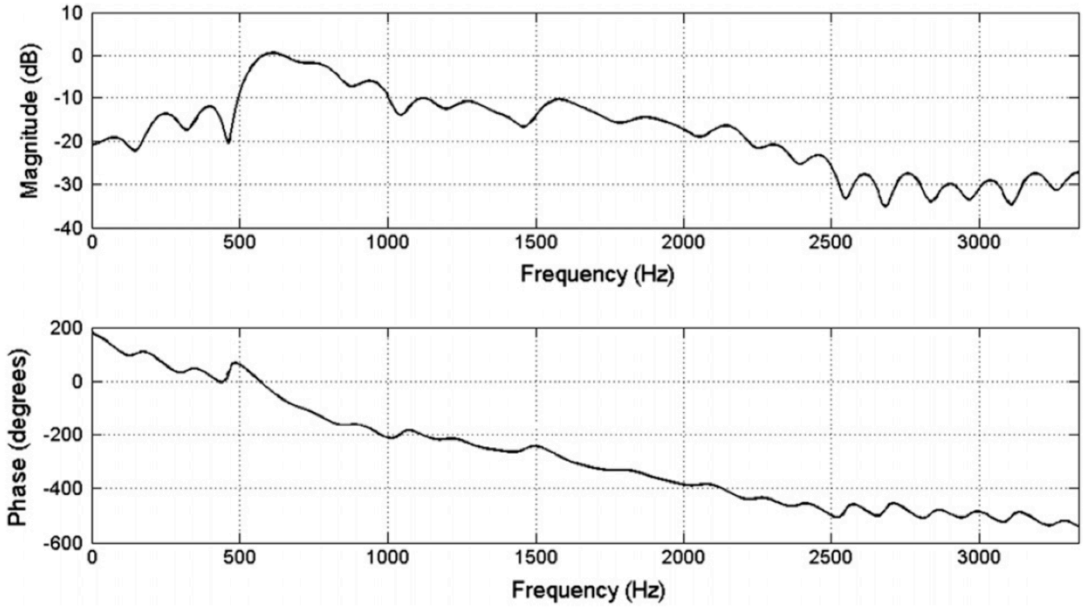

Figure 2-15 Frequency response of secondary path transfer function $s(n)$ estimated by additive white noise

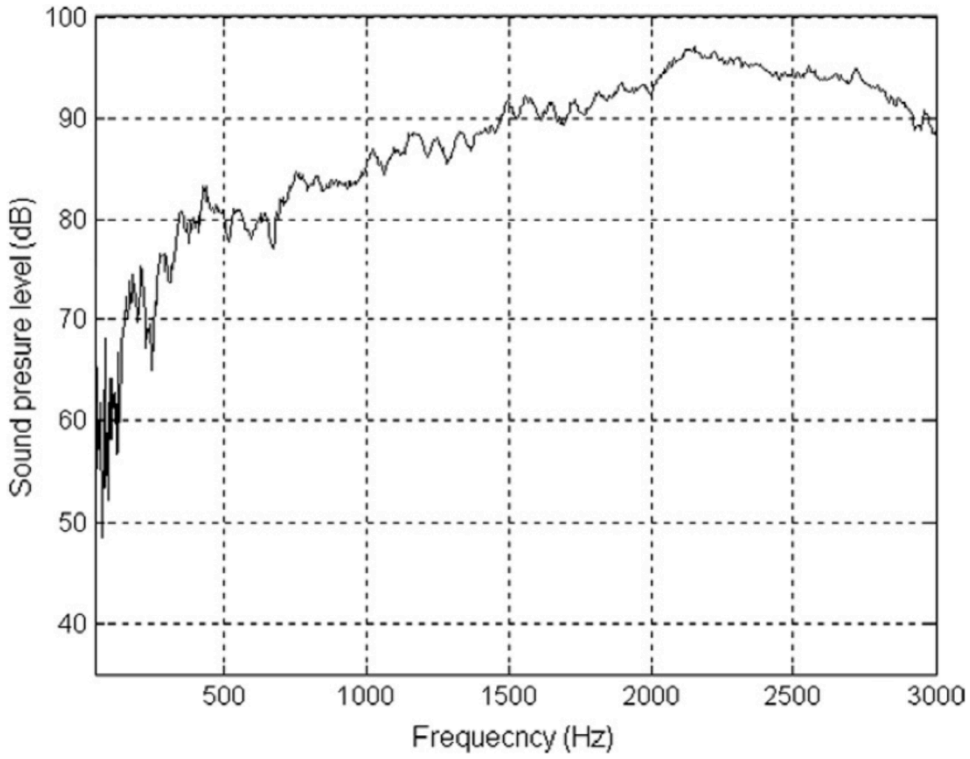

Figure 2-16 Measured frequency response from the thin film speaker that is excited by a 12 V_{rms} white noise signal.[39] (© 2007 IEEE. Reuse with permission)

2.7.4 Experiments on Simultaneous ANC and Auxiliary Audio

Experiments were performed to verify that the proposed ANC system could effectively prevent distortion of audio signals and deterioration of noise controller's performance. To verify that the proposed ANC system can effectively prevent distortion of audio signals and deterioration of noise controller's performance, two experiments were conducted in two scenarios: (1) playing single-frequency audio signals and single-frequency noise; (2) repeat but substitute the single-frequency audio signals with broad-band signals. As a measure of effectiveness, the sound in the cabin before and after the active noise control started was recorded and analyzed. To check the controller performance, control signals generated by the ANC systems were also collected. For

comparison purposes, the original ANC system was tested along with the proposed ANC system. In all the tests, the FXLMS filter has filter length of 48 and step size of 1×10^{-7}. In the first experiment, audio signals are the mix of 600Hz and 800Hz components, and the external noise is 700Hz. Figure 2-17 (a) is the noise control results from the traditional ANC systems. Figure 2-17 (b) shows the noise control results from the proposed ANC system integrated with the wave separation and the estimation of secondary path by source audio signals. Figure 2-17 (c) is similar to Figure 2-17 (b) except that the ANC system used additive white noise for secondary path estimation. Comparing the three control results, the proposed ANC system using source audio signals gives the best cancellation performance on unwanted 700Hz noise (~20dB). Reduction of 700Hz magnitude was about the same (~10db) for the traditional ANC system and the proposed ANC system using additive white noise for secondary path estimation. However, extra noise at about 510Hz and 850Hz appeared inside the cabin after the current ANC system started (marked by arrows in Figure 2-17 (a)). Figure 2-17 (d) compares the noise control signals generated by the three systems. The unwanted control strength exerted to cancel the desired audio signals was the highest (~20dB at both 600Hz and 800Hz) for the traditional ANC system. The traditional ANC system also produced control signals at around 510Hz and 850Hz, which introduced extra noise to the sound in cabin. The proposed ANC system using source audio signals hardly produced any control strength to cancel the desired audio signals.

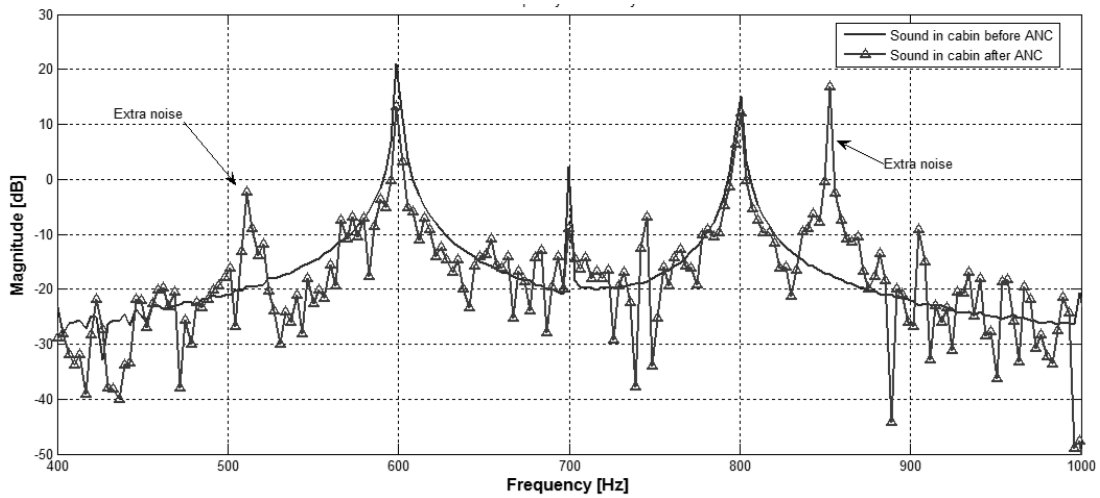
Sound in cabin before ANC
Sound in cabin after ANC
Extra noise
Extra noise
Magnitude [dB]
Frequency [Hz]

(a)

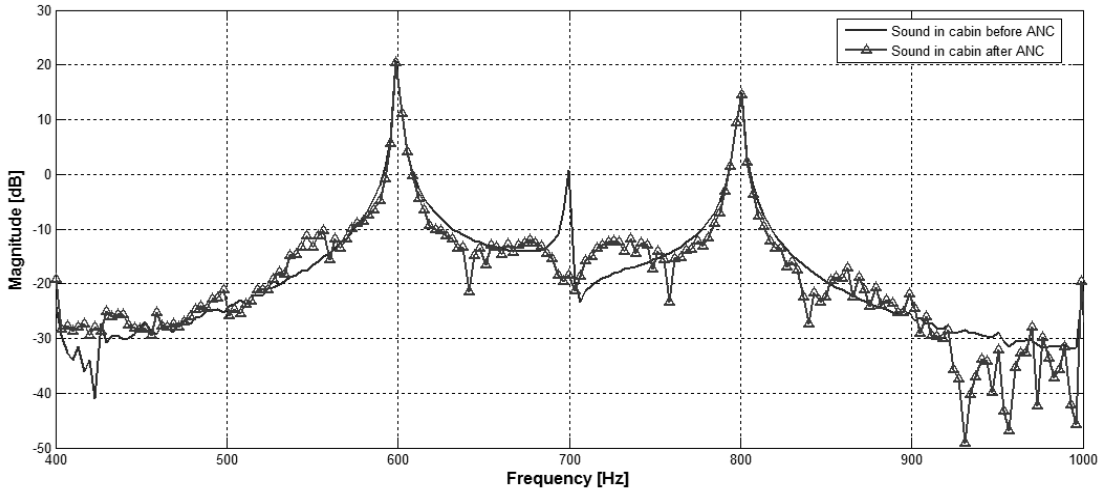
Sound in cabin before ANC
Sound in cabin after ANC
Magnitude [dB]
Frequency [Hz]

(b)

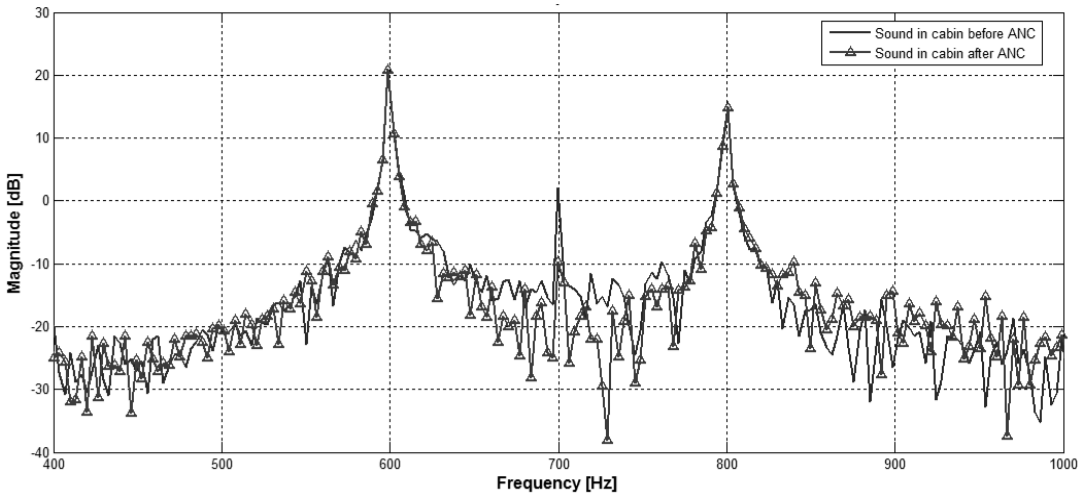
Sound in cabin before ANC
Sound in cabin after ANC
Magnitude [dB]
Frequency [Hz]

(c)

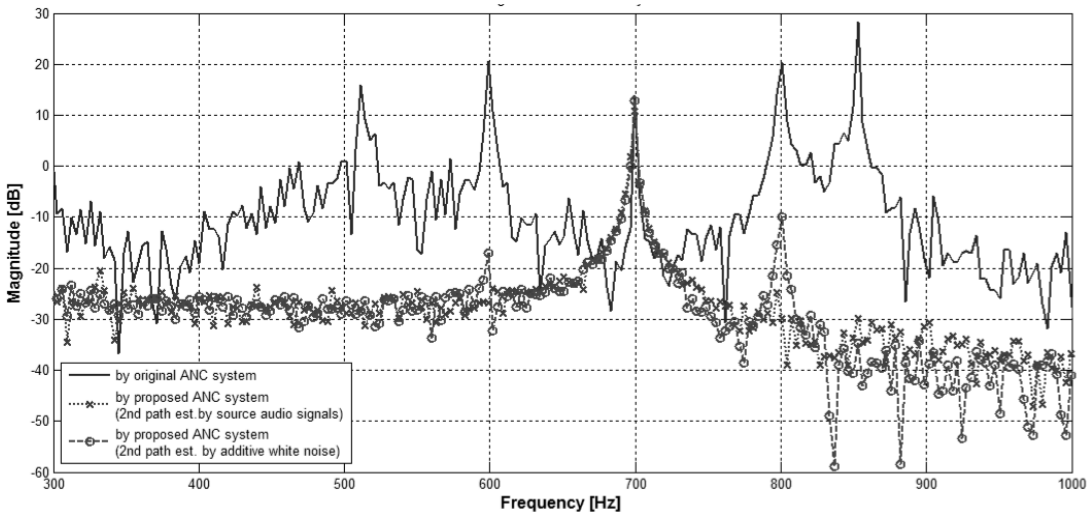

(d)

Figure 2-17 Control outcome of three ANC, (a) traditional ANC system, (b) proposed ANC system with wave separation and secondary path estimation by source audio signals, (c) similar ANC system with (b) but using additive white noise for secondary path estimation, (d) control signals generated by three ANC systems.

The second experiment tested the effectiveness of the ANC system when dealing with broadband sound. In this test, the simulated audio sound was 400-700 Hz broadband while the external noise was 800-1100Hz broadband. Figure **2-18** (a) is the sound in cabin in frequency domain before and after ANC: the broadband internal sound was well preserved (the average reduce of magnitude was only 0.0109dB), but the broadband external noise was successfully cancelled (the average magnitude reduce was more than 6 dB). Figure **2-18** (b) is the control signal, which shows that the controller mainly produced 800-1100 Hz “anti-noise” targeted at cancelling external noise.

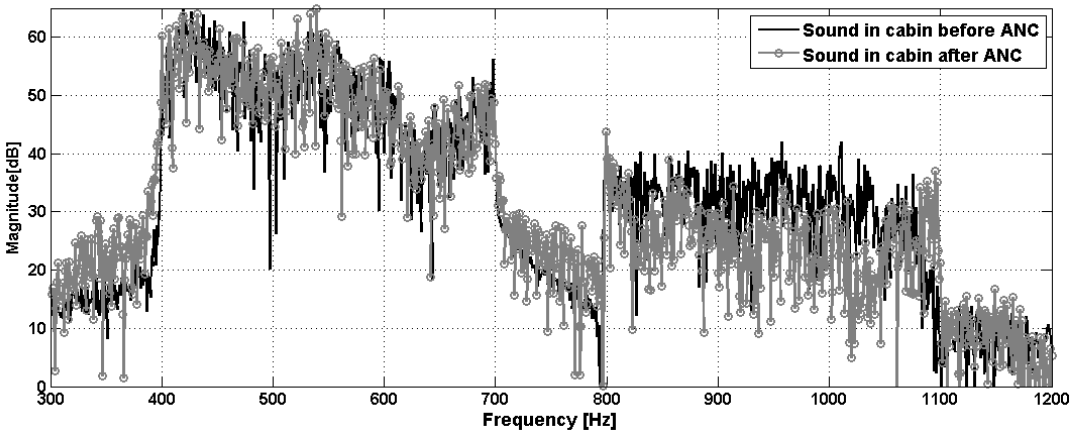

(a)

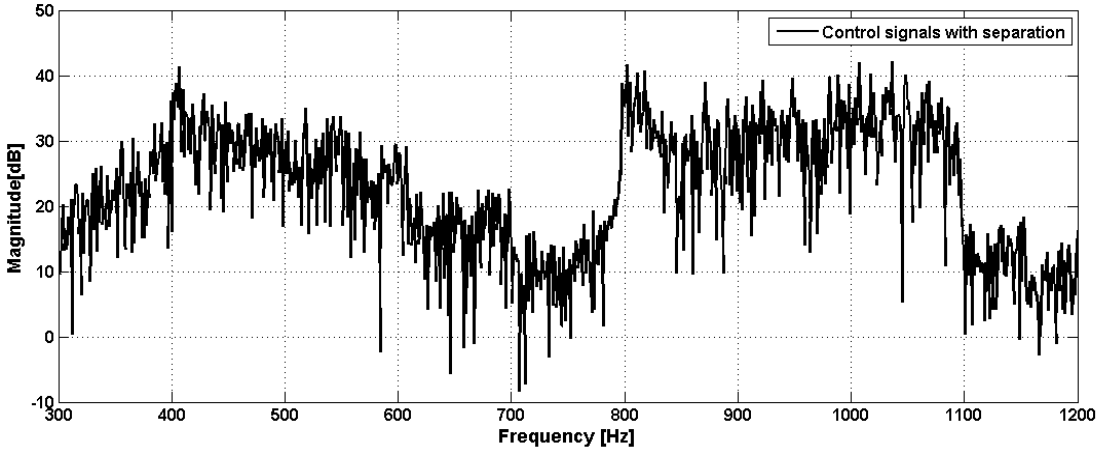

(b)

Figure 2-18 Control outcome of the proposed ANC systems, when audio sound was 400-700Hz broadband and external sound was 800-1100Hz broadband; (a) external noise level was reduced while audio sound was well preserved; (b) control signals produced by the proposed ANC.

3 Thin Flexible Solid-State CNT-Based Supercapacitors

3.1 Introduction to Supercapacitor

The typical structure of a supercapacitor (or an electric double layer capacitor) is shown in Figure 3-1(a). It usually consists of two electrodes and a non-conductive layer called separator to prevent the shorting of two electrodes. The separator is soaked in an electrolyte solution. The separator has to be porous so that ions in the electrolyte can move freely through it. When a bias voltage is applied to the two electrodes, a layer of positive charge builds up at the surface of the positive electrode, attracting a layer of negative ions from the electrolyte. Thus an electric double layer is formed at the interface between the positive electrode and the electrolyte. The same happens at the negative electrode. The capacitance of each electric double layer can be calculated by the capacitance equation for a parallel-plate capacitor

$$C = \frac{\varepsilon_r \varepsilon_0}{d_{EDL}} A \tag{3-1}$$

where ε_r is the dielectric constant of the electrolyte, ε_0 is the permittivity of a vacuum, A is the surface area of the electrode accessible to ions in the electrolyte, and d_{EDL} is the effective distance between positive and negative charges in the electric double layer. Unlike the supercapacitor, Figure 3-1(b) is the schematic of a dielectric parallel-plate capacitor. It consists a layer of non-conductive dielectric materials sandwiched between two parallel plate electrodes. No electric double layers form during charging and discharging and the distance between positive and negative charges is the thickness (d) of dielectric material. Note that d cannot be very small otherwise the capacitor will have an

electric breakdown voltage too low to be of practical use. On the other hand, since d_{EDL} is at the level of atomic size, much smaller than d, the capacitance of supercapacitors is significantly larger than that of dielectric capacitors.[49] To further increase the capacitance, electrode area A can be increased by using high surface area material as electrodes.

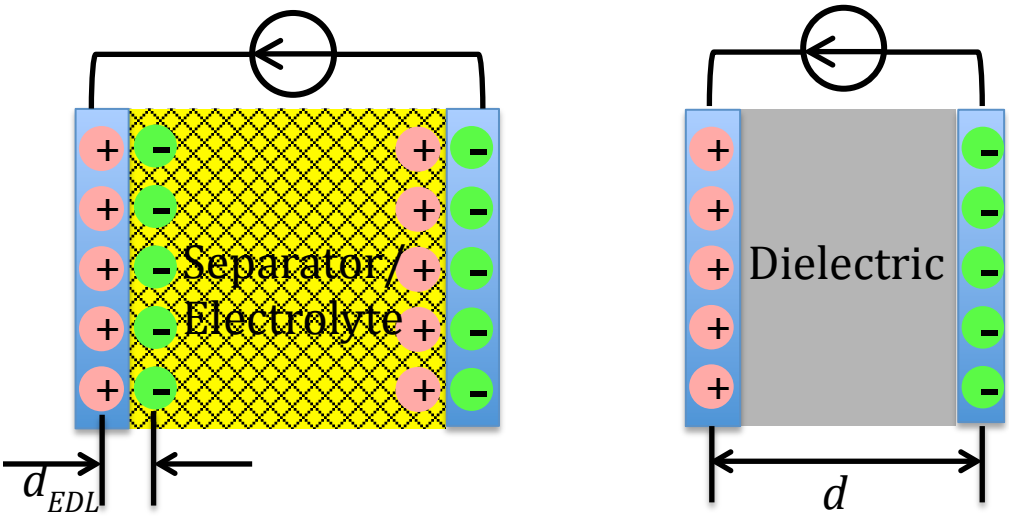

(a) (b)

Figure 3-1 Comparison of device structures between an electric double layer capacitor (EDLC) and a dielectric capacitor. a) Schematic of an EDLC being charged; b) Schematic of a dielectric capacitor being charged.

3.2 Necessity of Supercapacitors for the Solar-powered ANC System

Unlike ambient random noise, which has low power density but long duration, airport noise usually has high power density and short duration. For example, at 100 m from an aircraft taking off, the noise power density can reach 0.1 Watt/m^2 (110dB) and the total take off time is usually less than 1 minute.[50] As a result, the stored solar energy needs to be extracted at a fast rate (high power) during real-time noise cancellation. Introducing supercapacitors into the solar energy storage system can mitigate the power

density problem. Supercapacitors are energy storage devices with much higher power density than batteries. They can be charged by the solar cells at a slow rate and later discharge the energy to the real-time ANC system at a fast rate to meet its power requirements. In fact, supercapacitors have been used in electric vehicles (EV) to provide large power during acceleration. However, the supercapacitors used in EVs are bulky, rigid, and heavy, and are difficult to be integrated into the window ANC system. Hence, thin, flexible, and lightweight supercapacitors, which can be easily mounted on any arbitrary surfaces, are needed for the window ANC application.

3.3 Review of Previous Work on Supercapacitors

Supercapacitors will be used to provide high power for the real-time window ANC system. Commercial supercapacitors are bulky and contain a liquid electrolyte system, which are difficult to integrate with the home windows. Thin and flexible supercapacitors can mitigate the problem, because they can fit anywhere and can even be mounted on the inner surfaces of the window frame. Some prototypes of thin flexible supercapacitors have been developed in literature. Hu et al prepared flexible paper-based electrodes by coating conductive SWNT solution onto both sides of a piece of printing paper pre-treated by polyvinylidene fluoride (PVDF). The SWNT/paper electrodes and the electrolyte (1M Lithium hexafluorophosphate in Ethylene carbonate and Dimethyl carbonate) were encapsulated in a coffee-bag cell to obtain a supercapacitor.[51] The use of liquid electrolyte is a drawback for the above flexible supercapacitor prototypes. Since the electrolyte is usually hazardous to the environment, good sealing of the electrolyte is required. To ensure stable supercapacitor performance, a good housing is also needed to

immobilize the electrodes with respect to each other. The sealing and housing materials add extra volume and weight to the supercapacitors, making them inefficient in terms of specific energy/power (energy/power stored per unit mass). The resulting bulky and rigid devices are unsuitable for applications, which require thin and lightweight components. Moreover, sealing and housing can reduce the flexibility of supercapacitors as well. To avoid the problems with liquid electrolyte, solid-state electrolyte will be used in this research. Different kinds of solid-state electrolytes have been studied in literature. As proposed by L.P. Ma et al, a thin film of metal salt electrolyte (e.g. Lithium fluoride) could be evaporated on copper electrodes to fabricate solid-state supercapacitors.[52] However, this evaporated electrolyte thin film is fragile and not suitable for use in a flexible device. A polymer-based electrolyte is another class of solid-state electrolytes that is very promising for flexible supercapacitors. Examples of polymer based electrolyte includes Poly (vinylidene fluoride-co-hexafluoropropylene)/1-Ethyl-3-methylimidazolium tetrafluoroborate and poly (vinyl alcohol) (PVA)/ phosphoric acid.[53-54] In this research an easy procedure will be presented to make thin, lightweight, flexible and solid-state supercapacitors suitable for the window-integrated solar cells application.

3.4 First Generation Flexible and Solid-state Supercapacitors: the Single-cell Parallel-Plate Type[*]

To fabricate flexible supercapacitors with high capacitance, SWNTs are used as flexible electrodes for supercapacitors in this research. SWNTs have large surface area,

[*] This section contains contents published in Hu, S., Rajamani, R., & Yu, X. (2012). Flexible solid-state paper based carbon nanotube supercapacitor. *Applied Physics Letters*, *100*(10), 104103. Copyright 2012, AIP Publishing LLC. Reused with permission.

which is highly accessible to ions in the electrolyte. In addition, SWNTs have good electrical and mechanical properties as well as good corrosion resistance. As discussed before, to avoid the use of aqueous electrolyte, which requires housing and sealing, solid-state polymer gel electrolyte is used in this research. The polymer provides a matrix in which ions can travel freely. The non-conductive polymer matrix also serves as a separator to prevent electrode shorting. A schematic of the proposed SWNT-based flexible solid-state supercapacitor is shown in Figure 3-2. It consists of a thin layer of polymer-based solid-state electrolyte sandwiched between two pieces of CNT-coated conductive paper. Paper functions as supporting materials for the SWNT thin film. Paper is chosen because it is lightweight, ubiquitously available, and environmentally friendly. More importantly, the intrinsic hydroxyl groups on the paper cellulose can form hydrogen bonds with the carboxyl groups on the acid functionalized SWNT (Figure 3-3).[55-56] The hydrogen bonding could reduce delamination of SWNT into the electrolyte during charging/discharging (further discussed in Section 3.8).

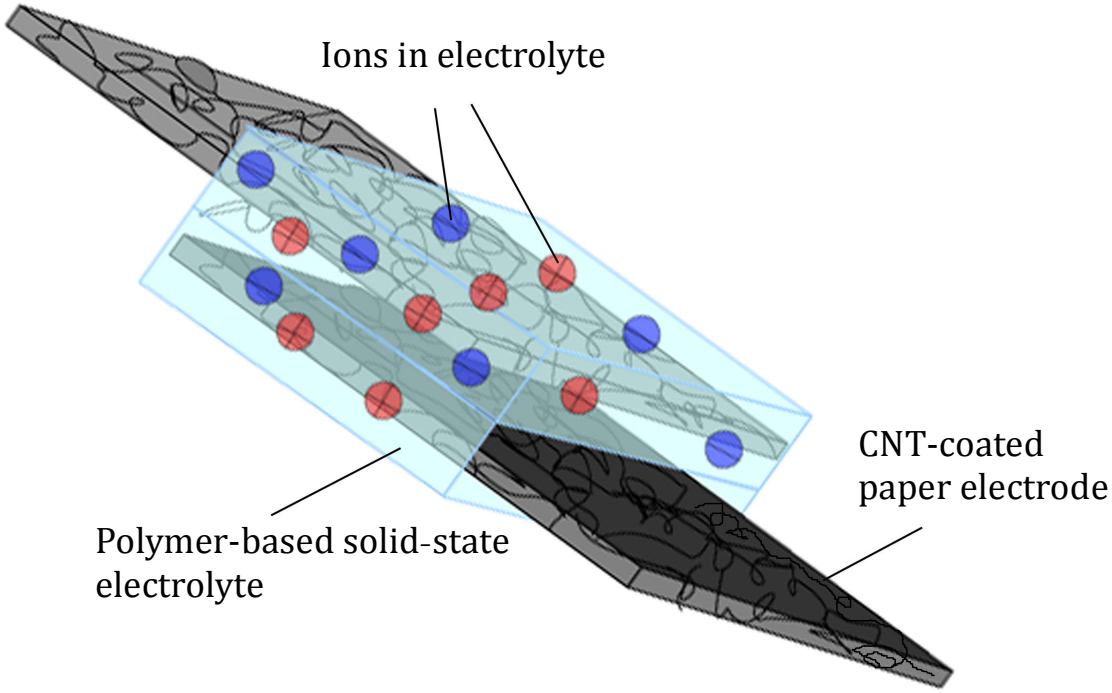

Figure 3-2 Proposed SWNT-based flexible solid-state supercapacitor.

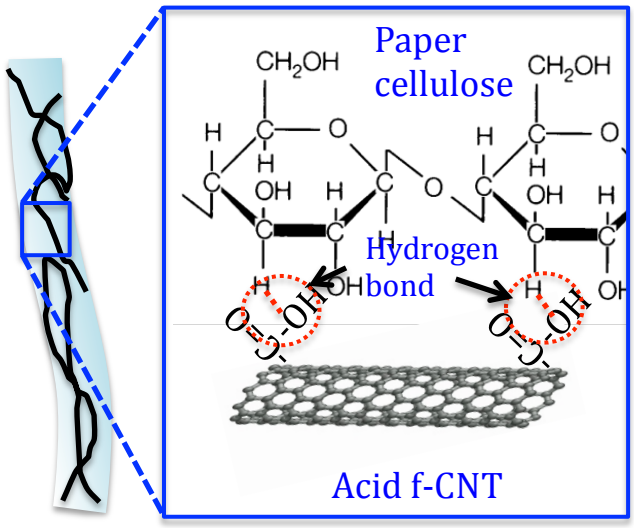

Figure 3-3 Schematic of hydrogen bonding between acid functionalized CNT and paper cellulose.

3.5 Fabrication Process of First Generation Supercapacitor

Figure 3-4 shows the fabrication process of the proposed supercapacitor. High purity SWNT powder (<10% impurities) synthesized by chemical vapor deposition was purchased from Timesnanoweb (Chengdu, China) and used as received. Then a solution-based method was used to coat SWNT on compliant substrates. For this, the SWNTs needed to be evenly dispersed into water by functionalization. Using a noncovalent, surfactant-based functionalization method can risk making the supercapacitor unstable because the surfactant might react with the electrolyte. Instead, we used covalent method: the oxidative purification method. Specifically, 200 mg SWNTs were added to 80 ml of oxidative acid mixture of sulfuric acid (98 wt%) and nitric acid (69 wt%) in a volume ratio of 3:1, and stirred for 2 hours on a 110^{o}C hot plate. The mixture was then diluted to 400 mL and the SWNTs were collected by membrane filtration and washed by DI water to remove residual acids. After acid treatment, the originally hydrophobic SWNTs became hydrophilic because carboxyl groups (-COOH) were attached to SWNT ends. Finally, the acid-treated SWNTs were uniformly dispersed into 40 mL of DI water through one-hour ultrasonic bath. When choosing compliant substrates for the flexible electrodes, paper rather than PET was chosen. Studies have been done to compare the coating of CNT thin film on PET and Xerox printing paper substrates. Results have suggested that the PET substrates showed poor bonding with the CNT and film delamination was observed, but coating CNT on Xerox printing paper was successful.[57] In this research, non-woven 100% cotton paper for cosmetic facial mask was used, because it has rough surface morphology, and is lighter and more absorbent than printing

paper. Initially, the cotton paper was cut into desired shape. To coat the cotton paper with SWNT, a simple dip-and-dry process was used: the cotton paper was dipped into the SWNT suspension and dried on 120 ^{o}C hot plate until excessive water was evaporated. This process was repeated until the sheet resistance of SWNT-coated cotton paper reached 9~10 Ω /□. The acid-treated SWNT bonded to the cotton fibers very well because the cotton fibers have hydroxyl groups that can form hydrogen bonds with the carboxyl groups on the acid treated CNT. For better electrical connection with the testing circuit, a small fraction of the electrodes was covered with silver conductive epoxy. To make PVA/phosphoric acid, 6 g of PVA powder (Mowiol® 18-88, Sigma Aldrich) and 1.6 g of phosphoric acid (69 wt%) were added to 40 ml of DI water and stirred on 85 ^{o}C hot plate until the mixture became a clear and glue-like gel. To assemble the supercapacitor cell, two SWNT-coated cotton electrodes were immersed into 85 ^{o}C PVA/phosphoric electrolyte. The silver epoxy-coated fraction was carefully kept away from the electrolyte. After 10 min the electrodes were taken out and assembled together face-to-face to achieve the maximum possible overlapping area. The assembly was dried in room temperature for 12 hours. Upon evaporation of excessive water, the original glue-like electrolyte solidified, forming a solid-state flexible supercapacitor. The PVA played two important roles in the fabrication process. It functioned as a binder to hold the supercapacitor assembly as one integrated part. It also acted as a separator to prevent electrode shorting. Figure 3-5 shows the as-fabricated solid-state supercapacitors with different shapes. The as-fabricated supercapacitor is very flexible and can be bent by

more than 90◦ without showing any fracture. The supercapacitor is also very thin with a thickness of only 1.3 mm.

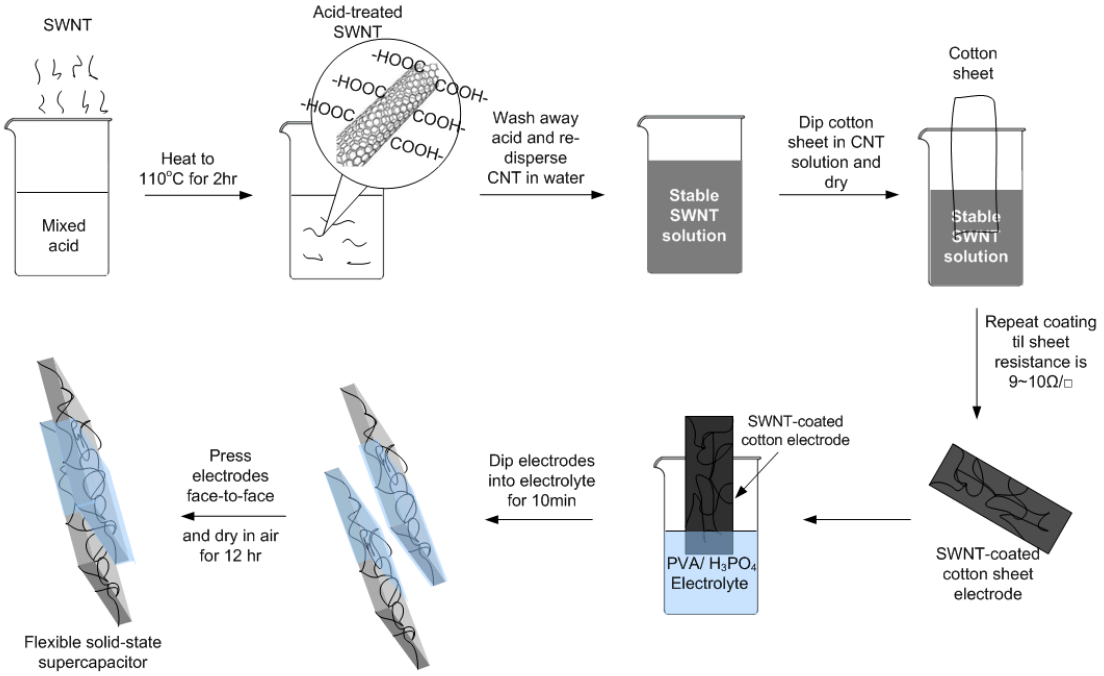

Figure 3-4 Fabrication process of the flexible and solid-state CNT-based supercapacitor

Figure 3-5 As-fabricated CNT-based supercapacitors with different shapes and great flexibility

3.6 Characterization of As-fabricated Supercapacitors

The performance of the as-fabricated supercapacitor (the rectangle shaped one in Figure 3-5) was tested using both cyclic voltammetry and constant current charging and

discharging with a two-electrode setup. In cyclic voltammetry (CV) test, the voltage across the supercapacitor under evaluation is ramped up/down at a constant rate, and the current passing the device is recorded alongside with the voltage. Using the CV curve (voltage vs. current curve), the capacitance (*C*) of the capacitor can be calculated by Equation (3-2).

$$C = \frac{\int_{V_1}^{V_2} i dv}{2(V_2 - V_1)^{dv}/_{dt}} \tag{3-2}$$

where V_1 and V_2 are the lower and upper limits during voltage ramping, i is the current, and $^{dv}/_{dt}$ is the constant voltage ramping rate.

In constant current charging-discharging (CC) test, a constant positive current is applied to the supercapacitor until it is charged to its maximum voltage, and then the current polarity is switched to negative until the supercapacitor is fully discharged. The voltage across the supercapacitor is recorded throughout the whole process. The CC test can also be used to calculate the device's capacitance by Equation (3-3)

$$C = \frac{I}{^{dU}/_{dt}} \tag{3-3}$$

where *I* is the charging/discharging current and $^{dU}/_{dt}$ is the voltage rate of changing or the slope of the CC curve (voltage vs. time). In addition, the equivalent series resistance (ESR) of the device can also be calculated the CC curve. During the CC test, when the current polarity is changed, there is a step change of the voltage across the supercapacitor (the IR drop), similar to the voltage change when the current passing a resistor switches polarity. In a two-electrode test setup, the ESR can be calculated from the IR drop by Equation (3-4)

$$ESR = \frac{U_{IR}}{2I} \tag{3-4}$$

where U_{IR} is the IR drop and I is the constant charging/discharging current. With the CV and CC curves, the maximum energy stored in a capacitor can also be calculated from Equation (3-5)

$$E = \frac{CU_{MAX}^2}{2} \tag{3-5}$$

where C is the capacitance and U_{MAX} is the maximum voltage the supercapacitor can be charged to. For cross comparison, specific capacitance and energy (capacitance and energy per unit weight of active materials or the whole device) are also calculated from the CV and CC tests. For a two-electrode test setup, specific capacitance C_s with respect to the weight of active materials or the weight of the whole device are calculated by Equations (3-6) and (3-7)

$$C_s = \frac{4C}{m_a} \tag{3-6}$$

$$C_s = \frac{C}{m} \tag{3-7}$$

where m_a is the weight of active materials and m is the weight of the whole device. Similarly, specific energy E_s can be calculated by Equations (3-8) and (3-9)

$$E_s = \frac{2CU_{MAX}^2}{m_a} \tag{3-8}$$

$$E_s = \frac{CU_{MAX}^2}{2m} \tag{3-9}$$

Figure 3-6 shows the CV test results of the as-fabricated supercapacitor at different scanning rates of 8mV/s, 4mV/s, and 2mV/s. As shown in the CV curves, the supercapacitor has both capacitive and resistive properties due to its large ESR.

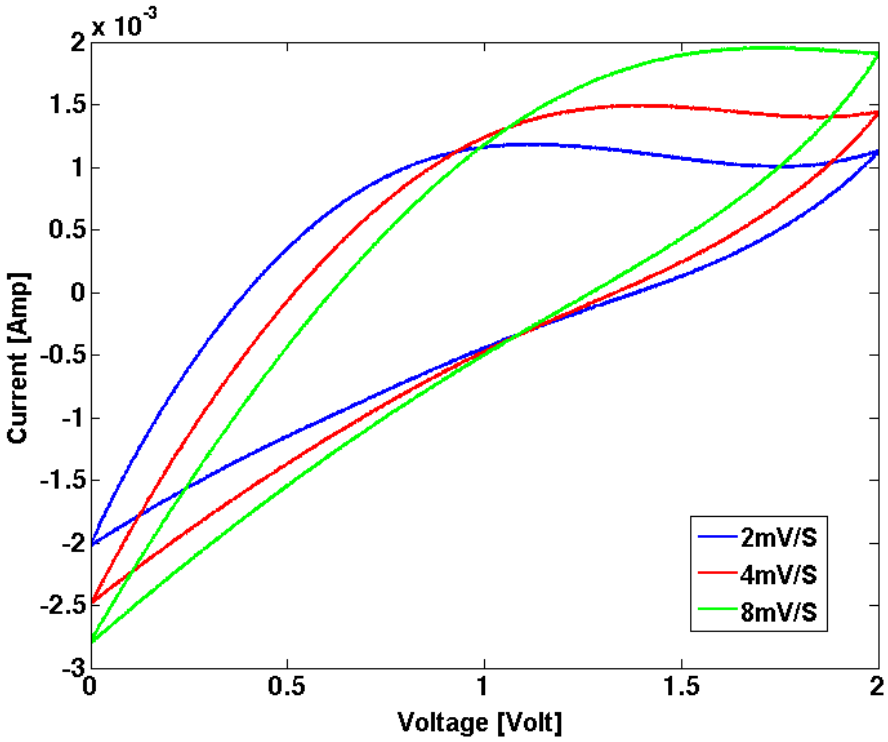

Figure 3-6 Cyclic voltammetry of the as-fabricated supercapacitor at different scanning rates.

Five cycles of CC curve at 2mA are shown in Figure 3-7. Specific capacitance, specific energy, and ESR of the supercapacitor were all computed from the CC curve. The weight of active materials m_a used in the calculation is the mass of acid-treated SWNT, which is obtained by comparing the weight of the cotton paper before and after SWNT coating. The same applies for specific energy (E_s). For the rectangle shaped supercapacitor in Figure 3-5, the total mass of SWNT on both electrodes was 122.40 mg. The specific capacitance of the as-fabricated supercapacitor was 115.83 F/g and specific energy was 48.86 Wh/kg. Supercapacitors using MWNT-based electrodes with specific capacitance in the range of 4-137F/g were found in literature.[58] For SWNT-based electrodes, a maximum specific capacitance of 180 F/g was found in literature.[59] The

performance of the developed supercapacitor was also compared with some of the best commercial supercapacitors (Table 3-1). The performance of the as-fabricated supercapacitor is in the same range as the best research and commercial supercapacitors, and the developed supercapacitor has the unique property of being flexible, thin, and solid-state. However, its ESR is significantly larger than that of the commercial ones. High ESR will reduce the capacitor's power rate (the amount of energy uptake or discharge per unit amount of time), as explained by Equation (3-10).

$$P = U^2/ESR \tag{3-10}$$

Another drawback is that the working voltage of the developed supercapacitor is limited (1.7 V), which is not enough for a lot of real applications. For example, in automotive applications, the required voltage is 12 V. In fact, low working voltage is a common drawback for all research and commercial single cell supercapacitors. Depending on the electrolyte used, the maximum achievable working voltage for a single cell supercapacitor varies between 0.5 V and 4 V.

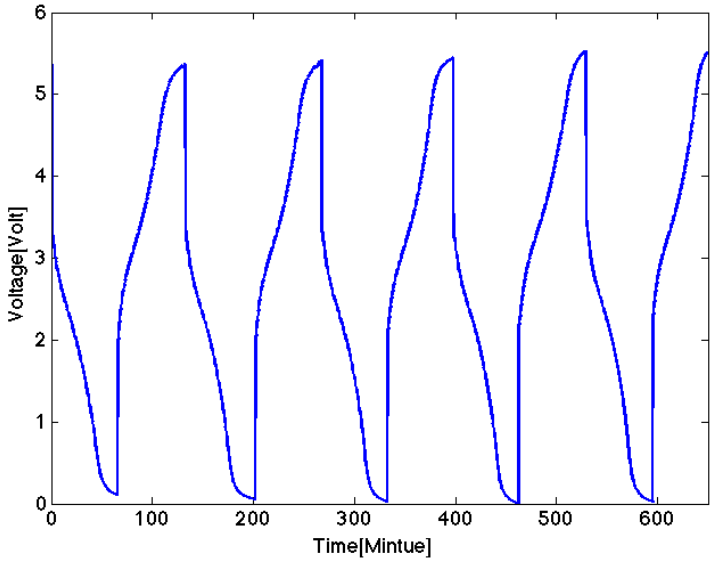

Figure 3-7 Galvanostat charging-discharging curves at 2mA

Table 3-1 Performance comparison between as-developed supercapacitor and commercial supercapacitors

	Commercial Supercapacitors		This work
	EPCOS B49410B-2506Q000 (organic electrolyte)	ESMA EC303 (aqueous electrolyte)	Flexible supercapacitor (solid-state electrolyte)
Weight of entire device (g)	1050	2600	1.08
Specific capacitance (F/g)	4.76	17.31	13.15
Specific energy (Wh/kg)	4.1	6.15	5.54
Working voltage (volt)	2.5	1.5	1.7
ESR (Ω)	0.35×10^{-3}	0.3×10^{-3}	117.73

3.7 High-voltage Multi-cell Supercapacitors

Both the working voltage and the amount of energy stored in a single supercapacitor are far from enough for many real applications. To reach the working voltage and the energy level required by many real-world systems, multiple parallel-plate supercapacitors are usually stacked together.[60,61,62] Figure 3-8 shows the schematic of a three-cell stacked supercapacitor. Bipolar electrodes, which act as positive/negative electrode for one cell and negative/positive electrode for the adjacent cell, electrically connect all the cells in series. Bipolar electrodes also serve as electrolyte barrier to isolate individual cell's electrolyte system. Although the number of cells is unlimited theoretically, adding more units onto a stack to meet requirements for higher voltage and stored energy will result in a very bulky device.

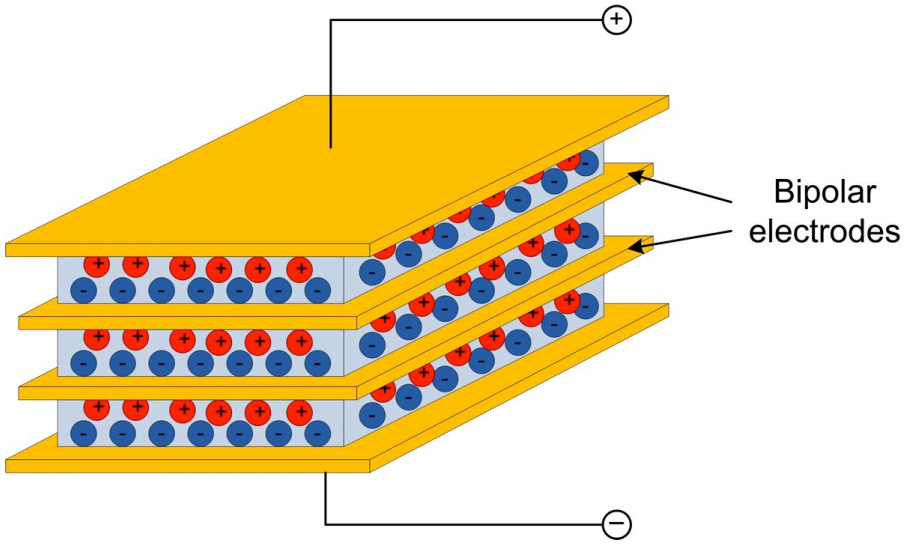

Figure 3-8 Schematic of stacked three-cell bipolar supercapacitors

3.8 Planar Supercapacitors

Planar supercapacitors have recently been proposed and have completely different device architecture than the parallel-plate supercapacitors. Parallel-plate capacitors have a three-dimensional architecture, in which a thin layer of electrolyte is sandwiched between two electrodes. Whereas for planar capacitors, both the electrodes are fabricated on one plane and an electrolyte film is deposited on top of the electrodes.[63,64] Multiple research groups have reported single cell planar supercapacitors using various active materials and electrolyte systems on different substrates. Feng Jun *et al.* fabricated a planar supercapacitor by vacuum filtration of vanadium disulfide (VS_2) nanosheets onto mixed cellulose membrane substrate, and applying a PVA/$BMIMBF_4$ electrolyte on top of the VS_2 layer.[65] Carbon materials such as reduced graphene oxide (RGO) sheets and pristine CNT were used as active materials for supercapacitors as well. Yoo Jung Joon *et al.* and El-Kady, Maher F., *et al.* drop cast graphene oxide (GO) solution on non-porous and non-

water-absorbing substrate (such as glass and PET). Then the GO was reduced to conductive graphene layer by a laser source or hydrazine hydrate chemical bath. Finally, PVA-acid (H_2SO_4 or H_3PO_4) electrolyte was deposited onto the RGO to produce planar supercapacitors.[66,67] Jiang, Y. Q. *et al.* grew CNT forests on silicon wafer by chemical vapor deposition (CVD) and utilized the CNT forests as planar electrodes and ionic liquid as electrolyte for their CNT-based planar supercapacitor.[68] It is difficult to fabricate the previously discussed planar supercapacitors onto wide variety of substrate materials, due to the limitation of their fabrication methods (e.g. CVD and laser treatment). Most of these methods are also not readily scalable to large sizes.

3.9 Second Generation CNT-based Supercapacitor: the High-voltage Multi-cellular Planar Type

So far planar supercapacitors reported in the literature have been single-cell devices.[63-68] In order to achieve a high-energy planar supercapacitor, a two-dimensional (2D) equivalence of the three-dimensional (3D) multi-cellular stacked supercapacitor shown in Figure 3-8 needs to be developed. This research designs a novel multi-cellular planar supercapacitor architecture, in which multiple single-cell planar supercapacitors are integrated into a high-energy planar supercapacitor. The schematic of the new design with three cells is shown in Figure 3-9. The proposed multi-cellular planar supercapacitor has CNT thin film electrodes and solid-state PVA-based electrolyte. Similar to RGO thin films, CNT thin films also have high in-plane conductivity, because CNT bundles form dense network on the electrode plane.[15,69,70] More importantly, as discussed in Chapter 1, CNTs can be uniformly dispersed into water and the resulting CNT solution enables the

fabrication of CNT thin films by wet coating processes. Fabrication using wet coating processes has the flexibility to be highly scaled down for microelectronics applications and highly scaled up for automotive power electronics application.

In order to pattern positive and negative CNT electrodes on the same plane, wax printing/painting is used to create nonconductive gaps between electrodes. The CNT solution can only be deposited on to areas without wax, because areas with wax on them are hydrophobic and repel the CNT solution. Using high resolution wax printing, small and intricate electrodes can be patterned for micrometer scale supercapacitors; effective hydrophobic wax gaps created by wax printing between adjacent electrodes can be as small as 300μm.[71] On the other hand, wax painting also provides a fast and economical method to pattern electrodes for large-size planar supercapacitors with dimensions in meters. After CNT electrodes are fabricated, a thin layer of PVA-based electrolyte will be deposited on top of the electrodes by brush painting.

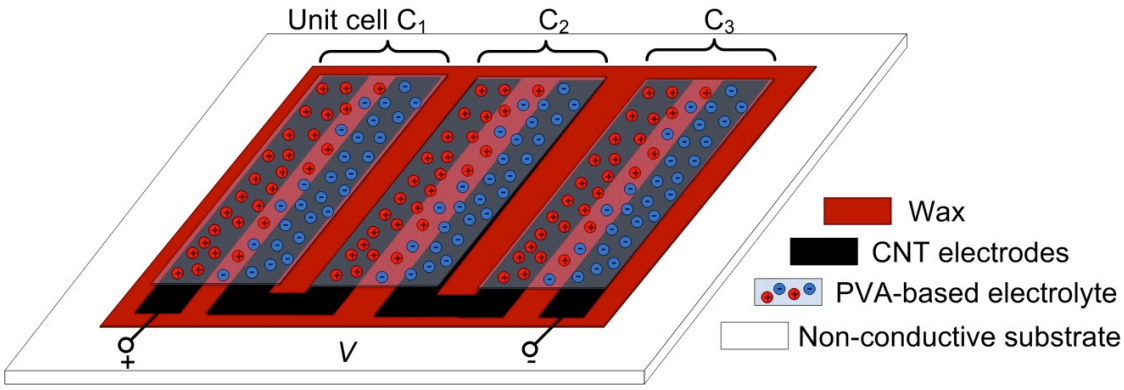

Figure 3-9 Schematic of planar supercapacitor with three cells.

The 2D planar configuration offers obvious advantages over the 3D stacked configuration. As the number of cells increases, the stacked supercapacitor will get bulkier, whereas the planar supercapacitor can still maintain its thin profile. Moreover,

the stacked architecture poses strict limits on what kinds of materials can be used as their bipolar electrodes. Essentially the bipolar electrode has to act as a barrier to prevent electrolyte transfer between adjacent cells. As a result, any materials, which are permeable to the electrolyte, cannot be used as bipolar electrodes. Porous materials with high surface area are ideal electrode materials, but they are also highly permeable to electrolyte and cannot be used as bipolar electrodes for stacked supercapacitors.

It would be difficult, if not impossible, to create an electrolyte barrier throughout the entire thickness of a porous electrode, as is required in the stacked supercapacitor case, but it is much easier to create lateral electrolyte barriers in the same plane as the electrodes. Researchers have previously used wax to create hydrophobic barriers on photocopy paper for use as fluid channel walls in paper-based micro-fluidic devices.[72] Similarly, the wax patterns used to define electrode areas in the proposed planar supercapacitor can also function as barriers to confine the hydrophilic PVA-based electrolyte within defined areas on the electrode plane. These "wax walls" make it possible to fabricate a high-energy multiple-cell supercapacitor onto different surfaces made of both porous as well as non-porous materials.

3.10 Fabrication Process of Second Generation Supercapacitor

The whole planar device can be fabricated using layer-by-layer coating onto a variety of substrates. Here, photocopy paper is used as an example substrate. Figure 3-10 schematically shows the fabrication process for the planar bipolar supercapacitor.

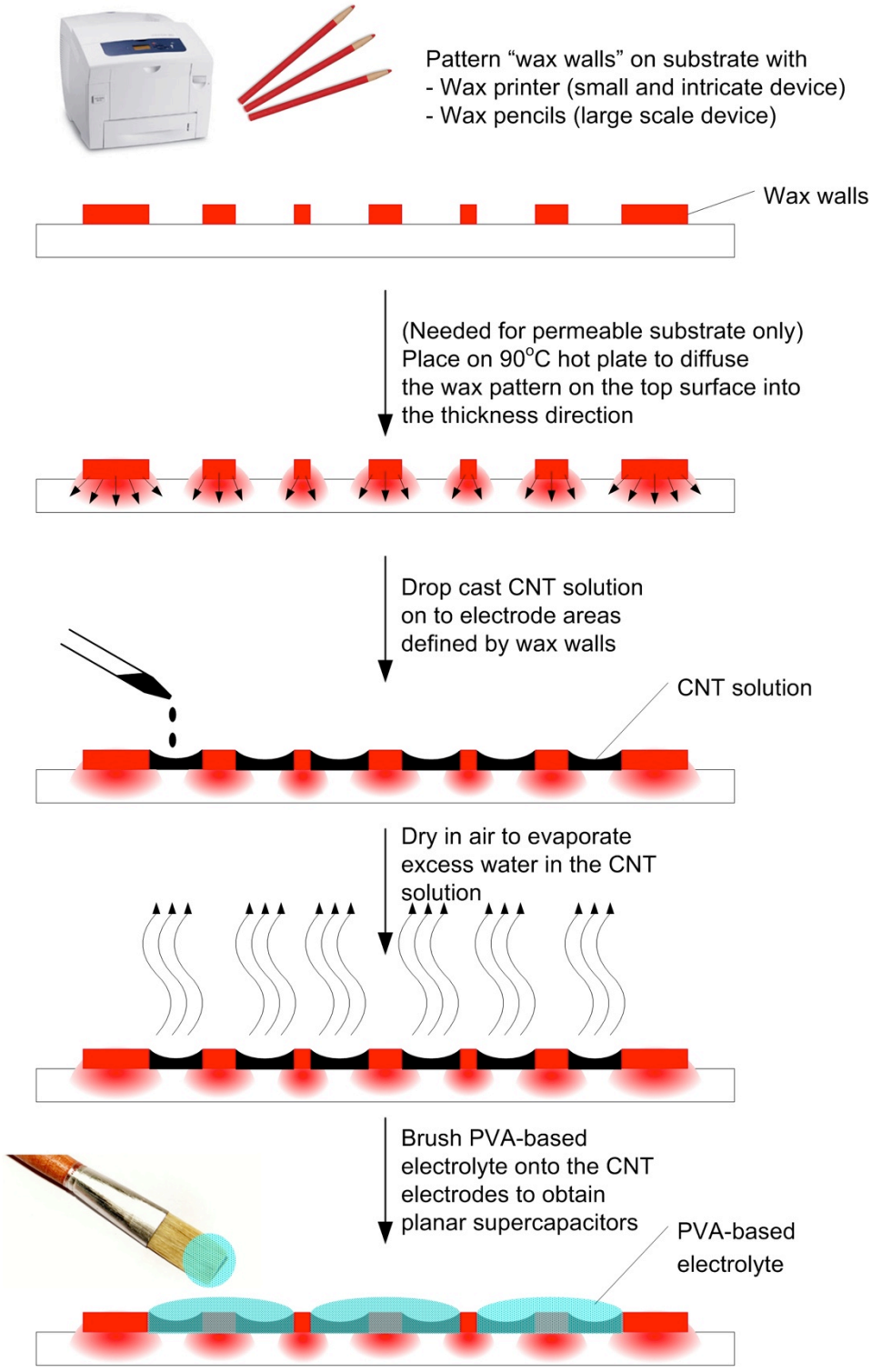

Figure 3-10 Schematic of fabrication steps in building the planar supercapacitor

Wax pencils were first used to paint the required wax patterns on the paper substrate. The paper area with wax patterned on it became hydrophobic (water repelling) and the untouched paper area remains hydrophilic (water absorbing). The wax pattern also facilitates the patterning of CNT electrodes later. For small and intricate supercapacitors in microelectronic applications, a wax printer can be used to generate high-resolution wax patterns on the substrate. The wax-patterned paper was then put on a 90^{o}C hot plate for 2 minutes to diffuse the wax and create electrolyte barriers throughout the thickness of the paper substrate. To fabricate CNT electrodes, acid functionalized CNT was dispersed into water and the resulting solution was dropped onto the hydrophilic area of the paper substrate and dried in the air. The drop-and-dry process was repeated several times until the desired resistance level was achieved. The sheet resistance of the CNT electrodes achieved is 12Ω/□ and this value can be further reduced if needed by more cycles of the drop-and-dry process. This low resistance makes it possible to use the high surface area CNT electrodes as both an active material and a current collector. The photocopy paper is an example of a porous and water absorbing substrate. The same planar bipolar supercapacitor structure can also be fabricated on non-porous and non water-absorbing substrates, such as Polyethylene terephthalate (PET) films. The fabrication process for non-porous substrates is almost the same as for photocopy paper substrate, except that the wax pattern does not need to diffuse into the thickness direction of the substrate, because the substrate itself is not permeable to CNT solution or electrolyte. Two kinds of solid-state PVA-based electrolyte, PVA/Phosphoric acid (H_3PO_4) and PVA/Lithium chloride (LiCl), have been prepared for the

supercapacitors. 6g of PVA powder (Mowiol® 18-88, Sigma Aldrich) and 1.6g of phosphoric acid (69 wt. %) or 12g of Lithium chloride powder (>99.0%, Sigma Aldrich) were added to 40 ml of DI water and stirred on a 85°C hot plate until the mixture became a clear and glue-like gel.[65] The gel-like electrolyte was then brushed onto the top of the CNT electrodes. Care should be taken during this process to ensure that the electrolyte of one cell is physically isolated from that of the adjacent cells, which is the key for successfully fabricating the multi-cellular supercapacitor.

3.11 Performance of Second Generation Supercapacitors

Planar supercapacitors with three unit cells were fabricated on paper and PET substrates using PVA/LiCl and PVA/H_3PO_4 electrolyte. Two planar supercapacitors with identical CNT electrodes but different electrolytes: PVA/LiCl and PVA/H_3PO_4 electrolyte were fabricated. It is observed that if not sealed airtight after fabrication the supercapacitor with PVA/LiCl can still maintain its original mechanical and electrical properties, which agrees with findings from other research.[73] However, it is found in this research that, as the water in the PVA/H_3PO_4 electrolyte evaporated, the originally flexible gel-like electrolyte will gradually lose its flexibility. The PVA/H_3PO_4 supercapacitor's resistive property became more dominant over capacitive property as the water content in the electrolyte is reduced. Figure 3-11 shows the CC tests on different days after a PVA/H_3PO_4 supercapacitor was fabricated and left unsealed. The IR drop became larger from day 1 to day 5, indicating the increase of the ESR value. After the electrolyte was re-wetted on day 6, the IR drop reduced, indicating a smaller ESR value than that of day 5. It is proposed that as the water evaporates, more and more H_3PO_4

crystallizes and the H^+ and $PO4^-$ ions lose their mobility in the PVA matrix. By re-wetting the PVA/ H_3PO_4 electrolyte and making the ions free to move again, the supercapacitor's resistive property is suppressed and the capacitive property becomes dominant again. It should be noted that the PVA/LiCl electrolyte does not have this problem of water evaporation and retains its capacitance value even after many days of exposure to the atmosphere. Hence, only performances of supercapacitors with PVA/LiCl will be discussed hereafter.

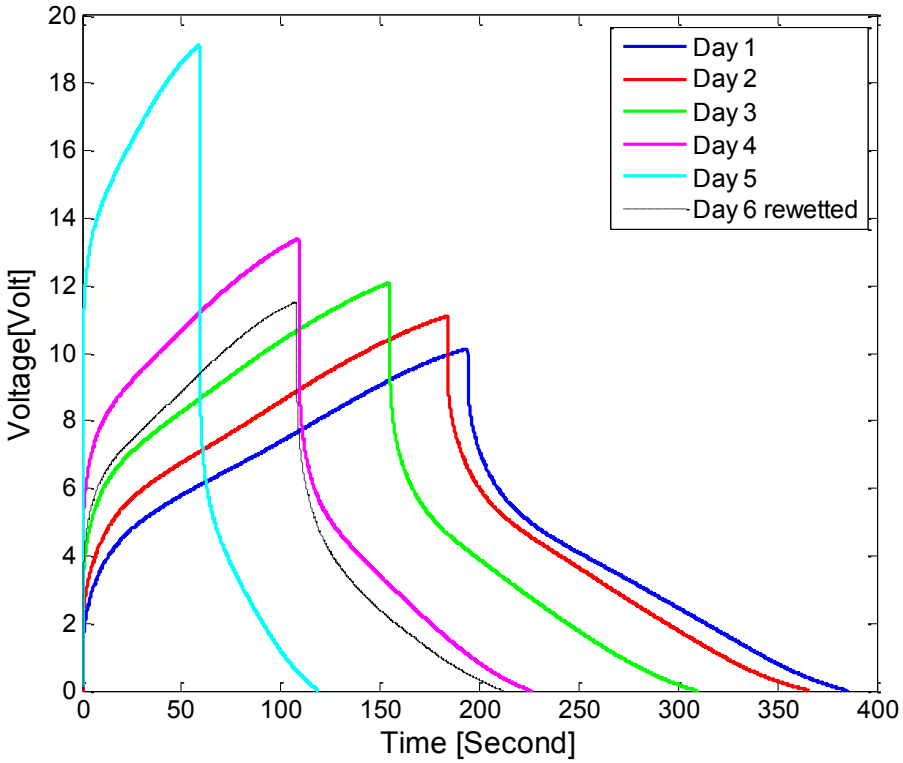

Figure 3-11 CC test results obtained day 1 to day 6 after the planar supercapacitor with PVA/H_3PO_4 electrolyte was fabricated.

Figure 3-12(a) is a photograph of the as-fabricated three-unit supercapacitor on paper placed next to a metric ruler. The effective size of the supercapacitor is 2.00cm×2.60cm, which covers the electrodes and the gaps between them. With the planar

configuration, additional cells can be easily added to achieve higher voltage and higher energy. As the number of cells increases, the area occupied by the planar bipolar supercapacitor also increases. The traditional stacked supercapacitor has the same issue: as the number of cells increases, the device gets bulkier. This could be problematic for applications with limited space for energy storage. Fortunately, the multi-cellular planar supercapacitor developed in this research has the benefits of being thin and flexible. Thus, it can be rolled up to reduce the area it takes up. Figure 3-12(b) shows how the three-cell supercapacitor in Figure 3-12(a) can be rolled up while lighting up a red LED.

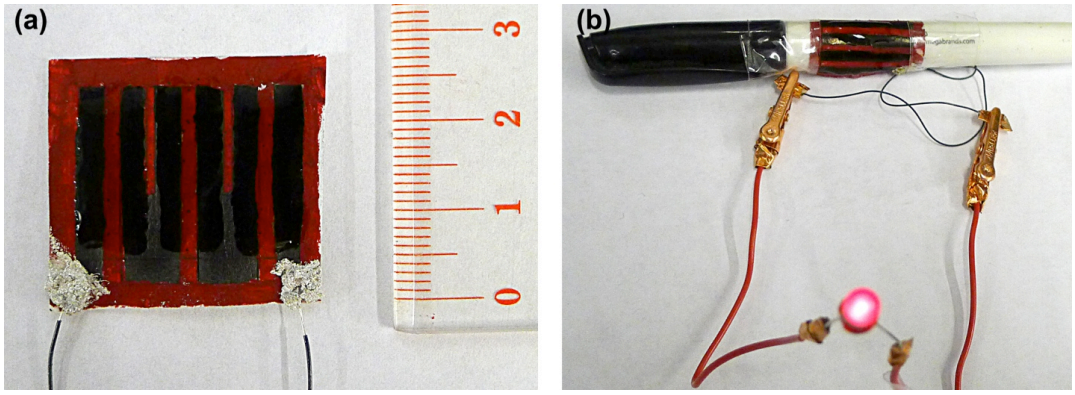

Figure 3-12 Optical pictures of the as-fabricated three-cell planar supercapacitor. (a) The flexible planar bipolar supercapacitor fabricated on paper substrate placed next to a metric ruler; (b) The supercapacitor in (a) can be rolled up while powering a red LED.

The three-cell supercapacitors fabricated on paper and PET substrates were tested with cyclic voltammetry (CV) at different scanning rates (Figure 3-13 (a) and (b)). The symmetric and near-square shapes of the CV curves demonstrate pure electrostatic capacitor behavior. The specific capacitances at different scanning rates (0.5mV/s to 100mV/s) are calculated and compared in Figure 3-13 (c). The specific capacitance of the CNT/PET planar supercapacitor is at the same level as that of the best graphene/PET

planar supercapacitors found in literature.[63] The specific capacitance of CNT/paper planar supercapacitor is much higher than that of the CNT/PET planar supercapacitor, especially at high scanning rates. Similar results have been found in literature for non-planar supercapacitors using CNT/paper electrodes and CNT/PET electrodes.[74] This can be explained by the differences in the surface morphology of the paper and PET substrates. Figure 3-14 (a) and (b) are the Scanning Electron Microscopy of the CNT-coated paper and PET electrodes under the same magnification. The paper based electrodes shows a rough and porous structure made of 3D cellulose network, whereas the PET based electrodes is flat and featureless. When coating CNT on non-porous substrates such as PET, dense CNT network forms on the PET surface. Hence, it is difficult for electrolyte ions to diffuse into the thickness direction of the CNT layer, especially at high scanning rate. On the other hand, the conformal coating of CNT onto the porous paper fibers can expose more CNT surface area to the ions in electrolyte, resulting in larger capacitance. Generally, the capacitance decreases as the scanning rate increases. Part of the CNT network's surface becomes inaccessible to ions in the electrolyte because the time allowed for ions to be inserted and extracted from the CNT network became shorter as the scanning rate increases. As the scanning rate increases to a high value, electric double layers of ions only form at the superficial layer of the CNT electrodes. Thus, the specific capacitance will converge to a constant value determined by the electrode area defined by the wax patterns. This result agrees with that of other non-planar supercapacitors using CNT as electrode materials.[75,76]

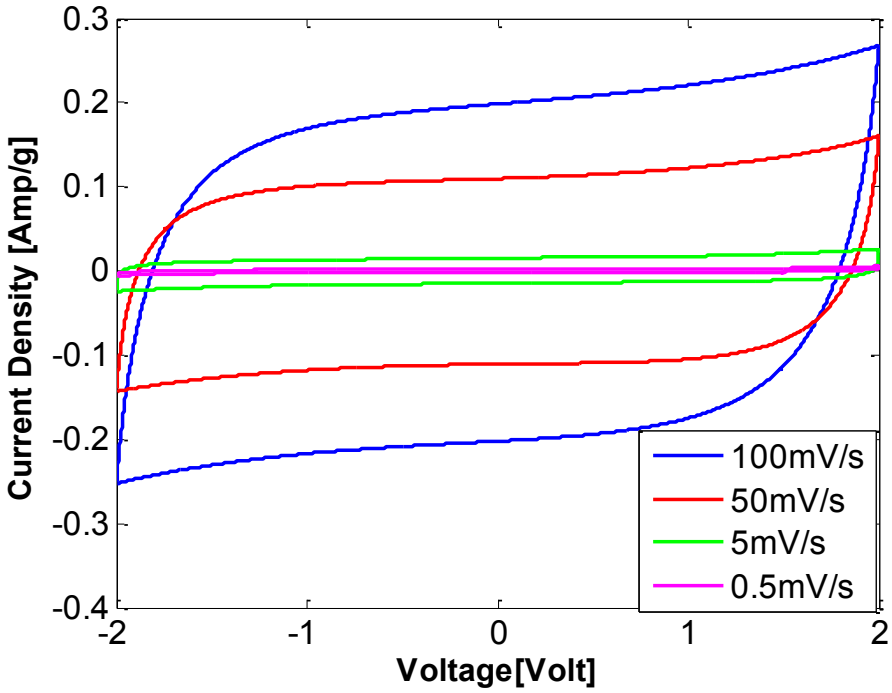
0.3
0.2
0.1
0
-0.1
-0.2
-0.3
-0.4
-2
-1
0
1
2
Current Density [Amp/g]
Voltage[Volt]
100mV/s
50mV/s
5mV/s
0.5mV/s

(a)

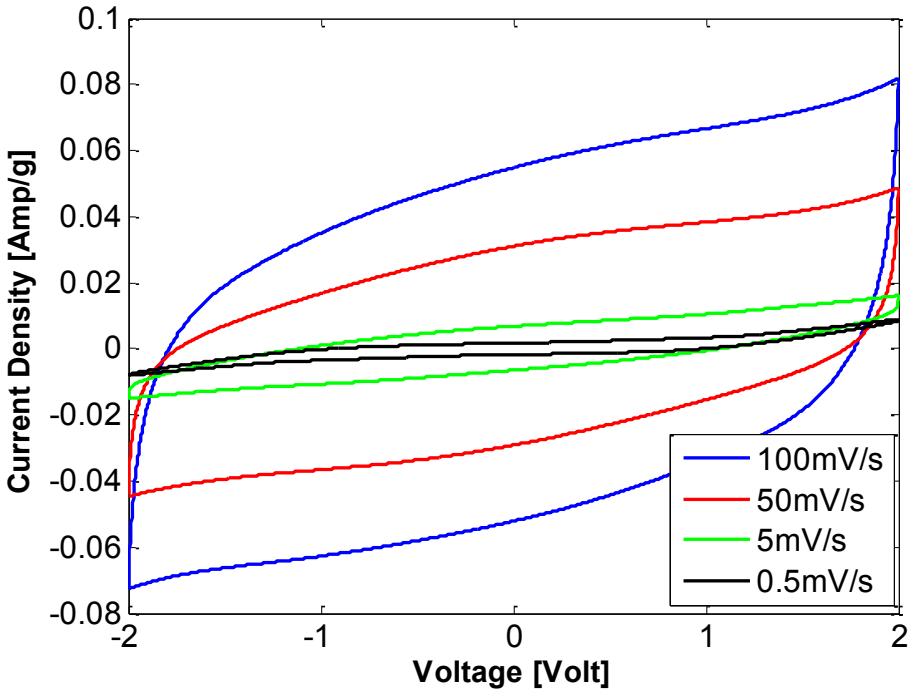
0.1
0.08
0.06
0.04
0.02
0
-0.02
-0.04
-0.06
-0.08
-2
-1
0
1
2
Current Density [Amp/g]
Voltage [Volt]
100mV/s
50mV/s
5mV/s
0.5mV/s

(b)

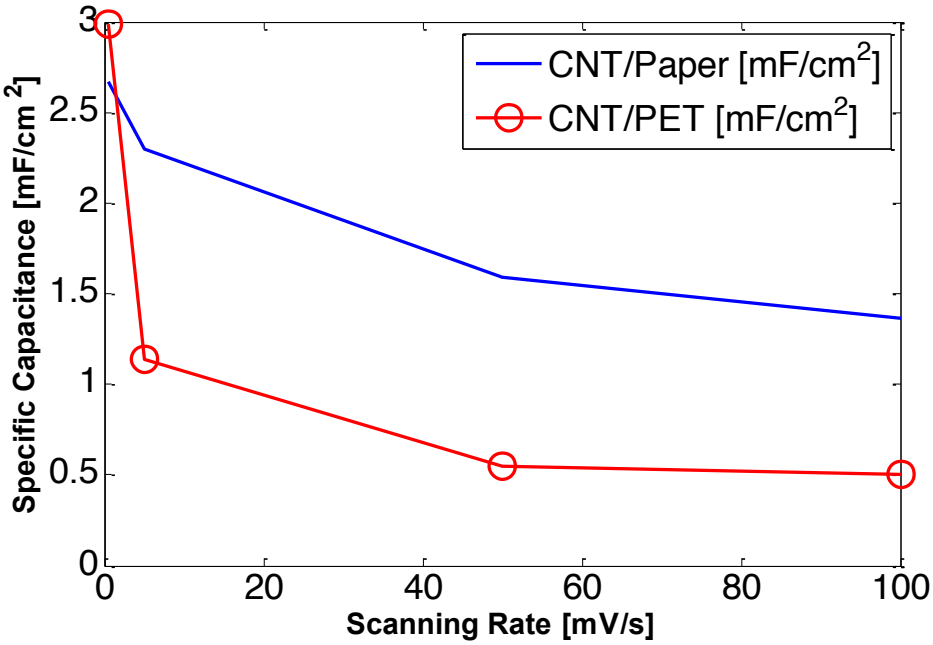

(c)

Figure 3-13 Cyclic Voltammetry at different scanning rates with three-cell planar bipolar supercapacitor using paper substrate and PET substrate; (a) and (b) are the CV curves of supercapacitor fabricated on paper and PET substrates respectively; (c) comparison of specific capacitance (F/cm^2) at different scanning rate for the two supercapacitors.

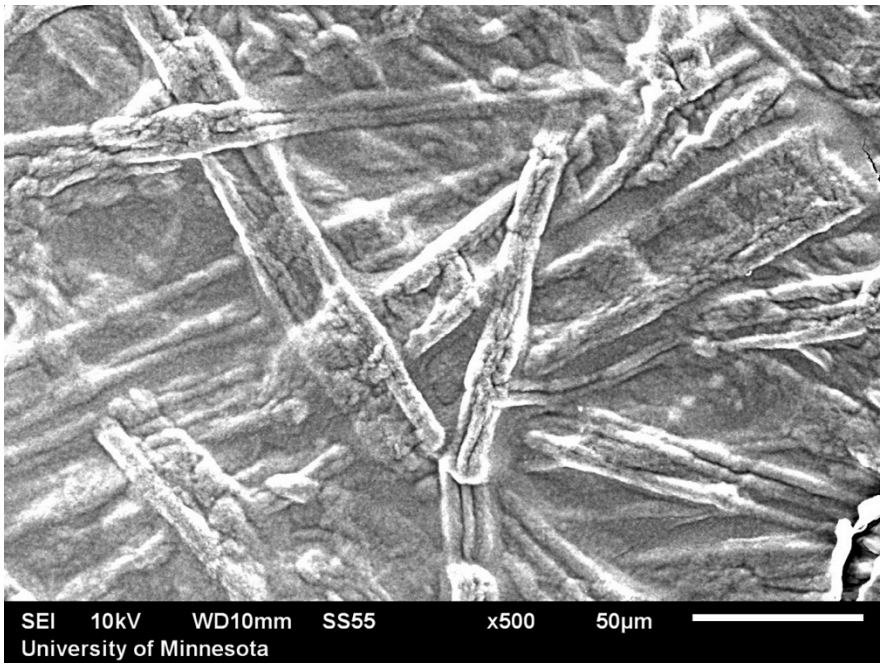

(a)

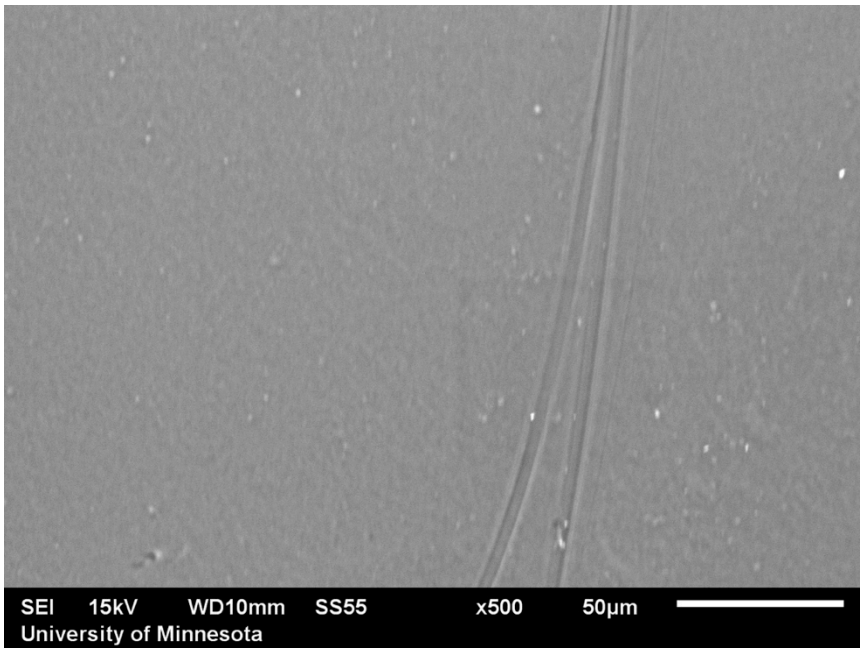

(b)

Figure 3-14 SEM images of CNT-coated paper and PET electrodes; (a) paper-based electrode; (b) PET-based electrode.

The capacitance retention abilities of both capacitors were tested by 1000 charging/discharging cycles as shown in Figure 3-15. It can be seen that supercapacitor made on the paper substrate has a better capacitance retention ability than the one made on PET substrate. The better retention ability of paper-based device could be attributed to the hydrogen bonding between the paper cellulose and the carboxylic groups on the acid functionalized CNT, which is missing in the PET-based device. During charging and discharging, electrolyte ions are inserted and extracted from the CNT network, causing volume expansion and contraction. The change of volume can result in CNT delamination from the electrode. After many cycles of charging, the originally clear electrolyte becomes darkened due to the release of CNT into the electrolyte. The hydrogen bonds can reinforce the CNT bonding to the paper substrate and reduce the delamination of CNT and increase the supercapacitors capacitance retention ability.

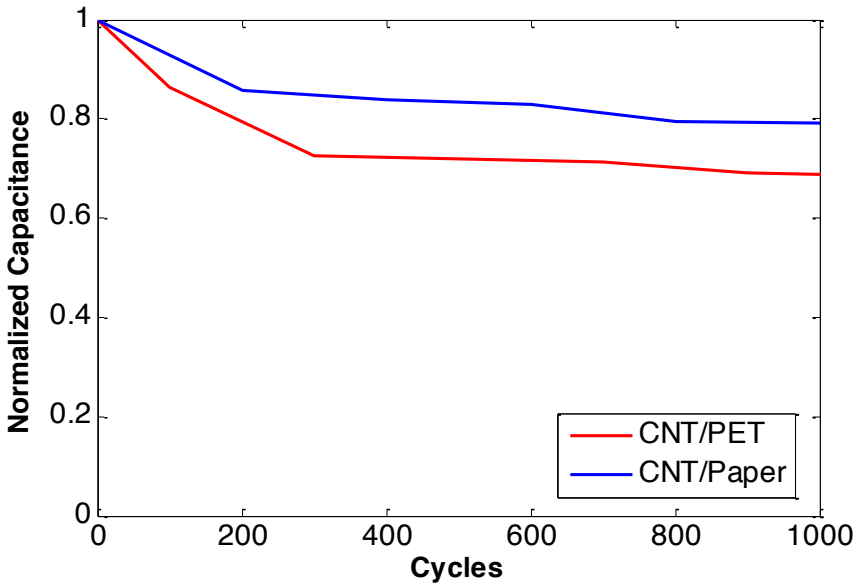

Figure 3-15 Comparison of capacitance retention ability with 1000 cycles of charging/discharging

Constant current charging-discharging (CC) was used to determine the maximum working voltage of the planar multi-cellular supercapacitors. The working voltages of a three-cell supercapacitor and the voltage across each of its individual cell were measured at the same time when the supercapacitor was charged by a constant current of 0.2mA. As shown in Figure 3-16 (a), the three-cell supercapacitor can reach a working voltage of $V_3 = \pm 6.3V$ with the voltage of each individual cell approximately equal to $V_o = \pm 2.1V$. The relationship $V_3 = 3V_o$ agrees with the voltage relationship for capacitors connected in series, showing proof that the three cells fabricated with the planar configuration were successfully connected internally to form a multi-cellular supercapacitor with a working voltage three times higher than that of one cell. Each cell having approximately the same voltage proves that the wax-patterned electrodes are identical to each other. Having

identical unit cells is very important to make the best use of every cell connected in series. High voltage operation of the supercapacitor is important for real-life applications.

Next it is demonstrated that a working voltage as high as 12V, which is the required voltage for automotive applications, has been achieved by a six-cell planar supercapacitor in this research. Figure 3-16 (b) shows the CC curve of the 6-cell supercapacitor being charged to above $V_6 = \pm 12V$ by a constant current of 0.2mA. Figure 3-16 (c) shows the CV curves of the three-cell and six-cell supercapacitors with scanning rate of 50mV/s. The capacitances calculated from the CV curves are C_3=2.87mF for the three-cell and C_6=1.13mF for the six-cell. $C_3 \approx 2C_6$ and $V_3 \approx 0.5V_6$ prove that the six-cell device is equivalent to connecting two three-cell devices in series.

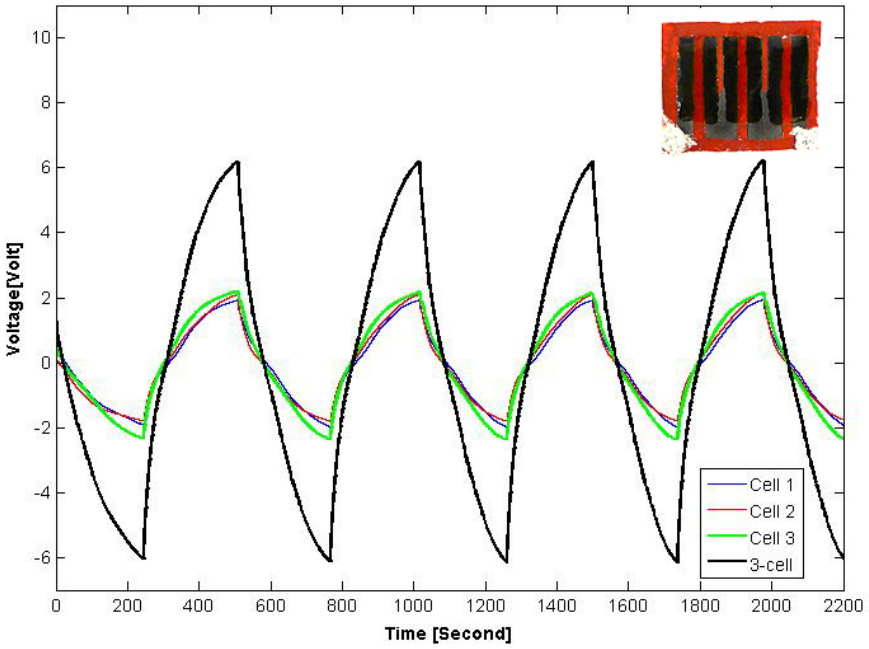

(a)

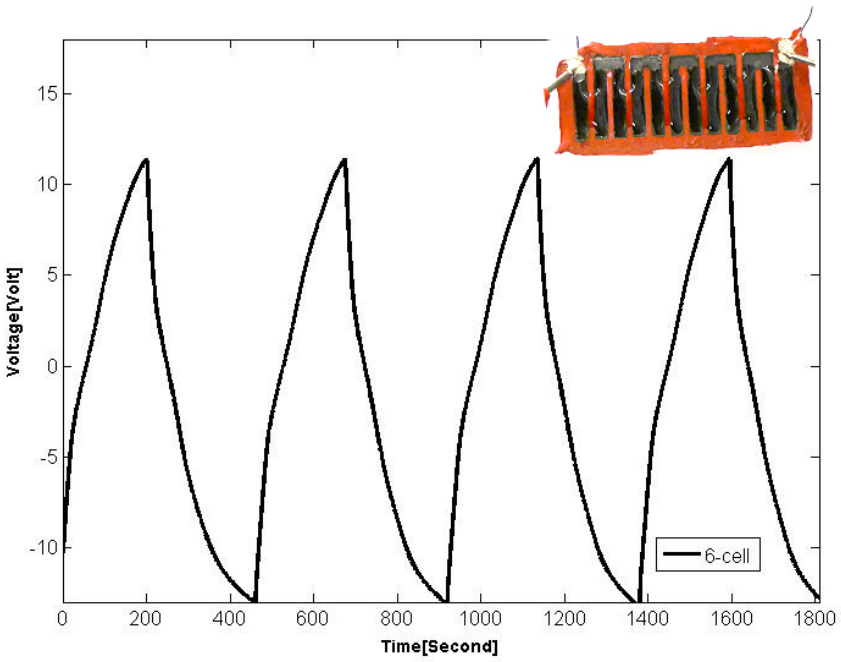

(b)

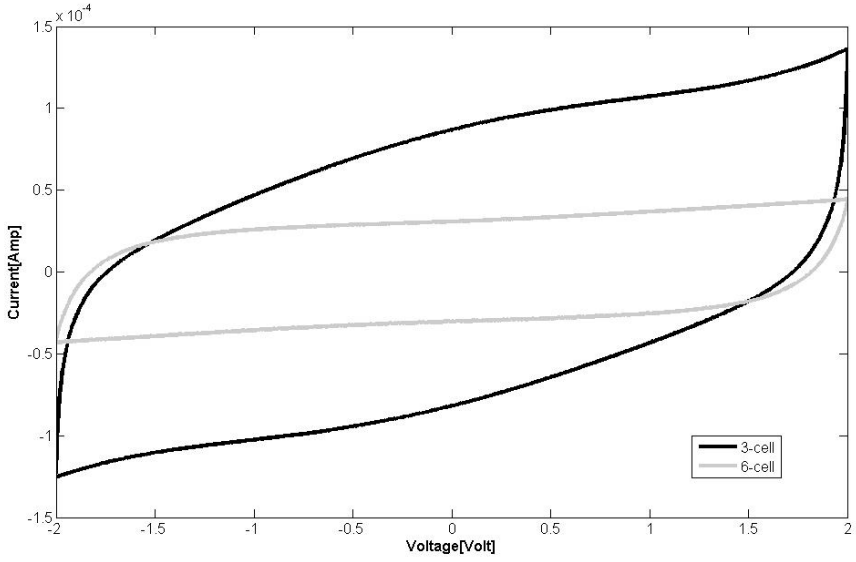

(c)

Figure 3-16 Performance measurement of the as-fabricated three-cell and six-cell supercapacitors. (a) CC curve (0.2mA) of a three-cell bipolar supercapacitor being charged to ±6V with almost identical voltage (±2V) across each cell; (b) CC curve (0.2mA) of a six-cell bipolar supercapacitor being charged to ±12V, high enough for HEV applications; (c) CV curves of the three-cell and six-cell at a scanning rate of 50mV/s.

Table 3-2 compares the metrics of the 3-cell supercapacitor developed in this paper with that of other planar supercapacitors in the literature. The specific capacitance of the CNT/paper three-cell supercapacitor is comparable to that of the best one-cell supercapacitors in literature. At the same time, the operating voltage obtained is ten times higher than previously reported. This leads to an energy density that is nearly two orders of magnitude larger than that of the best planar supercapacitors reported in literature, because the energy density of a supercapacitor is proportional to the square of its voltage.

Table 3-2 Comparison of supercapacitors metrics with other planar supercapacitors

Planar Electrode	**VS_2 Nanosheets**	**RGO/glass**	**RGO/PET**	**CNT/Si**	**CNT/paper 3-cell (this work)**	**CNT/PET 3-cell (this work)**
Electrolyte	PVA /$BMIMBF_4$	PVA/H_3PO_4	PVA/H_2SO_4	$BMIMBF_4$ (liquid)	PVA/LiCl	PVA/LiCl
Geometric area (cm^2)	11.52	0.18	40.28	0.27	5.20	5.20
Voltage(Volt)	0.6	1.0	1.0	0.5	6.0	6.0
Areal Spec. Cap. (mF/cm^2)	4.76	0.39	2.32	0.43	2.30	1.13
Areal Spec. Energy ($\mu Wh/cm^2$)	0.24	0.05	0.32	0.01	11.50	5.65

The performances of the three-cell planar supercapacitor are also compared with commercial supercapacitors with similar working voltages (6.0±0.5V) in Table 3-3. All the commercial supercapacitors have the disadvantage of being rigid and using a liquid electrolyte. The capacitances of the 3-cell supercapacitors are calculated from their CV curves at scanning rate of 5mV/s. When calculating the gravimetric specific capacitance and energy density for 3-cell planar supercapacitors, only the weight of the active materials (i.e. carbon nanotubes and electrolyte) is considered and the weight of the substrate (i.e. paper or PET) is not considered. This is due to the fact that the planar

supercapacitors can be fabricated onto existing structure and eliminates the use of substrate. As seen in Table 1, the 3-cell CNT/paper supercapacitor has a gravimetric energy density larger than the best commercial supercapacitor (KEMET FG0H475ZF).

When calculating the volumetric energy density, the volume of the whole device (i.e. electrode, electrolyte, and substrate) is considered. This is because the volume of the electrode and electrolyte is difficult to measure, especially in the case of CNT/paper planar device where the CNT electrode and electrode are infiltrated into the porous paper substrate. The volumetric energy density of the multi-cell planar supercapacitors is superior to that of all the supercapacitors.

Table 3-3 Comparison of supercapacitor metrics with commercial supercapacitors

	Commercial Supercapacitors			This work	
	KEMET FG0H475ZF	AVX BestCap BZ125A105ZAB	Panasonic RF Series	CNT/Paper Planar 3-cell	CNT/PET Planar 3-cell
Mass[1] (g)	27.3	18.4	3.3	0.0487	0.0492
Volume[2] (cm^3)	$\pi \times 1.43 \times 1.43 \times 2.2$	$4.8 \times 3.0 \times 0.67$	$\pi \times 0.68 \times 0.68 \times 0.95$	$2.0 \times 2.6 \times 0.0129$	$2.0 \times 2.6 \times 0.0127$
Capacitance (F)	4.7	1.0	0.1	0.012	0.0059
Voltage (Volt)	5.5	5.5	5.5	6.0	6.0
Spec. Cap. (F/g)	0.1722	0.0543	0.0303	0.2464	0.1199
Gravimetric Energy Density (mWh/g)	0.7233	0.2283	0.1273	1.2320	0.5996
Volumetric Energy Density (mWh/cm^3)	1.3972	0.4355	0.3044	0.8945	0.4467

[1] Mass for commercial supercapacitors is the mass of the whole device; mass for CNT/Paper and CNT/PET is the weight of CNT electrodes and PVA-based electrolyte.
[2] Volumes for all the supercapacitors discussed in Table 2 are the volumes of the whole devices.

3.12 Broad Example Impact of Developed Multi-cellular Planar Supercapacitors

Low energy density is the primary disadvantage of supercapacitors compared with Lithium-ion batteries. The high-voltage multi-cell planar supercapacitor developed in this research has exceptionally high energy density, significantly better than that of other supercapacitors found in literature. Hence, it fills the gap between supercapacitors and batteries and provides a promising solution to the need for energy storage systems of both high energy and high power. The device architecture makes it possible to fabricate such energy storage devices onto versatile surfaces by method as simple as painting. This could benefit on-site energy storage for energy harvesting/generation devices. For example, by fabricating the proposed supercapacitor on the back of a rooftop solar cell, the solar-generated electrical energy can be stored right away rather than being transmitted to a remote energy storage device, which could bring much more energy loss due to transmission. The thin and flexible properties of the proposed supercapacitor can also benefit the emerging area of flexible electronics such as flexible displays and wearable sensors.

The whole planar device can be fabricated using layer-by-layer coating onto any surface of arbitrary three-dimensional shape. For example, the supercapacitor can be fabricated on top of the sheet metal body of a car after use of a base insulating layer. No storage space for the capacitor in the trunk or other portions of the car is needed. When fabricating the planar supercapacitor onto existing structural materials, the use of a supporting substrate for the supercapacitor can be entirely eliminated. The thin CNT

electrodes and solid-state electrolyte layer add almost no weight or volume to an existing structure, whereas the substrate usually constitutes a dominant part of the weight and volume of previous planar supercapacitors. Hence, eliminating the substrates can result in extremely high gravimetric and volumetric energy densities for the overall system.

The performance of the current multi-cell planar supercapacitor has room for improvement. The size of the gap between the positive and negative electrodes can be minimized, so that the area occupied by the planar supercapacitor can be reduced and so that an even higher areal energy density can be achieved. To this end, wax patterns of higher resolution should be used. The shape of the CNT electrode is another place for optimization. Currently, the electrodes have a simple rectangle strip shape. Modifying it into interdigitated shapes has the potential to improve the power rate of the supercapacitor, because interdigitated electrodes provide shorter electrolyte ion transport path between the positive and negative electrodes.

To summarize, this research proposes a multi-cellular planar supercapacitor with CNT electrodes and solid-state polymer gel electrolyte. Such devices can be fabricated layer-by-layer using wax printing/painting and wet coating processes. The benefits of the proposed supercapacitor for real-world applications are as follows:

1) Minimal storage space: The supercapacitor can be painted right on top of any existing structural material due to its thin, flexible and solid-state architecture;
2) Reconfigurable and high energy stored: The working voltage and the energy stored in the proposed supercapacitor are both n times higher than that of a one-cell planar supercapacitor, and the value of n is reconfigurable;

3) Easy and economical fabrication and flexibility of scaling up or scaling down: The wet coating fabrication process has the flexibility to enable fabrication of small and intricate devices for microelectronic applications, as well as large scale devices for automotive residential and industrial energy harvesting applications.

3.13 Pseudocapacitor with Nickel/Nickel Oxide Core-shell Nanowires as Electrodes

Carbon nanotube-based supercapacitors are electric double layer supercapacitors (EDLS). As described in Section 3.1, in an EDLS charges are stored in the electric double layer mostly through electrostatic forces. There is another type of supercapacitor called "pseudocapacitor", in which charges are transferred into/from the electrode from/into the electrolyte through electrochemical reactions. Compared with EDLS, the advantage of pseudocapacitor is its exceptionally high specific capacitance, whereas disadvantages include relatively lower working voltage and reversibility.[77] Generally, pseudocapacitors behave more like batteries than capacitors – hence the use of "pseudo" in their name. Electrodes of pseudocapacitors are made of materials that can undergo reversible redox reactions with ions in the electrolyte. Transition metal oxides are important materials for pseudocapacitor electrodes. Ruthenium oxides have been widely studied as pseudocapacitor electrodes with specific capacitance as high as 734 F/g reported in literature.[78] Due to the high cost of ruthenium, researchers worked to find low-cost transition metal oxides as substitutes for ruthenium oxides. Electrodes made of cobalt oxide nanotubes with individual tube diameter of 200nm were found to have a specific capacitance of 574 F/g in 6M KOH solutions, and electrodes made of nickel oxide 50-80

nm nanoflakes could achieve 137.7 F/g in 2M KOH solutions.[79-80] It is noted that research using transition metal oxides as active materials for pseudocapacitors all reported that making the transition metal oxides into nanostructured materials can improve the resulting pseudocapacitors' performances.[81] The reasons include: firstly, nanomaterial-based electrodes provide larger contact area with electrolyte and shorter electron transport path, which all increase chemical reaction rate; secondly, the nanostructure brings large surface energy, which enables new reactions which are impossible with bulk materials with relatively lower surface energy; and finally, high porosity of nanomaterials can better accommodate the destructive stress/strain introduced by the volume change during chemical reaction and prolong device cycle life. In this research a novel nanostructured materials, the nickel/nickel oxide core-shell nanowire, will be developed and its performance in pseudocapacitor electrodes will be investigated.[82]

3.13.1 Fabrication of Nickel/Nickel Oxide Core-shell Nanowires

In this research, template-assisted method was used to synthesize nanostructured materials. Figure **3-17** is the schematic of the synthesis apparatus. Polycarbonate membrane filters with through-hole channels of 400 nm and 1200 nm (Isopore, Millipore) were used as templates. The membranes were first soaked in DI water and treated with ultrasonication for 5 minutes. This step ensured the inner walls of the channels were wetted, very important for the uniform growth of nickel nanowires across the whole template. Secondly, nickel nanowires were grown inside the template's nanochannels by an electrochemical process. A thin layer of copper was sputtered onto

one side of the membrane and served as the back electrode during the electrochemical synthesis. The copper-coated membrane was connected to the negative output of a DC power supply, whereas a nickel wire was connected to the positive output. A nickel electroplating solution was prepared using 150g/L nickel sulfate hexahydrate, 22.5g/L boric acid, and 22.5g/L nickel chloride hexahydrate. The membrane and the nickel wire were then dipped into the electroplating solution and a constant DC voltage of 2 Volt was applied between them. Nickel nanowires started to grow from the copper back electrode until the nanowires completely filled the nanochannels of the membrane after 8 minutes. The electroplating solution was kept at 60^{o}C. A sudden increase of the current implied that the nanochannels were completely filled by nickel nanowires and the growth of nickel progressed to the front surface of the membrane, which should be prevented. The membrane was removed from the solution, washed with DI water, and soaked in methylene chloride at 70^{o}C for 24 hours to remove the polycarbonate membrane and expose the nickel nanowires arrays. The nanowire arrays were then washed in chloroform and dried with nitrogen air. The as-grown nickel nanowires replicated the shapes of the nanochannels and have a uniform diameter of ~400nm (SEM image shown in Figure **3-18**). Finally, the nickel nanowires were treated in oxygen plasma (200 Watt, 100 sccm oxygen) for 20 minutes. The side of the membrane with copper coated was protected from the oxygen plasma with Kapton tapes. It is believed that the oxygen plasma treatment could further remove the residual polycarbonate on the nanowires and more importantly deposit a thin shell made of nickel oxide onto the nickel nanowire core. Hence, a core-shell structure was obtained. The nickel oxide shell served as the active

material for reversible redox reaction with KOH electrolyte as shown in Equation (3-11) and the nickel core serves as current collectors, which transport electrons to the nickel oxide during the redox reaction.

$$NiO+OH^- \leftrightarrow NiOOH+e^- \quad (3\text{-}11)$$

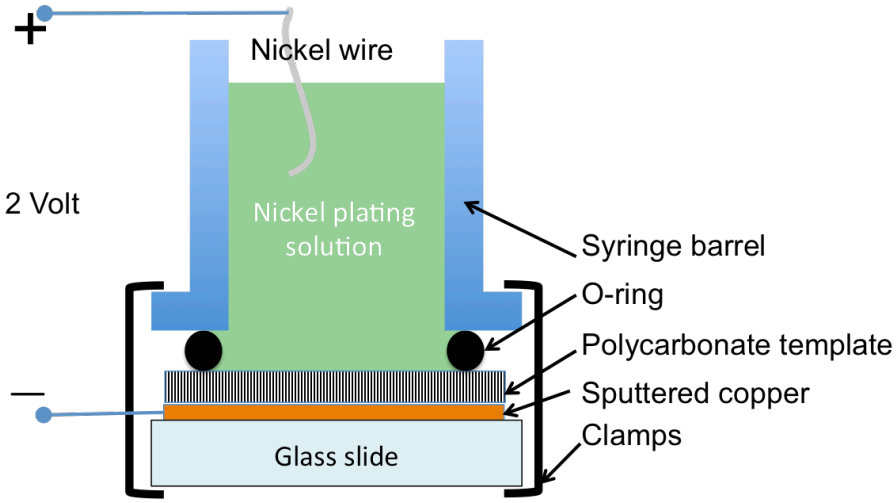

Figure 3-17 Schematic of nickel nanowire synthesis apparatus

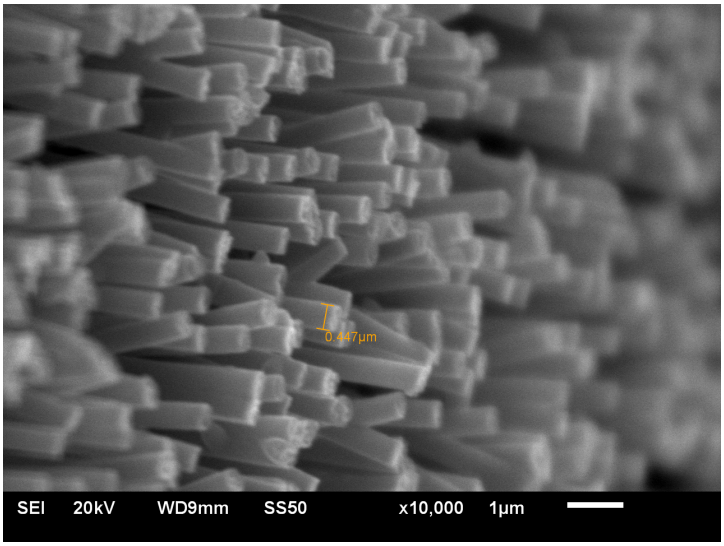

Figure 3-18 SEM image of nickel nanowires grown by polycarbonate membrane template with 400nm nanochannels.

3.13.2 Performance of the As-grown Nickel/Nickel Oxide Core-shell Nanowires as Pseudocapacitor Electrodes

The performance of the electrode made of the as-grown nickel/nickel oxide core-shell nanowires was tested in a half-cell with a three-electrode setup. The counter electrode was a platinum-coated titanium wire and the reference electrode was a standard Ag/AgCl electrode. The electrolyte was a 2M KOH aqueous solution. Figure **3-19** is the cyclic voltammetry (CV) obtained at different voltage ranges but the same scanning rate with nickel/nickel oxide electrode grown by a template with channel size of 1 μm. The obvious redox peaks in both CV curves were caused by the redox reaction shown in Equation (3-11), which further proves that the oxygen plasma did deposit a thin layer of nickel oxide onto the nickel nanowires. The specific capacitances calculated from the CV curves are 21.14 F/g for V_{max}=0.45 Volt and 15.02 F/g for V_{max}=0.35 Volt, when the weight of the whole electrode was considered. The areal specific capacitance are 0.090 F/cm^2 for V_{max}=0.45 Volt and 0.064 F/cm^2 for V_{max}=0.35 Volt. The cycling stability of the electrode was tested by 100 cycles of CV test (Figure **3-20**). The capacitance initially increased from its starting value then stabilized after 60 cycles.

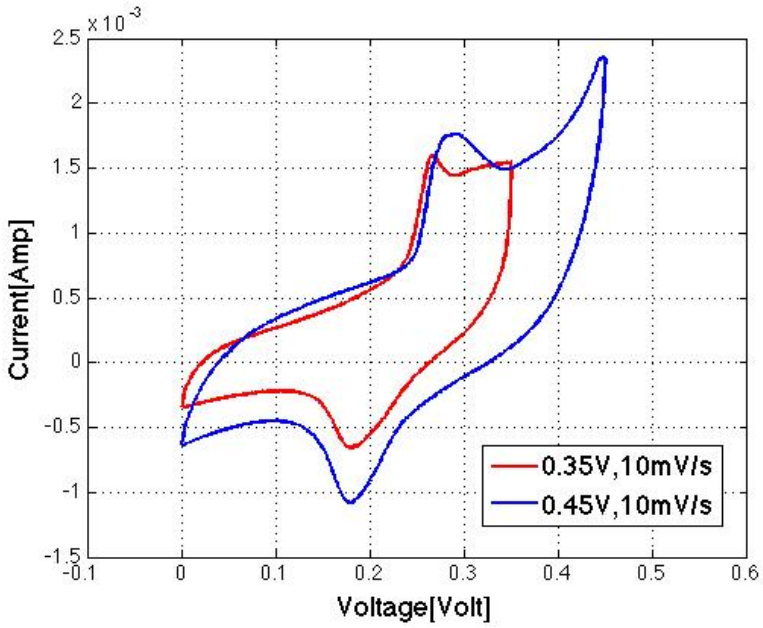

Figure 3-19 Cyclic voltammetry obtained at different voltage ranges but same scanning rate of 10mV/s with nickel/nickel oxide nanowires electrode grown by polycarbonate membrane with channel size of 1 μm.

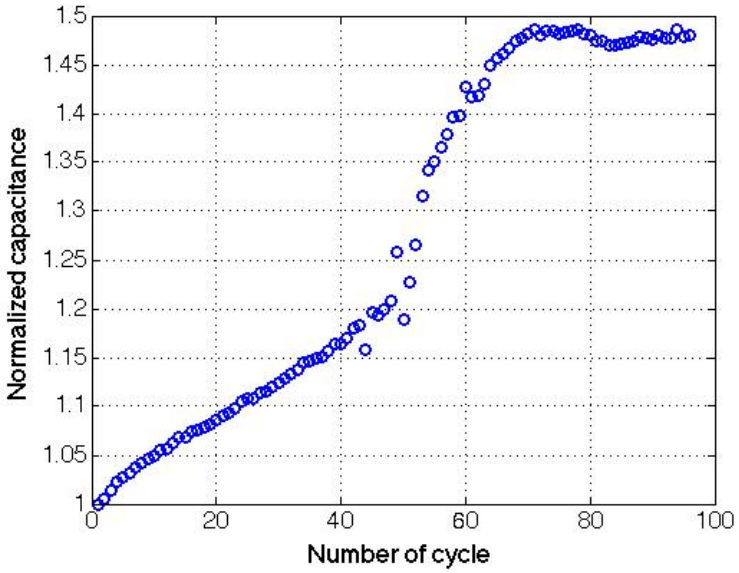

Figure 3-20 Cycling stability test of the nickel/nickel oxide core-shell nanowire based pseudocapacitor electrode

4 Renewable Energy Source for the ANC system

4.1 Benefits and Feasibility of Solar Power for the ANC System

Integrating solar cells in the window panes to provide sustainable energy for ANC brings several advantages to the current window ANC system. Using solar energy eliminates the use of electricity generated by fossil fuels. Without external wiring and power supplies, the self-powered ANC system will also be more compact. Installation and handling will become significantly easier as well. Windows could be easily replaced in homes with the new ANC windows without requiring a wiring system.

To validate the feasibility of solar-powering, the energy requirement of the ANC system needs to be analyzed first. Here, the noise distribution around the MSP airport is used as an example to calculate the energy requirement. As shown in Table **2-1**, all homes are under the impact of noise less than 70dB DNL. For a conservative calculation, 70dB DNL is used to calculate the acoustic energy density of the airport noise. By definition, 70dB means the power density of the noise is 10^{-5} Watt/m^2. Thus, the noise energy density is the power density times 24 hours, which is 2.40×10^{-4} Watt-hour/m^2. By the principle of active noise cancellation, anti-noise with equal energy density should be generated by the ANC system daily. The proposed ANC system uses a piezoelectric actuator (PVDF thin film), which converts the electrical energy into acoustic energy. The energy conversion efficiency (or electroacoustic efficiency) of the actuator is measured at different frequencies as shown in Figure **4-1**, and its average efficiency is 0.0097%. Such a speaker has to be driven by a power amplifier. In this research, ESA 2-channel car

audio amplifier with a rated power of 100 Watt was used. The amplifier requires adequate power to avoid overload during transient, but during normal operation the power level is only a few watts (in this case 6 Watts). The combined electroacoustic efficiency of the piezoelectric speaker and the amplifier was also measured at different frequencies as shown in Figure **4-1**, and the average combined efficiency calculated from this figure is 0.0012%. As a result, total electrical energy density required by the speaker and amplifier combined is 20 Watt-hour/m^2.

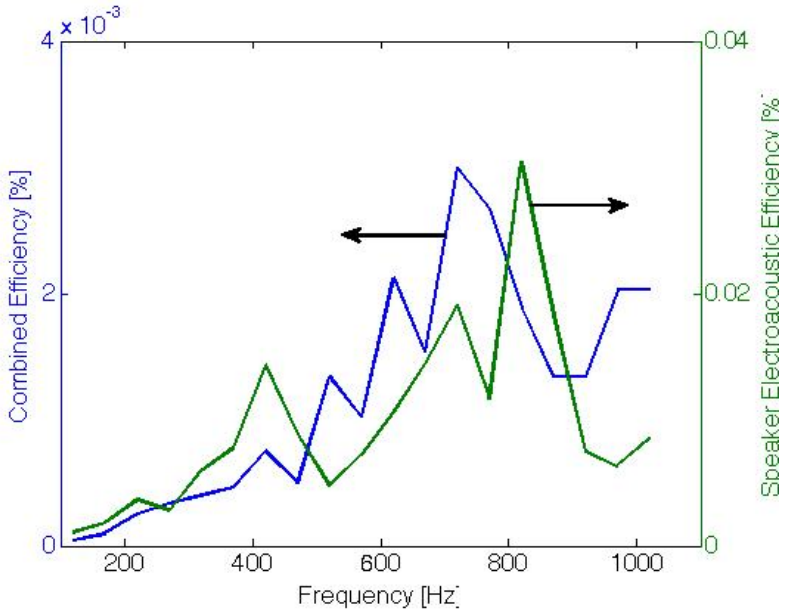

Figure 4-1 Combined efficiency of the transparent speaker system (including a piezoelectric speaker and a power amplifier), and the speaker's electroacoustic efficiency

Solar energy is the cleanest and most abundant renewable energy source available. According to surveys on solar radiation received on the earth by National Renewable Energy Lab, a vertical flat-plate facing north, which corresponds to solar cells mounted on north-facing home windows, receives an average solar radiation of 1.1 kWatt-hour/m^2 daily in the Minneapolis-St. Paul area.[83] In this case, 1.8% of the solar

radiation received on the window is needed daily to power the ANC system. It should be mentioned that vertical flat plates facing north represents the worst case, for which the solar radiation received is the least when compared with all other cases, such as horizontal plates or south-facing plates. Hence, the 1.8% solar energy conversion efficiency is a conservative estimation. Figure **4-2** shows the recorded efficiencies of solar cells available up to date. Considering that most commercial solar cells now have efficiencies well above 1% and the best ones from research labs have efficiencies higher than 40%, a solar-powered ANC system is totally feasible from the energy density point of view. An important design consideration of solar cells for home windows is that the cells have to be as transparent as possible, so that the function and aesthetics of the window can be preserved. Ongoing research effort is devoted to developing more transparent and efficient solar cells, which will be further reviewed in the next section.

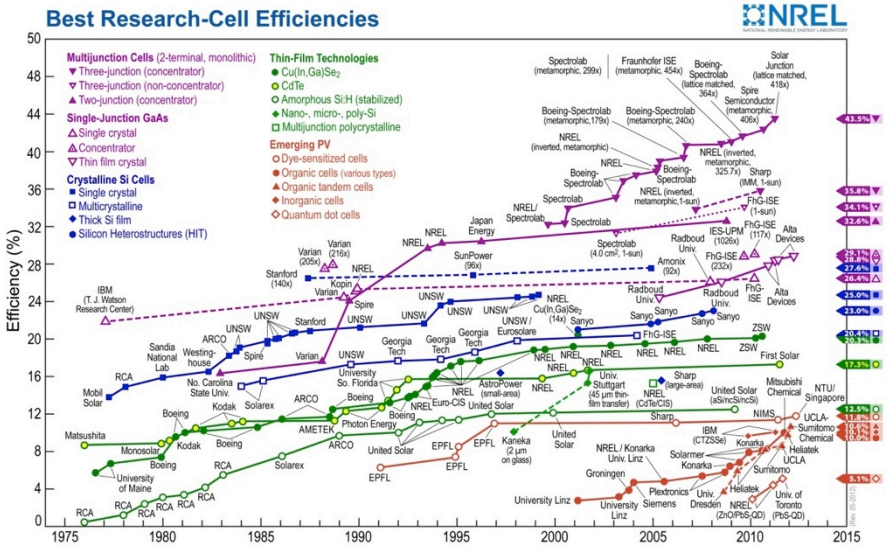

Figure 4-2 Up to date recorded PV cell efficiencies from National Renewable Energy Laboratory (NREL).[84]

4.2 Review of Photovoltaic Technologies

Since the invention of the first practical photovoltaic cell by Bell Laboratories in 1954, photovoltaic (PV) technologies have evolved through three generations. Most commercially available solar cells are based on the first generation (1G) technology. It uses a single PN-junction on single crystalline or polycrystalline silicon wafers. Power Conversion Efficiency (PCE) - the percentage of incoming solar radiation that is converted by the solar cell into usable power- is usually used to quantify the performance of PV cells. 1G solar cells have high PCE (recorded highest 27.6%)[84] and relatively long lifetime. However, crystalline silicon has low optical absorption coefficient. As a result, the wafers need to be 200 μm or thicker to absorb most of the incident light.[85] The required thick silicon layer limits the possibility of making transparent silicon solar cells for solar-powered ANC home windows.

The second generation (2G) solar cells are based on thin film technology. 2G solar cells use semiconductor materials with high optical absorption rate. Thus a thickness of only a few microns is needed to absorb the most incident light. The thin film fabrication processes (sputtering, evaporation, etc) increase the manufacturing scale from the 1G's 100 cm^2 on a silicon wafer to 1 m^2 on a glass sheet. The highest recorded PCE of 2G solar cells is 28.8%,[84] a little better than the best single-junction 1G products. With thinner layer of photovoltaic materials, researchers have found the possibility of increasing the solar cells' light transmittance without sacrificing much PCE. Takeoka et al. significantly improved the light transmittance of the translucent thin film solar cells using microfabrication techniques.[86] Their so-called see-through PV cells have the same

structure as ordinary thin film amorphous silicon solar cells: a glass substrate, a transparent top electrode, amorphous silicon layers, and a metal back electrode. The only difference is that they used photoresist to pattern uniform microscopic holes of size between 0.1 and 1.0 mm in the photovoltaic area. Portion of the incident light is directly transmitted through those microscopic holes. By changing the holes' size and density, light transmittance of the solar cell could be modified between 15% and 50%.

The third generation (3G) solar cells feature diverse photovoltaic materials and structure designs. Organic photovoltaic cells (OPVs) use photo-excitable polymers or small molecule weight organic materials as electron donors and acceptors. Using photo-excitable polymer blends, OPVs can be fabricated by low-cost printing and coating technologies. They have great potential in economical, large-scale, flexible, and light-weighted solar energy harvesters. Huang et al spin-coated a thin layer of poly(3-hexylthiophene):[6,6]-phenyl-C61-butyric acid methyl ester (P3HT:PCBM) polymer blend onto transparent conductive electrodes to build a semitransparent OPV. The as-fabricated OPV has a PCE of 3% and a transparency of 70% in wavelength range where P3HT:PCBM has no absorption (the average transparency in visible light wavelength range was not given).[87] OPVs using small molecule organic materials have good potentials in transparent solar cells. For such OPVs, the optimal thickenss of the active layer is on the order of a few tens of nanometers.[88,89] This results in a thinner device and thus a higher optical transmittance than polymer OPVs. Lunt et al evaporated small molecule chloroaluminum phthalocyanine (ClAlPc) and fullerene C_{60} onto transparent conductive indium tin oxide (ITO) electrodes as donor-acceptor pair. The as fabricated

OPVs have absorption peaks in the infrared light range (near 750nm). With a PCE of 1.7%, the OPVs have average visible light transmittance of 56%.[90] The performance of the small molecule weight OPVs are greatly influenced by impurities in the active layer, because the layer is very thin. Hence, the source materials have to be of high purity and the deposition of small molecule weight organics thin films requires high vaccumm (10^{-6}~10^{-7} Torr) or even ultrahigh vacuum (10^{-10} Torr) environment,[91,92] which makes it difficult and expensive for large-scale production.

Dye-sensitized solar cells (DSCs) are based on a new photovoltaic mechanism, which is a photo-electrochemical system consisting of low cost photo-excitable organic dyes and electrolyte.[93,94] DSCs are made with abundant and low purity materials with wet chemical fabrication processes. Economical and large scale methods such as roll-to-roll printing has been proposed for the manufacturing of DSCs.[95] The low material and manufacturing costs make up for its less impressive PCE (highest recorded 11.8%).[84] This research will focus on developing transparent DSCs with materials and fabrication methods that are economical and scalable.

4.3 Dye Sensitized Solar Cells

Dye-sensitized solar cells consist of a transparent conductive electrode (such as fluorine-doped tin oxide thin film on glass) as the working electrode, a layer of n-type semiconducting photoanode anchored with photo sensitizing dye, a hole-conducting electrolyte system, and a catalyst-coated counter electrode. When the dye absorbs photons, photoexcited electrons will be injected into the conduction band of the semiconducting photoanode, which then carries the electron to the working electrode.

The oxidized dye is reduced by obtaining electrons from the electrolyte, which transports the positive charges to the counter electrode through oxidzation of ions in the electrolyte. The electrons collected at the working electrode will pass through external circuit, do work, and finally reach the counter electrode. With the help of the catalyst, the electrons will neutralized the positive charges through reduction reaction with the electrolyte and complete the circuit. Continuous research effort have contributed to the optimazation of the materials of DSC components and the DSC efficiency has been greatly improved. Grätzel et al discovered that a film of titania (TiO_2) nanoparticles (10~20nm) can function as the n-type photoanode. Moreover, the mesoporous TiO2 provides large surface area to anchor the photosensitive dye and greatly improve the PCE.[96] Ruthenium (Ru) based dyes, such as N3, N719, and Z907, have been the first choice of dyes in most of the studies on DSCs.[97,98,99] They have fairly broad absorption spectra but low molar extinction coefficients, meaning low light absorptivity. Although great research efforts have been placed on developing alternative dyes for the purpose of removing expensive metal Ru from the DSC systems, Ru-based dyes are still benmarks for DSC research. The iodide/triiodide (I^-/I_3^-) system has been identified as the most successful electrolyte system for the DSCs.[100,101] It has slow recombination between the photo-excited electrons. Recombination of electrons with the electrolyte will reduce the electrons being transferred to the working electrode, resulting in lower photo current and lower PCE. It has small size, which could diffuse into the mesoporous TiO_2 fast. Each molecule of I^-/I_3^- can carry two electrons from the back electrode, contributing to higher photo current for a given concentration of electrolyte. As for the catalyst-coated counter

electrode, platinum has been proven as an effective catalyst for the reduction reaction of the electrolyte.[102,103] To fabricate Pt-coated electrode, Pt is usually sputtered onto a transparent conductiv electrode. For scalable solution-based fabrication, Chloroplatinic acid solution (H_2PtCl_6) is painted onto the electrode and thermally decomposed into platinum. In an effort to eliminate the use of expensive Pt, several Pt-free counter electrodes have been proposed in literature, including carbon, tungsten carbides, titanium nitride, etc.[104,105,106,107]

The transparency of the DSC is tunable. One simple and straightforward way is to change the thickness of the TiO_2 photoanode. With a thin photoanode, there are less dye absorption sites. Lower mass loading of the dye will result in lower light absorption and higher light transmission. However, this high transparency is only achievable at the expense of a low PCE. Strategies to improve the PCE of transparent DSCs are proposed in literature. First strategy is to deposit a back-scattering layer made of large TiO_2 particles (diameter of ~ 400nm) on top of the original photoanode made of small TiO2 particles (diameter of ~20nm) to increase the optical path length of low energy photons.[108,109] However, such a high scattering layer makes the DSCs opaque and hinder its use as a window integrated solar cell. Another method is to attach a Bragg Reflector to the counter electrode to selectively reflect light at certain wavelengths (usually outside or at the edge of the visible light wavelength) back to the dye layer for reabsorption.[110,111] Heiniger *et al.* fabricated a Bragg Reflector onto a DSC with dye layer of only 1 μm, and enhance the PCE by 39%. The resulting see-through DSC has a PCE of 3.37%.[112]

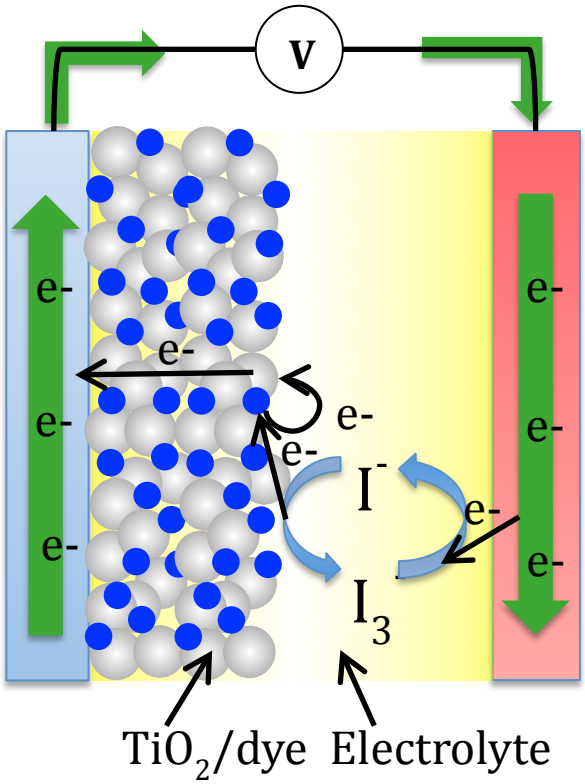

Figure 4-3 Schematic of dye sensitized solar cell device architecture

4.4 CNT Thin Films as Catalytic Counter Electrodes for DSCs

4.4.1 Overview

Platinum has great catalytic performance towards the reduction of I_3^- to I^-, but it is expensive and its performance degrades in the corrosive I^-/I_3^- electrolyte.[113] Extensive research efforts have been placed on the search for alternatives made of cheaper and abundant materials. Carbon materials have attracted a lot of attention because they are low-cost, corrosion resistant, and electrically conductive. Activated carbon,[102] carbon black,[114] and carbon nanotubes[115] all show catalytic activity in I^-/I_3^- electrolyte. Some study even reported that carbon electrode has nearly equivalent performance as the Pt electrode.[116] Among them, CNTs are very promising counter electrode materials. CNTs

have mesoporous structure, which is highly accessible to the ions in electrolyte. They are also more corrosion resistant than Pt, which provides better stability and longer life. Although the exact mechanism of I_3^- reduction at the counter electrode made of carbon nanomaterials remains unknown and is still under study, experimental studies have shown that high surface area, low resistivity, and oxygen-containing functional groups all help to increase the catalytic activity of the carbon nanomaterials.[103] This research uses polyelectrolyte and functionalized-CNT layer-by-layer (LBL) self-assembled thin films[40] as counter electrodes for DSC. The mass loading of CNT and transparency of CNT thin films can be tuned by varying the number of self-assembled layers. Its all-solution fabrication process is scalable and suitable for a wide variety of substrates including glass, polymer, etc. In addition, CNT thin films fabricated by the LBL self-assembled method have a smooth macrostructure while maintaining the micro/nano mesoporous structure.[117] Such a "macro-smooth" surface profile can prevent circuit short caused by electrical contact between the counter electrode and the TiO_2 photoanode introduced by protruding CNT chunks from the counter electrode.

4.4.2 Fabrication of CNT-based DSC

Fluorine-doped tin oxide (FTO) glass slides (6-8 ohm/square, MTI Corp) were cleaned by detergent solution (1wt % Alconox Powdered Precision Cleaner in deionized water) in ultrasonication bath for 15 minutes to remove any grease and particles on the glass. Then it is washed sequentially in deionized (DI) water, acetone, methanol, isopropyl alcohol, and dry in nitrogen airflow. The glass was further cleaned in oxygen plasma (200 sccm oxygen flow, 200 Watt Power) for 15 minutes to get rid of organic

contaminations. The cleaned glass was put into 40mM solution of Titanium tetrachloride in Methylene chloride at 70^{o}C for 30 minutes, washed by DI water, and dried in nitrogen airflow. TiO_2 paste (Ti-Nanoxide T/SP, Solaronix) was coated onto a 1 cm by 1 cm area on the FTO glass by doctor blade method. Increasing the number of coatings can increase the thickness of the TiO2 layer. The TiO_2-coated glass was put away into a clean box for 6 minutes to relax the stress in the TiO_2 thin film, and then placed on a 125^{o}C hot plate for 15 minutes to cure the TiO_2 paste. The originally translucent TiO_2 film became slightly yellow after curing. Heat treatment in a 500^{o}C oven for 30 minutes turned the yellow film into transparent photoanode. After being cooled down to 80^{o}C, the photoanode was immediately immersed in 0.3 mM Z907 (Sigma Aldrich) dye solution in acetonitrile and tert-butanol (1:1 v:v) at 80^{o}C for 12 hours. The thickness of the TiO_2 layer was studied by a profiler (P-7, Tencor) and found to be 4.61μm.

Two catalytic counter electrodes were fabricated for performance comparison. To make Pt-coated counter electrode, Chloroplatinic acid solution (Plantisol, Solaronix) was brush-painted onto a FTO glass pre-cleaned by the procedure previously described. The glass slide was placed in a 450^{o}C oven for at least 15 minutes. The oven's temperature ramping rate should not be too high to bring thermal shock to the glass slide. Otherwise, cracks will appear on the electrode, reducing its conductivity. To make CNT-coated counter electrode, a layer-by-layer self assembly method was used. Specifically, the FTO glass was first modified by a hydrophilic and positively-charged polyelectrolyte poly(diallyldimethylammmonium chloride) (PDDA). To ensure full coverage of PDDA on the glass slide, a negatively charged polyelectrolyte poly (sodium styrenesulfonate)

(PSS) was also introduced. The pre-cleaned FTO glass was first immesed into 1.5 wt% PDDA solution (with 0.5 M Sodium choloride NaCl solution) for 15 minutes at room temperature. After rinsing with DI water, it was then immersed into 0.3 wt% PSS solution (with 0.5 M NaCl solution) at the same temperature for the same amount of time. The previous PDDA/PSS coating was repeated once and finally the electrode was treated with PDDA again. This process ensures that the FTO glass is fully coated with PDDA. Hence the outermost surface is positively charged. Acid-functionalized MWNT solution was coated onto the PDDA-modified FTO glass by wire-wound rod coating and dried on a 80^{o}C hot plate. Note that the acid-functionalized MWNT is negatively charged when the carboxylic groups (-COOH) lose the proton in the solution. Hence, the MWNT can form electrostat bonding with the PDDA, resulting in a smooth and robust coating of MWNT on the FTO glass. The mass loading of the catalyst MWNT can be increased by coating additional layers onto the previous MWNT layers. The working electrode and counter electrode were assembled together using a 25μm thermoplastic spacer (Surlyn, DuPont) and clamped together by binders. The liquid electrolyte (Iodolyte HI-30, Solaronix) was injected into the gap between the two electrodes by vacuum backfilling through a small hole on the counter electrode. The hole was sealed using thermoplastic to complete the fabrication of a DSC. The as-fabricated solar cells with Pt as catalyst (Pt-DSC) and MWNT as catalyst (MWNT-DSC) are pictured in Figure 4-4, when held against a computer screen. As demonstrated in Figure 4-4, both of them are semi-transparent and the letters on the screen can be seen through both solar cells.

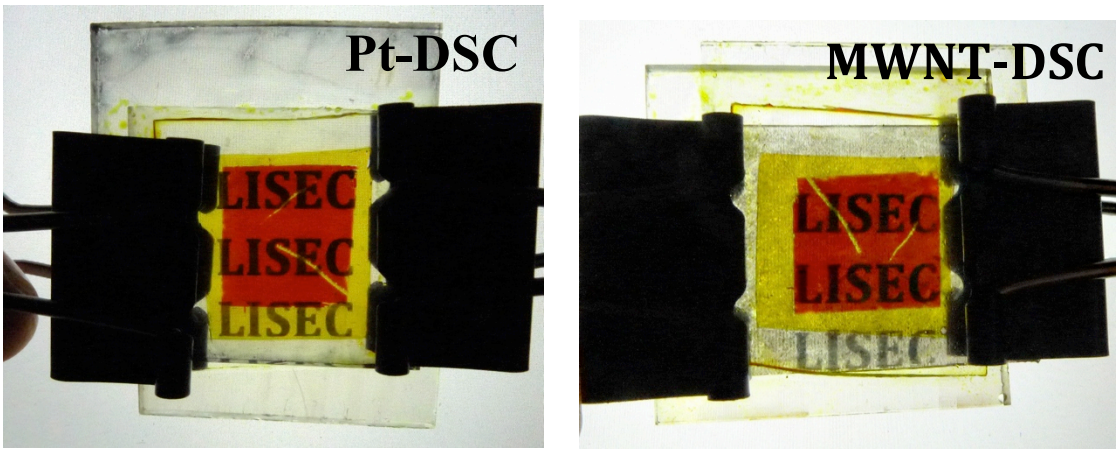

(a) (b)

Figure 4-4 Photos of as-fabricated semi-transparent DSC using platinum and MWNT as counter electrodes. (a) and (b) are Pt-DSC and MWNT-DSC held against computer screen respectively.

4.4.3 DSC Photovoltaic Performance Characterization

Both solar cells were tested under the same condition, i.e. under 25 mWatt/cm^2 radiation from a photoflood incandescent light bulb (Light Kit, Speedball). Both DSCs are of the size 1cm by 1cm. Figure 4-5 is the V-I curves obtained the two DSCs. The Pt-DSC has a larger short circuit current J_{sc} than the MWNT-DSC, whereas the open circuit voltage V_{oc} of MWNT-DSC is only slightly larger than the Pt-DSC. Hence, the Pt-DSC has a higher power output at most of the scanning voltages as shown in Figure 4-5. PCEs caculated from the V-I curves are 3.24% for Pt-DSC and 2.67% for MWNT-DSC. Both PCEs are larger than the required 1.8% for solar-powered ANC window facing north. Important metrics of the DSCs are summarized and compared in Table 4-1. The reason for MWNT-DSC's lower J_{sc} is that the MWNT thin film has lower electrical conductivity than the Pt thin film, which is confirmed by the relatively lower fill factor of the MWNT-DSC. Fill factor is defined as the ratio of the maximum power calculated from the V-I

curve to the product of the open circuit voltage V_{oc} and the short circuit current J_{sc}. High fill factor means the solar cell has a low equivalent series resistance and a high equivalent shunt resistance (ESR), hence less of the electrical energy generated by the solar cell is wasted through heat dissipation. The relatively lower fill factor of the MWNT-DSC demonstrates a higher ESR, which can only be explained by the lower electrical conductivity of the MWNT counter electrode, since the working electrode is identical for both Pt- and MWNT- DSCs. The V_{oc} of both cells are almost the same. To improve the PCE of MWNT-DSC, the J_{sc} must be increased. Higher J_{sc} can be achieved by increasing the conductivity of the MWNT thin film. Increasing the number of the LBL self-assembled layers could give higher conductivity, but at the expense of lower transparency.

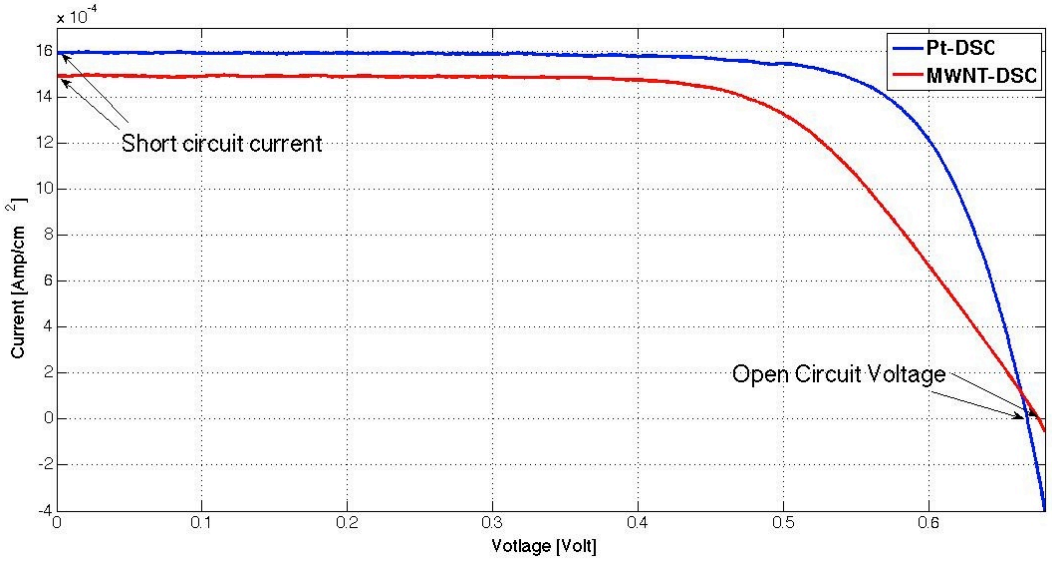

Figure 4-5 V-I curves of the Pt-DSC and MWNT-DSC under 25 mWatt/cm^2 radiation from an incandescent light bulb

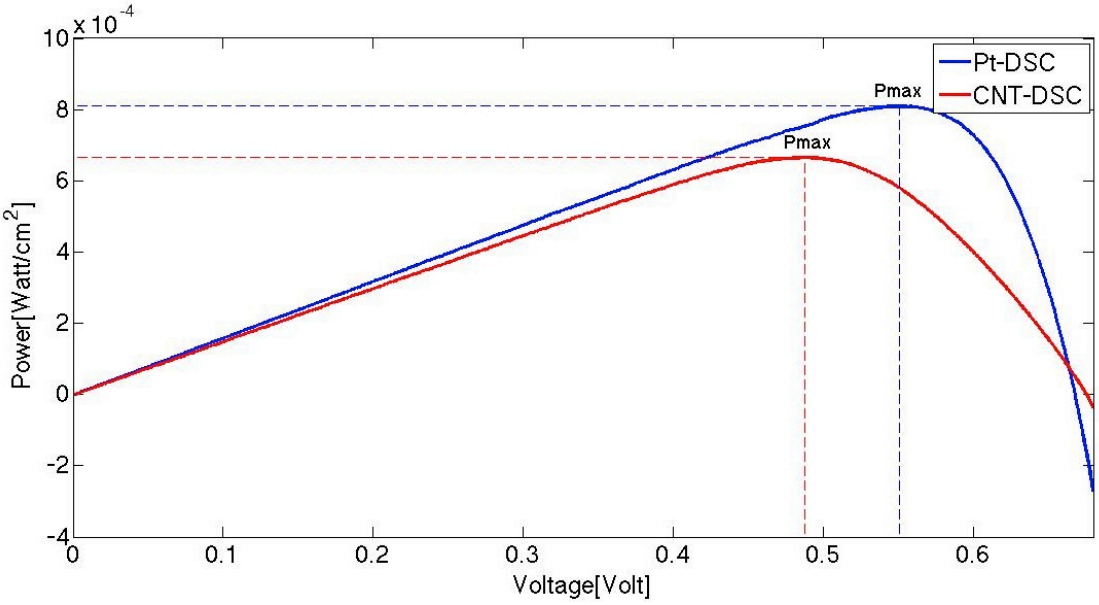

Figure 4-6 Power curves of the Pt-DSC and MWNT-DSC under 25 mWatt/cm^2 radiation from an incandescent light bulb

Table 4-1 Performance metrics of Pt-DSC and MWNT-DSC

	Short-circuit J_{SC} (mA)	**Open-circuit V V_{OC} (Volt)**	**Max Power P_{max} (mWatt)**	**Fill Factor *FF***	**PCE η (%)**
Pt-DSC	1.60	0.67	0.81	0.76	3.24
CNT-DSC	1.50	0.68	0.67	0.66	2.67

5 Conclusions and Future Work

This research explores the application of carbon nanotube (CNT) films for active noise cancellation, solar energy harvesting and energy storage in building windows. The CNT-based components developed herein can be integrated into a solar-powered active noise control system for a building window.

A novel control system was developed, which integrates a wave separation algorithm and a secondary path transfer function estimator with a standard feedforward adaptive noise controller. Such a control system allows the use of a CNT-based transparent acoustic actuator for simultaneous ANC and auxiliary audio playback. The wave separation algorithm works to prevent sound generated by the transparent speaker from entering the reference measurement. The performance of the new reference measurement system with the wave separation algorithm depends on the inter-microphone distance in the reference microphone pair. Small distance is preferable for high performance. The secondary path transfer function, estimated by either the additive random signals or the readily available audio signals, was used to remove the audio sound that enters the error measurement. Experiments using both narrowband and broadband sound prove that the added algorithms and hardware can eliminate the interference between the ANC and auxiliary audio playback, and also ensure that desirable internal sounds generated inside the buildings are not cancelled.

Porous and conductive CNT thin films were used as electrode materials for high-performance supercapacitors. Such supercapacitors with high power can work as an

energy management buffer between the low-power solar cells and the high-power real-time ANC. Two generations of flexible, thin, and fully solid-state supercapacitors are developed. Both generations consist of CNT films coated on supporting substrates as electrodes and a solid-state polymer gel layer for the electrolyte. They are easy to be fabricated in large-scale on a variety of substrates, such as paper, polymer, etc. They are thin and flexible, thus can be mounted on almost any surfaces including those inaccessible to traditional bulky supercapacitors. They are solid-state without the electrolyte-leaking problem, thus handling is easy. The first generation is a single-cell parallel-plate supercapacitor with a working voltage of 1.5 Volt. Its energy density is competitive with commercially available supercapacitors (which use liquid electrolyte). The second-generation is a multi-cell planar supercapacitor. Unlike the first generation's 3D structure, the second generation has a novel planar (2D) architecture, which makes it easy to integrate multiple cells into a thin and flexible supercapacitor. A six-cell device with a working voltage as high as 12 Volt is demonstrated by this research. The multi-cell planar supercapacitor has energy density exceeding that of other planar supercapacitors in literature by more than one order of magnitude. The performance of the developed supercapacitors is affected by the supporting substrates. Paper substrates provide higher capacitance and longer capacitance retention than PET substrates. It is proposed that paper's porous structure and hydrogen bonding between paper cellulose and functionalized CNT contribute to the high performance of the paper-based supercapacitors. All-solution fabrication processes were developed for both generations to achieve economical and scalable production. The internal resistance of the developed

CNT-based supercapacitor is still higher than commercial supercapacitors. Future work is needed to identify the source of the internal resistance: whether is from the interface between the electrode and the electrolyte or from the electrolyte itself.

Nickel/Nickel Oxide core-shell nanowires were synthesized by a template-assisted method and used as electrode materials for battery-like pseudocapacitors. The specific capacitances of such pseudocapacitors were high, but their working voltages were low (< 1 Volt), which limits the energy density of the capacitor. Future work is needed to solve the low working voltage problem.

Semi-transparent dye sensitized solar cells (DSCs) with CNT counter electrodes are developed to power the active noise cancellation system. The CNT counter electrode is used to replace the more expensive but less chemically robust platinum counter electrode. The developed CNT-DSCs have an efficiency of 2.67%, slightly lower than the Pt-DSC's efficiency of 3.24%, due to a smaller photocurrent caused by the relatively lower conductivity of the CNT counter electrode. However, the 2.67% efficiency is already higher than the 1.8% efficiency required for harvesting adequate energy to cancel noise of 70dB Day-Night-Level. Moreover, the CNT-DSCs are semi-transparent and see-through. Hence, they can be directly mounted on the glass panes and become part of the home window. This kind of solar cell has great potential to be integrated into building windows and car windows for solar energy harvesting.

In summary, this project develops several fundamental technologies that together can contribute to a solar-powered active noise cancellation system for a building window. At the same time, since the component technologies being developed are fundamental, it

is also likely that they will have wider applications in other domains beyond building windows.

Bibliography

[1] Saito, R., Dresselhaus, G., & Dresselhaus, M. S. (1998). *Physical properties of carbon nanotubes* (Vol. 4). London: Imperial college press.

[2] Odom, T. W., Huang, J. L., Kim, P., & Lieber, C. M. (1998). Atomic structure and electronic properties of single-walled carbon nanotubes. *Nature*, *391*(6662), 62-64.

[3] Mintmire, J. W., & White, C. T. (1995). Electronic and structural properties of carbon nanotubes. *Carbon*, *33*(7), 893-902.

[4] Yao, Z., Kane, C. L., & Dekker, C. (2000). High-field electrical transport in single-wall carbon nanotubes. *Physical Review Letters*, *84*(13), 2941.

[5] Wong, E. W., Sheehan, P. E., & Lieber, C. M. (1997). Nanobeam mechanics: elasticity, strength, and toughness of nanorods and nanotubes. *Science*, *277*(5334), 1971-1975.

[6] Dalton, A. B., Collins, S., Munoz, E., Razal, J. M., Ebron, V. H., Ferraris, J. P., ... & Baughman, R. H. (2003). Super-tough carbon-nanotube fibres. *Nature*, *423*(6941), 703-703.

[7] Pop, E., Mann, D., Wang, Q., Goodson, K., & Dai, H. (2006). Thermal conductance of an individual single-wall carbon nanotube above room temperature. *Nano Letters*, *6*(1), 96-100.

[8] Kaur, S., Raravikar, N., Helms, B. A., Prasher, R., & Ogletree, D. F. (2014). Enhanced thermal transport at covalently functionalized carbon nanotube array interfaces. *Nature communications*, *5*.

[9] Kordas, K., Tóth, G., Moilanen, P., Kumpumäki, M., Vähäkangas, J., Uusimäki, A., ... & Ajayan, P. M. (2007). Chip cooling with integrated carbon nanotube microfin architectures. *Applied Physics Letters*, *90*(12), 123105.

[10] Peigney, A., Laurent, C., Flahaut, E., Bacsa, R. R., & Rousset, A. (2001). Specific surface area of carbon nanotubes and bundles of carbon nanotubes. *Carbon*, *39*(4), 507-514.

[11] Edgeworth, J. P., Wilson, N. R., & Macpherson, J. V. (2007). Controlled Growth and Characterization of Two-Dimensional Single-Walled Carbon-Nanotube Networks for Electrical Applications. *Small*, *3*(5), 860-870.

[12] Murakami, Y., Chiashi, S., Miyauchi, Y., Hu, M., Ogura, M., Okubo, T., & Maruyama, S. (2004). Growth of vertically aligned single-walled carbon nanotube films on quartz substrates and their optical anisotropy. *Chemical Physics Letters*, *385*(3), 298-303.

[13] Tenent, R. C., Barnes, T. M., Bergeson, J. D., Ferguson, A. J., To, B., Gedvilas, L. M., ... & Blackburn, J. L. (2009). Ultrasmooth, Large-Area, High-Uniformity, Conductive Transparent Single-Walled-Carbon-Nanotube Films for Photovoltaics Produced by Ultrasonic Spraying. *Advanced materials*, *21*(31), 3210-3216.

[14] Kordás, K., Mustonen, T., Tóth, G., Jantunen, H., Lajunen, M., Soldano, C., ... & Ajayan, P. M. (2006). Inkjet printing of electrically conductive patterns of carbon nanotubes. *Small*, *2*(8-9), 1021-1025.

[15] Wu, Z., Chen, Z., Du, X., Logan, J. M., Sippel, J., Nikolou, M., ... & Rinzler, A. G. (2004). Transparent, conductive carbon nanotube films. *Science*, *305*(5688), 1273-1276.

[16] Hirsch, A. (2002). Functionalization of single-walled carbon nanotubes. *Angewandte Chemie International Edition*, *41*(11), 1853-1859.

[17] Ebbesen, T. W., & Ajayan, P. M. (1992). Large-scale synthesis of carbon nanotubes. *Nature*, *358*(6383), 220-222.

[18] Bronikowski, M. J., Willis, P. A., Colbert, D. T., Smith, K. A., & Smalley, R. E. (2001). Gas-phase production of carbon single-walled nanotubes from carbon monoxide via the HiPco process: A parametric study. *Journal of Vacuum Science & Technology A*, *19*(4), 1800-1805.

[19] Hu, H., Zhao, B., Itkis, M. E., & Haddon, R. C. (2003). Nitric acid purification of single-walled carbon nanotubes. *The Journal of Physical Chemistry B*, *107*(50), 13838-13842.

[20] Rinzler, A. G., Liu, J., Dai, H., Nikolaev, P., Huffman, C. B., Rodriguez-Macias, F. J., ... & Smalley, R. E. (1998). Large-scale purification of single-wall carbon nanotubes:

process, product, and characterization. *Applied Physics A: Materials Science & Processing*, *67*(1), 29-37.

[21] Dujardin, E., Ebbesen, T. W., Krishnan, A., & Treacy, M. M. (1998). Purification of single-shell nanotubes. *Advanced materials*, *10*(8), 611-613.

[22] Nagasawa, S., Yudasaka, M., Hirahara, K., Ichihashi, T., & Iijima, S. (2000). Effect of oxidation on single-wall carbon nanotubes. *Chemical Physics Letters*, *328*(4), 374-380.

[23] Datsyuk, V., Kalyva, M., Papagelis, K., Parthenios, J., Tasis, D., Siokou, A., ... & Galiotis, C. (2008). Chemical oxidation of multiwalled carbon nanotubes. *Carbon*, *46*(6), 833-840.

[24] Zhang, J., Zou, H., Qing, Q., Yang, Y., Li, Q., Liu, Z., ... & Du, Z. (2003). Effect of chemical oxidation on the structure of single-walled carbon nanotubes. *The Journal of Physical Chemistry B*, *107*(16), 3712-3718.

[25] O'connell, M. J., Bachilo, S. M., Huffman, C. B., Moore, V. C., Strano, M. S., Haroz, E. H., ... & Smalley, R. E. (2002). Band gap fluorescence from individual single-walled carbon nanotubes. *Science*, *297*(5581), 593-596.

[26] Islam, M. F., Rojas, E., Bergey, D. M., Johnson, A. T., & Yodh, A. G. (2003). High weight fraction surfactant solubilization of single-wall carbon nanotubes in water. *Nano Letters*, *3*(2), 269-273.

[27] Moore, V. C., Strano, M. S., Haroz, E. H., Hauge, R. H., Smalley, R. E., Schmidt, J., & Talmon, Y. (2003). Individually suspended single-walled carbon nanotubes in various surfactants. *Nano Letters*, *3*(10), 1379-1382.

[28] Strano, M. S., Moore, V. C., Miller, M. K., Allen, M. J., Haroz, E. H., Kittrell, C., ... & Smalley, R. E. (2003). The role of surfactant adsorption during ultrasonication in the dispersion of single-walled carbon nanotubes. *Journal of Nanoscience and Nanotechnology*, *3*(1-2), 1-2.

[29] Backes, C. and Hirsch, A. (2010) Noncovalent Functionalization of Carbon Nanotubes, in Chemistry of Nanocarbons (eds T. Akasaka, F. Wudl and S. Nagase), John Wiley & Sons, Ltd, Chichester, UK. doi: 10.1002/9780470660188.ch1

[30] Minneapolis St. Paul Metropolitan Airports Commision, "MSP Annual Noise Contour Analysis", URL: http://www.macnoise.com/sites/macnoise.com/files/pdf/2011-MSP-Annual-Noise-Contour-Report-2-29-12.pdf , 2011.

[31] Keast, D.N., "Energy Conservation and Noise Control in Residences", *Sound and Vibration*, Vol. 13, No.7, pp. 18-22, July, 1979.

[32] W. A. Utley, I. B. Buller, E. C. Keighley, J. W. Sargent, "Effectiveness and Acceptability of Measures for Insulating Dwellings Against Traffic Noise," *Journal of Sound and Vibration*, Vol. 109, Issue 1, pp. 1-18, August, 1986.

[33] C. Deffayet and P.A. Nelson, "Active Control of Low-frequency Harmonic Sound Radiated by a Finite Panel," *Journal of Acoustic Society of America*, Vol. 84 (6), pp.2192-2199.

[34] Billoud, G. D. (2002). *U.S. Patent No. 6,343,127*. Washington, DC: U.S. Patent and Trademark Office.

[35] Elliot, S. J., Nelson, P. A., Stothers, I. M., & Boucher, C. C. (1990). In-flight experiments on the active control of propeller-induced cabin noise. *Journal of Sound and Vibration*, *140*(2), 219-238.

[36] Sas, P., Bao, C., Augusztinovicz, F., & Desmet, W. (1995). Active control of sound transmission through a double panel partition. *Journal of Sound and Vibration*, *180*(4), 609-625.

[37] Kaiser, O. E., Pietrzko, S. J., & Morari, M. (2003). Feedback control of sound transmission through a double glazed window. *Journal of Sound and Vibration*, *263*(4), 775-795.

[38] Al-Bassyiouni, M., & Balachandran, B. (2005). Sound transmission through a flexible panel into an enclosure: structural–acoustics model. *Journal of Sound and Vibration*, *284*(1), 467-486.

[39] Yu, X., Rajamani, R., Stelson, K. A., & Cui, T. (2007). Active control of sound transmission through windows with carbon nanotube-based transparent actuators. *Control Systems Technology, IEEE Transactions on*, *15*(4), 704-714.

[40] Yu, X., Rajamani, R., Stelson, K. A., & Cui, T. (2006). Carbon nanotube-based transparent thin film acoustic actuators and sensors. *Sensors and Actuators A: Physical*, *132*(2), 626-631.

[41] Haykin, S. S. (2008). *Adaptive filter theory*. Pearson Education India.

[42] Elliott, S. J., & Nelson, P. A. (1993). Active noise control. *Signal Processing Magazine, IEEE*, *10*(4), 12-35.

[43] De Sanctis, G., & van Walstijn, M. (2009, September). A frequency domain adaptive algorithm for wave separation. In *12th Int. Conference on Digital Audio Effects (DAFx-09), Como, Italy*.

[44] Kemp, J. A., van Walstijn, M., Campbell, D. M., Chick, J. P., & Smith, R. A. (2010). Time domain wave separation using multiple microphones. *The Journal of the Acoustical Society of America*, *128*(1), 195-205.

[45] Zhu, H., Rajamani, R., & Stelson, K. A. (2003). Active control of acoustic reflection, absorption, and transmission using thin panel speakers. *The Journal of the Acoustical Society of America*, *113*(2), 852-870.

[46] Eriksson, L. J., & Allie, M. C. (1989). Use of random noise for on-line transducer modeling in an adaptive active attenuation system. *The Journal of the Acoustical Society of America*, *85*(2), 797-802.

[47] Zhang, M., Lan, H., & Ser, W. (2000). An improved secondary path modeling method for active noise control systems. *Signal Processing Letters, IEEE*, *7*(4), 73-75.

[48] Kuo, S. M., Mitra, S., & Gan, W. S. (2006). Active noise control system for headphone applications. *Control Systems Technology, IEEE Transactions on*, *14*(2), 331-335.

[49] Obreja, V. V. (2008). On the performance of supercapacitors with electrodes based on carbon nanotubes and carbon activated material—a review. *Physica E: Low-dimensional Systems and Nanostructures*, *40*(7), 2596-2605.

[50] California Department of Transportation, "Loudness Comparison Chart (dBA)", URL: http://www.dot.ca.gov/dist2/projects/sixer/loud.pdf, 2012.

[51] Hu, L., Wu, H., & Cui, Y. (2010). Printed energy storage devices by integration of electrodes and separators into single sheets of paper. *Applied Physics Letters*, *96*(18), 183502.

[52] Ma, L., & Yang, Y. (2005). Solid-state supercapacitors for electronic device applications. *Applied Physics Letters*, *87*(12), 123503.

[53] Fuller, J., Breda, A. C., & Carlin, R. T. (1997). Ionic Liquid-Polymer Gel Electrolytes. *Journal of the Electrochemical Society*, *144*(4), L67-L70.

[54] Chao, S., & Wrighton, M. S. (1987). Characterization of a solid-state polyaniline-based transistor: water vapor dependent characteristics of a device employing a poly (vinyl alcohol)/phosphoric acid solid-state electrolyte. *Journal of the American Chemical Society*, *109*(22), 6627-6631.

[55] Pushparaj, V. L., Shaijumon, M. M., Kumar, A., Murugesan, S., Ci, L., Vajtai, R., ... & Ajayan, P. M. (2007). Flexible energy storage devices based on nanocomposite paper. *Proceedings of the National Academy of Sciences*, *104*(34), 13574-13577.

[56] Yun, S., Jang, S. D., Yun, G. Y., Kim, J. H., & Kim, J. (2009). Paper transistor made with covalently bonded multiwalled carbon nanotube and cellulose. *Applied Physics Letters*, *95*(10), 104102.

[57] Hu, L., Choi, J. W., Yang, Y., Jeong, S., La Mantia, F., Cui, L. F., & Cui, Y. (2009). Highly conductive paper for energy-storage devices. *Proceedings of the National Academy of Sciences*, *106*(51), 21490-21494.

[58] Frackowiak, E., & Beguin, F. (2001). Carbon materials for the electrochemical storage of energy in capacitors. *Carbon*, *39*(6), 937-950.

[59] An, K. H., Jeon, K. K., Kim, W. S., Park, Y. S., Lim, S. C., Bae, D. J., & Lee, Y. H. (2001). Characterization of supercapacitors using singlewalled carbon nanotube electrodes. *JOURNAL-KOREAN PHYSICAL SOCIETY*, *39*, S511-S517.

[60] Ng, K. C., Zhang, S., Peng, C., & Chen, G. Z. (2009). Individual and bipolarly stacked asymmetrical aqueous supercapacitors of CNTs/SnO2 and CNTs/MnO2 nanocomposites. *Journal of The Electrochemical Society*, 156(11), A846-A853.

[61] Zhang, S., Peng, C., Ng, K. C., & Chen, G. Z. (2010). Nanocomposites of manganese oxides and carbon nanotubes for aqueous supercapacitor stacks. *Electrochimica Acta*, 55(25), 7447-7453.

[62] Staiti, P., & Lufrano, F. (2005). Design, fabrication, and evaluation of a 1.5 F and 5 V prototype of solid-state electrochemical supercapacitor. *Journal of The Electrochemical Society*, 152(3), A617-A621.

[63] El-Kady, M. F., & Kaner, R. B. (2013). Scalable fabrication of high-power graphene micro-supercapacitors for flexible and on-chip energy storage. *Nature communications*, 4, 1475.

[64] Wu, Z. S., Parvez, K., Feng, X., & Müllen, K. (2013). Graphene-based in-plane micro-supercapacitors with high power and energy densities. *Nature communications*, 4.

[65] Feng, J., Sun, X., Wu, C., Peng, L., Lin, C., Hu, S., ... & Xie, Y. (2011). Metallic few-layered VS2 ultrathin nanosheets: high two-dimensional conductivity for in-plane supercapacitors. *Journal of the American Chemical Society*, 133(44), 17832-17838.

[66] Yoo, J. J., Balakrishnan, K., Huang, J., Meunier, V., Sumpter, B. G., Srivastava, A., ... & Ajayan, P. M. (2011). Ultrathin planar graphene supercapacitors. *Nano letters*, 11(4), 1423-1427.

[67] El-Kady, M. F., Strong, V., Dubin, S., & Kaner, R. B. (2012). Laser scribing of high-performance and flexible graphene-based electrochemical capacitors. *Science*, 335(6074), 1326-1330.

[68] Jiang, Y. Q., Zhou, Q., & Lin, L. (2009, January). Planar MEMS supercapacitor using carbon nanotube forests. In *Micro Electro Mechanical Systems, 2009. MEMS 2009. IEEE 22nd International Conference on* (pp. 587-590). IEEE.

[69] Endo, M., Muramatsu, H., Hayashi, T., Kim, Y. A., Terrones, M., & Dresselhaus, M. S. (2005). Nanotechnology:'Buckypaper'from coaxial nanotubes. *Nature*, *433*(7025), 476-476.

[70] 15. Zhang, D., Ryu, K., Liu, X., Polikarpov, E., Ly, J., Tompson, M. E., & Zhou, C. (2006). Transparent, conductive, and flexible carbon nanotube films and their application in organic light-emitting diodes. *Nano Letters*, 6(9), 1880-1886.

[71] Carrilho, E., Martinez, A. W., & Whitesides, G. M. (2009). Understanding wax printing: a simple micropatterning process for paper-based microfluidics. *Analytical Chemistry*, 81(16), 7091-7095.

[72] Martinez, A. W., Phillips, S. T., Wiley, B. J., Gupta, M., & Whitesides, G. M. (2008). FLASH: a rapid method for prototyping paper-based microfluidic devices. *Lab on a Chip*, 8(12), 2146-2150.

[73] Wang, G., Lu, X., Ling, Y., Zhai, T., Wang, H., Tong, Y., & Li, Y. (2012). LiCl/PVA Gel Electrolyte Stabilizes Vanadium Oxide Nanowire Electrodes for Pseudocapacitors. *ACS nano*, 6(11), 10296-10302.

[74] Hu, L., Pasta, M., Mantia, F. L., Cui, L., Jeong, S., Deshazer, H. D., ... & Cui, Y. (2010). Stretchable, porous, and conductive energy textiles. *Nano letters*, 10(2), 708-714.

[75] Hu, L., Choi, J. W., Yang, Y., Jeong, S., La Mantia, F., Cui, L. F., & Cui, Y. (2009). Highly conductive paper for energy-storage devices. *Proceedings of the National Academy of Sciences*, 106(51), 21490-21494.

[76] An, K. H., Kim, W. S., Park, Y. S., Moon, J. M., Bae, D. J., Lim, S. C., ... & Lee, Y. H. (2001). Electrochemical properties of high-power supercapacitors using single-walled carbon nanotube electrodes. *Advanced Functional Materials*, 11(5), 387-392.

[77] Conway, B. E. (1991). Transition from "supercapacitor" to "battery" behavior in electrochemical energy storage. *Journal of the Electrochemical Society*, *138*(6), 1539-1548.

[78] Jang, J. H., Kato, A., Machida, K., & Naoi, K. (2006). Supercapacitor performance of hydrous ruthenium oxide electrodes prepared by electrophoretic deposition. *Journal of The Electrochemical Society*, *153*(2), A321-A328.

[79] Xu, J., Gao, L., Cao, J., Wang, W., & Chen, Z. (2010). Preparation and electrochemical capacitance of cobalt oxide (Co< sub> 3</sub> O< sub> 4</sub>) nanotubes as supercapacitor material. *Electrochimica Acta*, *56*(2), 732-736.

[80] Zheng, Y. Z., Ding, H. Y., & Zhang, M. L. (2009). Preparation and electrochemical properties of nickel oxide as a supercapacitor electrode material. *Materials Research Bulletin*, *44*(2), 403-407.

[81] Guo, Y. G., Hu, J. S., & Wan, L. J. (2008). Nanostructured materials for electrochemical energy conversion and storage devices. *Advanced Materials*, *20*(15), 2878-2887.

[82] Aricò, A. S., Bruce, P., Scrosati, B., Tarascon, J. M., & Van Schalkwijk, W. (2005). Nanostructured materials for advanced energy conversion and storage devices. *Nature materials*, *4*(5), 366-377.

[83] National Renewable Energy Laboratory, "The Solar Radiation Data Manual for Buildings", URL: http://rredc.nrel.gov/solar/old_data/nsrdb/1961-1990/bluebook/, 2014.

[84] National Renewable Energy Laboratory, "Research Cell Efficiency Records", URL: http://www.nrel.gov/ncpv/images/efficiency_chart.jpg, 2012.

[85] Miles, R. W., Zoppi, G., & Forbes, I. (2007). Inorganic photovoltaic cells. *Materials Today*, *10*(11), 20-27.

[86] Takeoka, A., Kouzuma, S., Tanaka, H., Inoue, H., Murata, K., Morizane, M., ... & Kuwano, Y. (1993). Development and application of see-through a-Si solar cells. *Solar Energy Materials and Solar Cells*, *29*(3), 243-252.

[87] Huang, J., Li, G., & Yang, Y. (2008). A Semi-transparent Plastic Solar Cell Fabricated by a Lamination Process. *Advanced Materials*, *20*(3), 415-419.

[88] Peumans, P., Yakimov, A., & Forrest, S. R. (2003). Small molecular weight organic thin-film photodetectors and solar cells. *Journal of Applied Physics*, *93*(7), 3693-3723.

[89] Peumans, P., Uchida, S., & Forrest, S. R. (2003). Efficient bulk heterojunction photovoltaic cells using small-molecular-weight organic thin films. *Nature*, *425*(6954), 158-162.

[90] Lunt, R. R., & Bulovic, V. (2011). Transparent, near-infrared organic photovoltaic solar cells for window and energy-scavenging applications. *Applied Physics Letters*, *98*(11), 113305.

[91] Rand, B. P., Genoe, J., Heremans, P., & Poortmans, J. (2007). Solar cells utilizing small molecular weight organic semiconductors. *Progress in Photovoltaics: Research and Applications*, *15*(8), 659-676.

[92] Salzman, R. F., Xue, J., Rand, B. P., Alexander, A., Thompson, M. E., & Forrest, S. R. (2005). The effects of copper phthalocyanine purity on organic solar cell performance. *Organic Electronics*, *6*(5), 242-246.

[93] Hardin, B. E., Snaith, H. J., & McGehee, M. D. (2012). The renaissance of dye-sensitized solar cells. *Nature Photonics*, *6*(3), 162-169.

[94] Grätzel, M. (2003). Dye-sensitized solar cells. *Journal of Photochemistry and Photobiology C: Photochemistry Reviews*, *4*(2), 145-153.

[95] Shin, K. H., Ahn, J. H., Kang, H. K., & Eom, Y. S. (2014). *U.S. Patent No. 8,658,455*. Washington, DC: U.S. Patent and Trademark Office.

[96] O'regan, B., & Grfitzeli, M. (1991). A low-cost, high-efficiency solar cell based on dye-sensitized. *Nature*, *353*, 737-740.

[97] Nazeeruddin, M. K., Kay, A., Rodicio, I., Humphry-Baker, R., Müller, E., Liska, P., ... & Grätzel, M. (1993). Conversion of light to electricity by cis-X2bis (2, 2'-bipyridyl-4, 4'-dicarboxylate) ruthenium (II) charge-transfer sensitizers (X= Cl-, Br-, I-, CN-, and SCN-) on nanocrystalline titanium dioxide electrodes. *Journal of the American Chemical Society*, *115*(14), 6382-6390.

[98] Nazeeruddin, M. K., Zakeeruddin, S. M., Humphry-Baker, R., Jirousek, M., Liska, P., Vlachopoulos, N., ... & Grätzel, M. (1999). Acid-base equilibria of (2, 2'-bipyridyl-4, 4'-dicarboxylic acid) ruthenium (II) complexes and the effect of protonation on charge-transfer sensitization of nanocrystalline titania. *Inorganic Chemistry*, *38*(26), 6298-6305.

[99] Wang, P., Zakeeruddin, S. M., Moser, J. E., Nazeeruddin, M. K., Sekiguchi, T., & Grätzel, M. (2003). A stable quasi-solid-state dye-sensitized solar cell with an amphiphilic ruthenium sensitizer and polymer gel electrolyte. *Nature Materials*, *2*(6), 402-407.

[100] Oskam, G., Bergeron, B. V., Meyer, G. J., & Searson, P. C. (2001). Pseudohalogens for dye-sensitized TiO2 photoelectrochemical cells. *The Journal of Physical Chemistry B*, *105*(29), 6867-6873.

[101] Nusbaumer, H., Moser, J. E., Zakeeruddin, S. M., Nazeeruddin, M. K., & Grätzel, M. (2001). CoII (dbbip) 22+ complex rivals tri-iodide/Iodide redox mediator in dye-

sensitized photovoltaic cells. *The Journal of Physical Chemistry B*, *105*(43), 10461-10464.

[102] Imoto, K., Takahashi, K., Yamaguchi, T., Komura, T., Nakamura, J. I., & Murata, K. (2003). High-performance carbon counter electrode for dye-sensitized solar cells. *Solar Energy Materials and Solar Cells*, *79*(4), 459-469.

[103] Roy-Mayhew, J. D., Bozym, D. J., Punckt, C., & Aksay, I. A. (2010). Functionalized graphene as a catalytic counter electrode in dye-sensitized solar cells. *Acs Nano*, *4*(10), 6203-6211.

[104] Murakami, T. N., Ito, S., Wang, Q., Nazeeruddin, M. K., Bessho, T., Cesar, I., ... & Grätzel, M. (2006). Highly efficient dye-sensitized solar cells based on carbon black counter electrodes. *Journal of the Electrochemical Society*, *153*(12), A2255-A2261.

[105] Suzuki, K., Yamaguchi, M., Kumagai, M., & Yanagida, S. (2003). Application of Carbon Nanotubes to Counter Electrodes of Dye-sensitized Solar Cells. *Chemistry Letters*, *32*(1), 28-29.

[106] SukáJang, J., & JináHam, D. (2010). Platinum-free tungsten carbides as an efficient counter electrode for dye sensitized solar cells. *Chemical Communications*, *46*(45), 8600-8602.

[107] Li, G. R., Wang, F., Jiang, Q. W., Gao, X. P., & Shen, P. W. (2010). Carbon Nanotubes with Titanium Nitride as a Low-Cost Counter-Electrode Material for Dye-Sensitized Solar Cells. *Angewandte Chemie International Edition*, *49*(21), 3653-3656.

[108] Ito, S., Murakami, T. N., Comte, P., Liska, P., Grätzel, C., Nazeeruddin, M. K., & Grätzel, M. (2008). Fabrication of thin film dye sensitized solar cells with solar to electric power conversion efficiency over 10%. *Thin Solid Films*, *516*(14), 4613-4619.

[109] Hore, S., Vetter, C., Kern, R., Smit, H., & Hinsch, A. (2006). Influence of scattering layers on efficiency of dye-sensitized solar cells. *Solar Energy Materials and Solar Cells*, *90*(9), 1176-1188.

[110] Colodrero, S., Mihi, A., Häggman, L., Ocana, M., Boschloo, G., Hagfeldt, A., & Miguez, H. (2009). Porous One-Dimensional Photonic Crystals Improve the Power-

Conversion Efficiency of Dye-Sensitized Solar Cells. *Advanced Materials*, *21*(7), 764-770.

[111] Bermel, P., Luo, C., Zeng, L., Kimerling, L. C., & Joannopoulos, J. D. (2007). Improving thin-film crystalline silicon solar cell efficiencies with photonic crystals. *Optics Express*, *15*(25), 16986-17000.

[112] Heiniger, L. P., O'Brien, P. G., Soheilnia, N., Yang, Y., Kherani, N. P., Grätzel, M., ... & Tétreault, N. (2013). See-Through Dye-Sensitized Solar Cells: Photonic Reflectors for Tandem and Building Integrated Photovoltaics. *Advanced Materials*, *25*(40), 5734-5741.

[113] Zheng, H., Neo, C. Y., & Ouyang, J. (2013). Highly efficient iodide/triiodide dye-sensitized solar cells with gel-coated reduce graphene oxide/single-walled carbon nanotube composites as the counter electrode exhibiting an open-circuit voltage of 0.90 V. *ACS applied materials & interfaces*, *5*(14), 6657-6664.

[114] Murakami, T. N., Ito, S., Wang, Q., Nazeeruddin, M. K., Bessho, T., Cesar, I., ... & Grätzel, M. (2006). Highly efficient dye-sensitized solar cells based on carbon black counter electrodes. *Journal of the Electrochemical Society*, *153*(12), A2255-A2261.

[115] Ramasamy, E., Lee, W. J., Lee, D. Y., & Song, J. S. (2008). Spray coated multi-wall carbon nanotube counter electrode for tri-iodide reduction in dye-sensitized solar cells. *Electrochemistry Communications*, *10*(7), 1087-1089.

[116] Lee, W. J., Ramasamy, E., Lee, D. Y., & Song, J. S. (2009). Efficient dye-sensitized solar cells with catalytic multiwall carbon nanotube counter electrodes. *ACS Applied Materials & Interfaces*, *1*(6), 1145-1149.

[117] Xue, W., & Cui, T. (2007). Characterization of layer-by-layer self-assembled carbon nanotube multilayer thin films. *Nanotechnology*, *18*(14), 145709.